OPEN ACCESS

ACTA METALLURGICA SLOVACA

2020, VOL. 26, NO. 3, 78-84

RESEARCH PAPER

FRICTION WELDING OF AISI 304: EFFECT OF FRICTION TIME ON MICRO-STRUCTURE, MICRO-HARDNESS AND TENSION-COMPRESSION PROPERTIES

Ammar Jabbar Hassan[1]*, Taoufik Boukharouba[1], Djamel Miroud[1]

[1] Mechanical and Process Engineering Department, Houari Boumediene University of Sciences and Technology, BP. 32, El-Alia, 16111 Bab-Ezzoaur, Algiers-Algeria

Received: 14.05.2020
Accepted: 04.06.2020

*Corresponding author: e-mail: jabbarhassan1973@yahoo.fr, Mechanical and Process Engineering Department, Houari Boumediene University of Sciences and Technology, BP. 32, El-Alia, 16111 Bab-Ezzoaur, Algiers-Algeria

ABSTRACT

During direct drive friction welding could relatively predicting the micro-structural and mechanical properties of friction-welded joints by controlling the welding conditions; friction time is an important coefficient that effects on these properties, present study focused on the effect of that time on micro-structural and mechanical phenomena during that process. The process achieved in different friction time, while the effect of that time on welding joint strength investigated by macroscopic, microstructure, scanning electron microscope [SEM], tensile, compression and micro-hardness tests. The micro-hardness tests were performed along the interface and axial direction. Thus, the tensile tests carried out on the standardized test piece with effective diameter of 6 mm and compression tests were extracted at welded center in three angles of 0°, 45° and 90° with test specimen of 4 mm diameter and 6.5 mm length. The results showed that with increasing friction time could be found hard zone at the interface of welded joint because of extended of high plastically deformation zone [HPDZ], which will responsible on decreasing some useful mechanical properties such as ultimate tensile strength [UTS] and yield compression strength. However, tensile fracture position occurred adjacent to the interface at the thermo-mechanical deformation zone [TMDZ] in the rotating side for all welding pieces, where the micro-hardness attenuated at that region.

Keywords: Austenitic stainless steel; Friction time; Thermo-mechanical deformation zone [TMDZ]; Ultimate tensile strength [UTS]; Compression yield strength

INTRODUCTION

Friction welding is well known among solid-state joining methods. Principle characteristic of this process is producing coalescence at temperature essentially below than the melting point of the base metal being welded [1, 2]. This method is clean, easily automated, high energy efficiency, narrower heat affected zone [HAZ], low welding cost, high material save and low production time [3-5]. In particular, friction welding is able to easily produce joints with high reliability and efficiency; it is widely used in the automobile industries and applied to fabricate important parts such as drive shafts, compressor or pumps shafts and engine valves [6].

The friction welding has different techniques, inertia friction welding is one of this kind of welding, one of the work piece connected to flywheel and the other remains stationary. The flywheel has a constant rotating speed, where the required kinetic energy is stored, then the drive is separated and the pieces are subject together under friction force. This action force leads to rub the contacting surfaces together under pressure. The stored kinetic energy in the rotating flywheel produces heat through friction at the interface as decreases the speed of flywheel. The generation friction welding force applied before cease of rotation. The force is still retained a period of time after stop of rotation [7].

Friction stir welding, on the other hand, produces an essential plasticized material in weld line by using non-consumable rotating pin tool, which is held under pressure against the materials to be welded. This pin tool is at the center followed by the shoulder. A plastic state material is generated by heat resulted from friction between tool and materials that is in contact with. As the pin tool advanced along the weld line, the material from the face of the tool is cleaned around this plasticized circular region to the back, so that producing interface [8, 9].

Direct drive friction welding produces joining under direct compression force resulting from rubbing of two specimens interface, one chucked in stationary part while the other is held in rotating side. The heat generates at interface because of the continuous rubbing of surfaces in contact, however, causing in the first step high temperature increasing until further and subsequent cause of metal softening, the temperature deceases gradually. Ultimately, the material at the interface begins to be soft and form flash. When a certain amount of flash metal has occurred, the rotation stops and the compressive force is maintained or slightly increased to consolidate welding [10].

Several studies have been conducted to understand the influence of direct drive friction welding parameters on both microstructure evolution and mechanical properties of post-forging joints such as friction time [11-16], friction pressure [10-17], forging phase [18, 19] and finally rotation speed [20, 21]. This process as mentioned in the literature has two phases. First one for friction phase and second one for forging phase. Present study focused on the direct effect of friction time on the microstructure and mechanical properties of welding joint for AISI 304, the results were investigated by macroscopic, microstructure, scanning electron microscope [SEM], tensile, compression and micro-hardness tests. Practically, should be noted that the short friction time and high rotation speed obtained high tensile strength [21]. While, longer friction time achieved low tensile strength, high level of micro-hardness and larger HPDZ [2].

Currently, according to the previous works, many of them have been considered of friction welding for the austenitic stainless steel grades AISI 304 and AISI 304 L [11, 15, 18, 21], whereas, little publication articles have explained influence of stationary and rotating side for similar welding joint on the microstructural and mechanical properties of AISI 304. Thus present study attempts to expose the effect of compression yield strength for different angles of 0°, 45° and 90° under effect of friction time to discover the isotropy of AISI 304 during friction welding process. However, the present paper is concerned with the lack of information and includes a contribution to illustrate and understand the direct drive friction welding joint strength of AISI 304 on the microstructural and mechanical behavior.

MATERIAL AND METHODS

Parent metal

Present study used commercial austenitic stainless steel bars of AISI 304. Generally, this metal is weld-able and utilized in joining for several

applications such as: cryogenic, corrosive environment, chemical, medical, alimentation and nuclear industries. The metal as received has a Ref. No. of 4301, when the metal arrived to the laboratory as a long shaft of 6 m length, cut to small test pieces, 45 mm length and 12 mm diameter. The alloying elements as shown in the Table 1, hence the principle mechanical properties as revealed in the Table 2. The optical microstructure for AISI 304 is showing the equiaxed fine grains of austenite as illustrated in Fig. 1.

Table 1 Alloying elements of parent metal (wt.%)

C	Mn	Si	P	S	Mo	Cr	Ni
0.070	1.650	0.750	0.045	0.030	0.80	19.00	8.00

Table 2 Mechanical properties of parent metal (Ref. No. of 4301)

UTS (MPa)	E (MPa)	Elongation (%)	Average $Hv_{0.1}$	Compression yield strength (MPa)
760 - 780	$1.93\ 10^5$	≈ 47	280 - 285	550 - 520

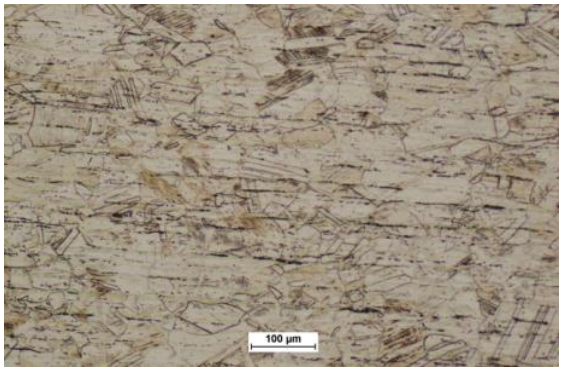

Fig. 1 Optical microstructures of the base metal, AISI 304

Welding process

Friction welding machine used in this work was designed and fabricated as a direct drive friction welding machine (Fig. 2); it was capable, precise and excellent for automatic controlling of welding conditions. The power rotating motor with brake has 3.5 kw, 3 Phases AC and operating speed can be varied from 0 to 3000 rpm, though brake utilized to suddenly stop of rotation at the end of friction phase. Friction and forging pressure applied by using hydraulic system and amplified via press, 300 MPa as a maximum pressure applied. The pressure was measured and verified by using two instruments, first one was the hydraulic pressure control and second one was the electronic pressure control. The friction time was experimentally calculated by control programmer and analyzed by present study to evaluate the effect of friction phase time on the evolution of mechanical and metallurgical properties of welded joint. Currently for this research prepared the following parameters: rotation speed 3000 rpm, friction pressure 130 MPa, forging pressure 260 MPa, forging time 5 s and with different friction time, 6.5, 8.5 and 10 s. Welding conditions selected according to the diameter of welding specimens (12 mm), type of the metal (AISI 304) and on the modern publication articles [2, 10].

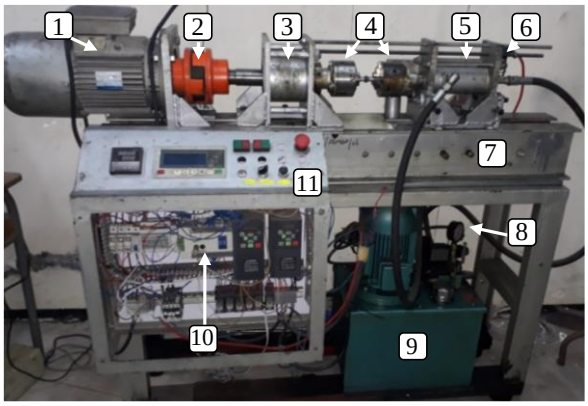

Fig. 2 Friction welding machine: 1. Main rotating motor with brake, 2. Clutch, 3. Bearing collar, 4. Chucks, 5. Press, 6. Electronic pressure control, 7. Main body, 8. Hydraulic pressure control, 9. Hydraulic unit, 10. Control programmer, 11. Control unit box

Metallography and welding profile study

Measurements of axial shortening achieved during welding operation by using a distance gauge with range between 0-20 mm and an accuracy of 0.01 mm. Macroscopic observations were carried out by optical macroscopic from type NIKON SMZ 745T with a magnification of X 0.67. To examine of microstructure, samples were taken from the welded simples using a Presi mecatome T180 cutting machine. They were pre-polished with wet SiC abrasive paper up to 1200 grit and then polished with 1 µm and ¼ µm diamond polishing paste. They were cleaned with deionized water and dried. Hence, the test pieces were electrolyte etched by 10 g oxalic acid hydrate and 90 ml water (Struers Lectropol-5) at 15 V for period of 300 s, while, microscopy observations were achieved by optical microscopy (NIKON ECLIPSE LV100ND) with a magnification of X 100. SEM observations obtained by JEOL JSM-6360 (EDAX) with magnification of the images X 50 and X 100.

Mechanical tests

Compression and tensile tests were carried out at room temperature using INSTRON 5500 and MTS 810 material testing system machines respectively, tensile tests used standardized test piece [ISO 6892-1: 2009 (F)] with effective diameter of 6 mm, machined in the axial direction (Fig. 3). While compression test pieces cut by electrical discharge machine with dimensions of 4 mm diameter and 6.5 mm length at welding center and extracted from three angles of 0°, 45° and 90° [10] as shown in Fig. 4. Micro-hardness measurements were performed over ± 4 and 4.5 mm on both sides for welding interface and axial direction respectively, the test specimens revealed in Fig. 5. Square based pyramidal diamond as indenter in Vickers tester machine from type SHIMADZU HMV with room temperature test conditions. The test pieces were polished with wet SiC abrasive paper until 1200 grit followed by 1 µm diamond paste on light disc cloth and finally degreased with ethanol and cleaned with deionized water. The Vickers hardness test conditions were 100 gf indent load and 10 s dwell time according to ASTM E384.

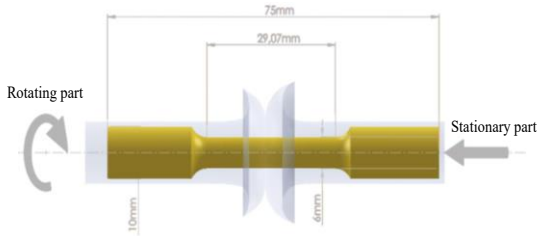

Fig. 3 Tensile test pieces according to standardized ISO 6892-1: 2009 (F)

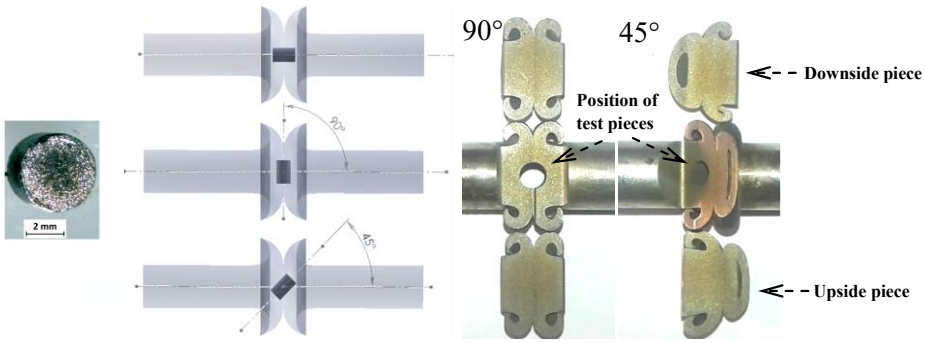

Fig. 4 Compression test pieces and the extracted position from three angles of 0°, 45° and 90°

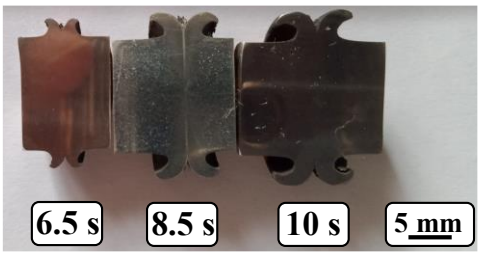

Fig. 5 Micro-hardness test pieces were carried out over ± 4 and 4.5 mm on both sides for axial direction and welding interface respectively

RESULTS & DISCUSSION

Macroscopic observation

The axial shortening characterization is an important factor which considered estimating of friction welding joint strength. The measured axial shortening of welded joints for stationary and rotating part was plotted according to the friction time as shown in Fig. 6. The axial shortening increased obviously with increasing friction time, this is also mentioned in previous articles [11, 20]. Thus, flash formation seems larger with increasing friction time, showing mainly, on the stationary side. This is may be explained by high plastic deformation in the friction welded joints which occurs by large amount at stationary side relative to rotating part (Fig. 7).

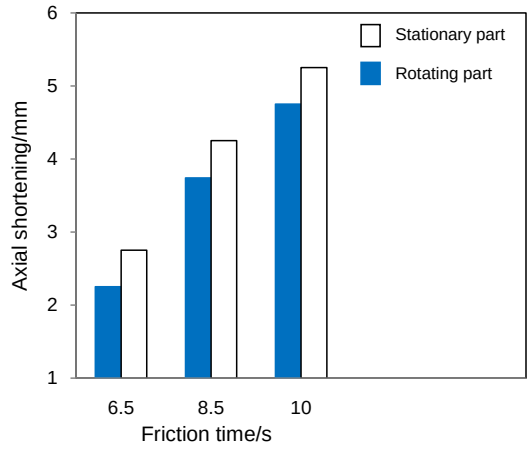

Fig. 6 Axial shortening vs. friction time

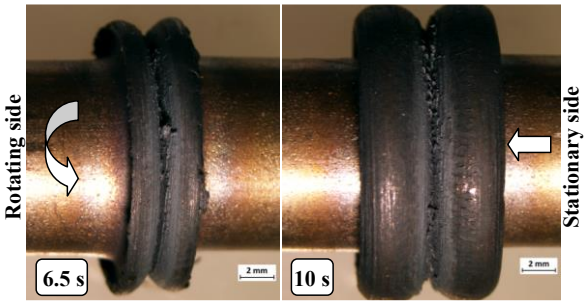

Fig. 7 Flash formation vs. friction time

Macro-graphic view for welded joint of 6.5 s and 10 s as illustrated in Fig. 8 exposed no macro cracks or defects, whereas can distinct large segregation in welding center for 10 s relative to 6.5 s, because of increasing in heat amount with friction time which results high thermo-plastic deformation in the welding line center.

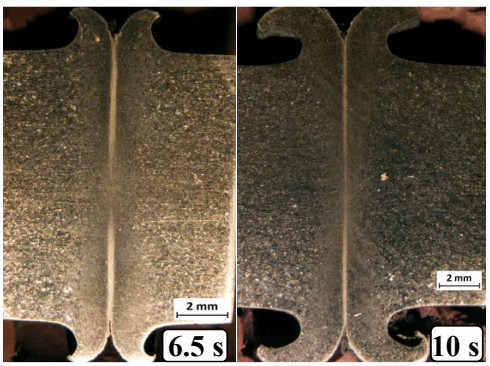

Fig. 8 Macro-graphic view for welding joint of 6.5 s and 10 s

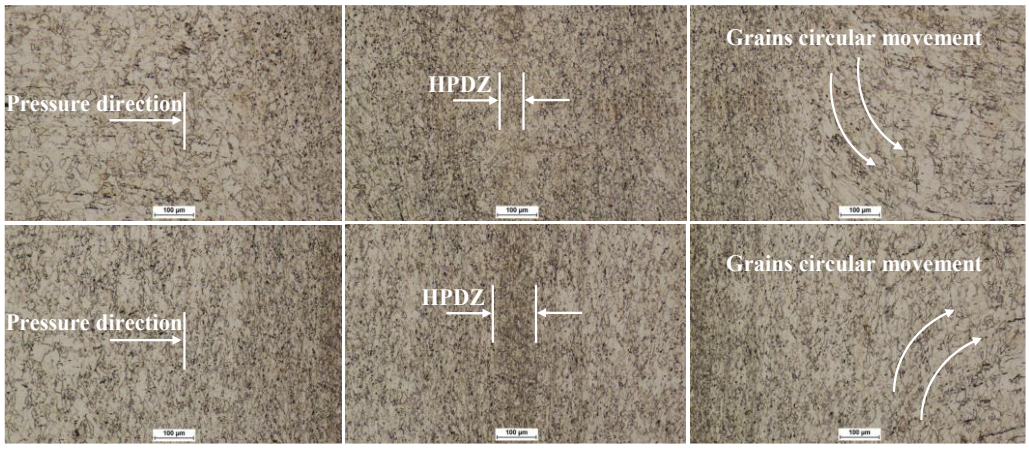

a) stationary side b) welding center c) rotating side

Fig. 9 Microstructure observed dimension of high plastically deformed zone [HPDZ], circular movement of grains and direction of pressure application: up: 6.5 s; down: 10 s

Microstructure observation

The optical microstructure study as illustrated in Fig. 9 reveals evolution of grain microstructure for the high plastically deformed zone [HPDZ] and thermo-mechanically deformation zone [TMDZ] for welding conditions of 6.5 s and 10 s in the stationary and rotating side. Fig. 9 (b) indicates fine grains with dark color at HPDZ, up for 6.5 s and down for 10s with relative dimension of 80 μm for 6.5 s while 110 μm for 10 s. Thus, as mentioned in macroscopic view (Fig. 8) discrete large separation in grains between the interface and the neighboring region for 10 s, whereas at 6.5 s illustrated homogenous grains distribution. The fine grains structure in HPDZ produced from dynamic recrystallization via high temperature and pressure concentrated at that region [22]. While dimension of HPDZ increased due to release of high amount of heat flow with elongated friction time [2]. TMDZ, on the other hand, extended in neighboring with coarse and narrow grains in stationary and rotating side [Figs. 9 (a) and (c)], the rotating side shows circular movement of grains with the motion of rotation and mechanical action, whereas the stationary side reveals the effect of pressure with elongated and deformed grains form.

Micro-hardness survey

Micro-hardness measurements obtained in Figs. 10 and 11 were carried out over ± 4 and 4.5 mm on both sides for welding interface and axial direction respectively. Micro-hardness profiles for welding interface as shown in Fig. 10 exposed general micro-hardness increase in all welding conditions relative to the base metal. The micro-hardness values increased from peripheral to the central, while these values in maximum level at longest friction time 10 s.

The welding interface suffered most thermo-plastic deformation via high friction between contact surfaces at the interface [4], which results dynamic recrystallization cause of high pressure and temperature. Forging pressure, on the other hand, is great responsible on the elevation of hardness due to strain hardening effect during process [23], that revealed as a high plastically deformed zone HPDZ at the weld interface with dark color [15]. The post weld interface joint, because of that effect, obtained fine grains with recrystallized forms [24], which will to blame on high level of micro-hardness.

Fig. 11 summarized the micro-hardness measurements obtained in the axial direction; the micro-hardness profiles illustrate uniform distribution along that axis an closer to the values of the base metal, whereas the welding line recorded the highest values of micro-hardness. High friction time gives maximum values at welding line and reduced with friction time decreasing. On the other hand, the micro-hardness attenuation as shown in the neighboring zone, precisely at TMDZ in the rotating side, resulted from limiting recrystallization because of heat distribution during welding process and also because of effect of thermo-mechanical deformation at that side resulted from high speed of rotation and pressure application. Finally as a result of micro-hardness observation of high Cr-Ni commercial austenitic stainless steel [AISI 304, Ref. No.: 4301], the friction force accompanied with high rotation speed produced fine grain size structure at the welding interface occurred from induced of flow thermo-plastic deformation, that fine grain size structure is blaming as a source of the micro-hardness elevation.

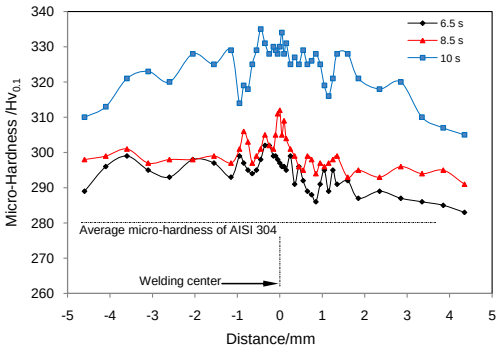

Fig. 10 Micro-hardness profiles for welding interface

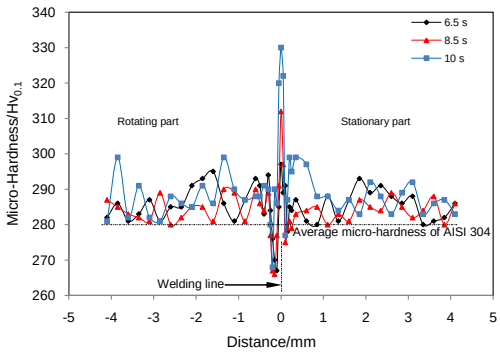

Fig. 11 Micro-hardness profiles for axial direction

Tension-compression tests

Tensile tests were achieved to estimate tensile fracture and determine fracture location. Ultimate tensile strength [UTS] as a function of friction time as presented in Fig. 12. The tensile test results show that UTS increases at shorter friction time, in present study 6.5 s introduced the closest value of UTS to the best metal. Sathiya & al. [25] noted that to obtain high UTS, friction time should be held as short as possible, where their work was carried out on AISI 430-AISI 430 welding joint. Consequently, high rotation speed and short friction time obtained high UTS [6, 21]. Thus, the couple effect of short friction time and high rotation speed on elevation of UTS can show it also in the friction stir welding; Singh & al. [26] illustrated this effect by using AA 6063 alloys.

On the other hand, compression tests performed to discover the compression yield strength with different angles to understand the isotropy of AISI 304 during friction welding process, Fig. 13 exposed the results of compression yield strength with different angles of 0°, 45° and 90° under effect of friction time. As shown in the figure, the values of compression yield strength relative to the base metal reduced with friction time increasing for 0° angle, while 45° and 90° angle kept relatively at the same values. From the compression results its obviously apparent of anisotropy in the yield strength seems under effect of friction time, noted that compression yield strength clearly decreased with longer friction time especially for 0° angle.

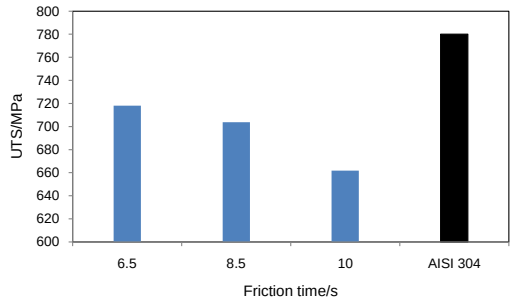

Fig. 12 UTS vs. friction time

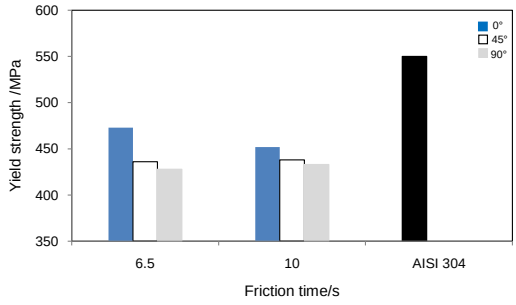

Fig. 13 Compression yield strength vs. friction time

From the above results revealed that the tension-compression joint properties depended on the force applied direction even for different friction time. Therefore, can distinguish such tension-compression properties for friction welding of AISI 304 with itself appeared that UTS and yield compression strength reduced, whereas remain it anisotropy under effect of friction time. UTS decreased from 718 MPa to 661 MPa for 6.5 s to 10 s respectively, in the reducing ratio with increasing friction time from 91 to 84 % relative to the base metal [AISI 304]. While compression yield strength reduced from 473 MPa to 452 MPa for 6.5 s to 10 s respectively for 0° angle direction, thus at longer friction time the ratio is falling from 86 to 82 % relative to AISI 304.

The macro-graphic of tensile fractures found all fractures were neighboring to the interface at TMDZ as shown in Fig. 14, which is obviously in the region that has more micro-hardness attenuation [rotating part], as mentioned in Fig. 11. However, it seemed reduction in the welding region in scale compared with the base metal, this reduction is more clear for 6.5 s relative to the two other cases 8.5 and 10 s, which represented that the 6.5 s is more ductile. on the other side, Fig. 15 shown the macro-graphic of compression test pieces for 6.5 and 10 s with 0°, 45° and 90° angle, while clearly form of drum in the center of the test pieces relative to the base metal. The drum form represented the malleable property, which is clearly observed in the 0° angle comparative to 45° and 90° angle.

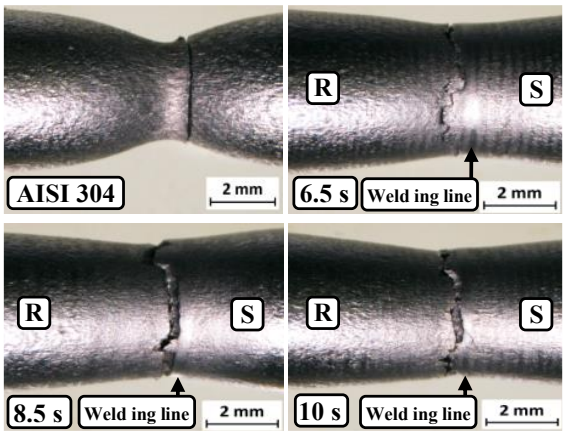

Fig. 14 Tensile fracture position for the three friction times 6.5, 8.5 and 10 s with regard to AISI 304, **R**: Rotating part; **S**: Stationary part

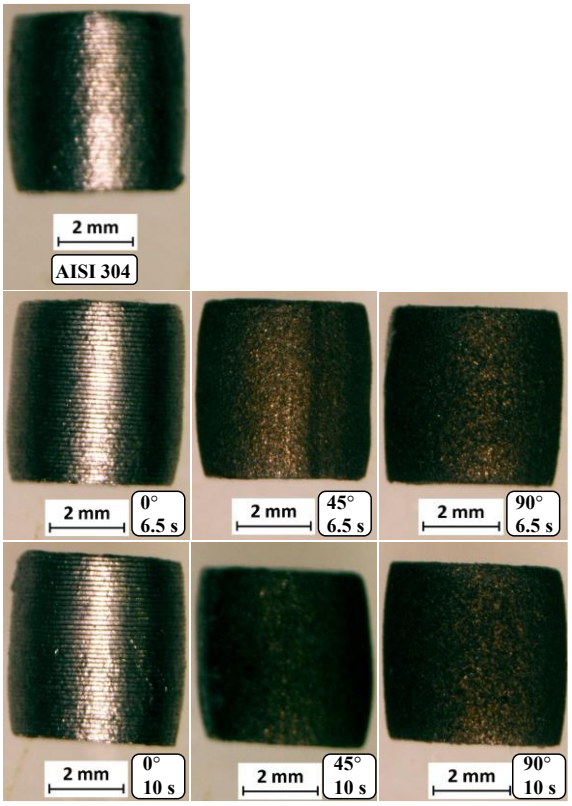

Fig. 15 Compression test pieces with drum form for two friction times 6.5 s and 10 s [0°, 45° and 90°] with regard to AISI 304

SEM observations

Fig. 16 illustrated the fracture surface observation by SEM which is shown that flow lines are very clear as form of spirals shape (fingerprint as machining marks) on the fracture surface for all welding pieces. The accumulation of spiral shape revealed amount of thermo-plastic deformation during friction welding of the austenitic stainless steel, that resulted due to effect of friction pressure and rotation speed, which led the soft metal to flow from center of the piece towards the outside all along the friction phase. It also seemed amount of dimples formation on all fractured surface, which obtained the fractures with mostly ductile mode [2, 10], the nature mode of fracture also mentioned and observed on the macro-graphic of tensile fractures as revealed in Fig. 14.

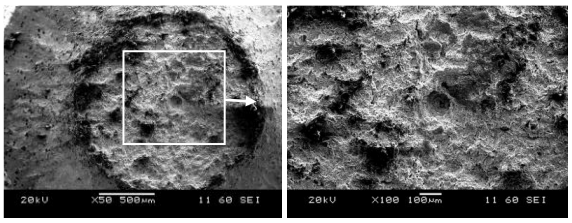

a) AISI 304

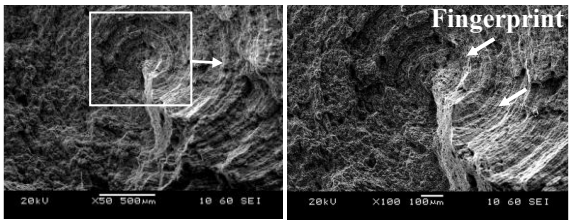

b) 6.5 s

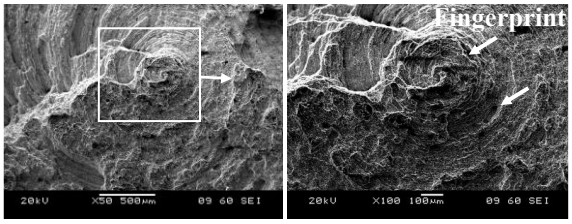

c) 8.5 s

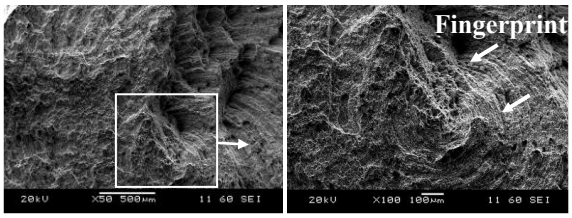

d) 10 s

Fig. 16 Fracture surface of tensile test specimens for different magnifications, for 6.5, 8.5 and 10 s with regard to AISI 304

CONCLUSIONS

The following conclusion can be taken into consideration in manufacturing field at welding types similar to that of AISI 304, where increasing friction time released high amount of heat diffusion which results:

- High amount of flash formation showing mainly, on the stationary side. This is may be explained by high plastic deformation in the friction-welded joints which occurs by large amount at stationary side relative to rotating part,

- Bulky dimension of HPDZ increased because of heat flow released. While TMDZ extended in neighboring with coarse and narrow grains in stationary and rotating side,

- Profile of micro-hardness at maximum level in the welding center, while these values increased from peripheral to the central at the interface,

- Reducing helpful mechanical properties such as UTS and compression yield strength, from compression results its obviously apparent of anisotropy in the yield strength seems under effect of friction time, noted that compression yield strength clearly decreased with longer friction time especially for 0° angle,

- The values of UTS decreased from 718 MPa to 661 MPa for 6.5 s to 10 s respectively, in the reducing ratio with increasing friction time from 91 to 84 % relative to the base metal [AISI 304]. While compression yield strength reduced from 473 MPa to 452 MPa for 6.5 s to 10 s respectively for 0° angle direction. Thus at longer friction time the ratio is falling from 86 to 82 % comparative to AISI 304.

- The tensile fractures found at TMDZ, which is obviously in region of micro-hardness attenuation (rotating part), whereas The drum form in compression test pieces is clearly observed in the 0° angle relative to 45° and 90° angle,

- The final properties of the welded joint depend, therefore, on the friction time. Concerning the grade AISI 304, low friction time provides more homogeneous joint and properties close to those of the base metal. On the other hand, macro-graphic view for welding joint of 6.5 s and 10 s seemed no macro cracks or defects, whereas can distinct large segregation in welding center for 10 s relative to 6.5 s.

REFERENCES

1. R. Satish, V. S. Rao, D. Ananthapadmanaban, B. Ravi: Journal of the Institution of Engineers India Series C, 97, 2016, 121-126. https://doi.org/10.1007/s40032-015-0187-8
2. A. J. Hassan, T. Boukharouba, D. Miroud, S. Ramtani: International Journal of Engineering Transactions B: Applications, 32 (2), 2019, 306-312. DOI: 10.5829/ije.2019.32.02b.16
3. K. S. Sreenivasan, S. S. Kumar, J. Katiravan: Engineering Science and Technology, an International Journal, 22, 2019, 1136-1148. https://doi.org/10.1016/j.jestch.2019.02.010
4. N. Titouche, T. Boukharoubab, S. Amzert, A. J. Hassan, R. Lechelah, S. Ramtani: Journal of Manufacturing Processes, 41, 2019, 73-283. https://doi.org/10.1016/j.jmapro.2019.03.016
5. A. Kurt, I. Uygur, U. Paylasan: Welding Journal, 90, 2011, 02s-106s. http://files.aws.org/wj/supplement/wj201105_s102.pdf
6. E. Bouarroudj, S. Chikh, S. Abdi, D. Miroud: Applied Thermal Engineering, 110, 2017, 543-1553. https://doi.org/10.1016/j.applthermaleng.2016.09.067
7. M. Sahin, H. E. Akata, K. Ozel: Materials and Design, 29, 2008, 265-274. https://doi.org/10.1016/j.matdes.2006.11.004
8. V. Sinka: Acta Metallurgica Slovaca, 20(3), 2014, 287-294. https://doi.org/10.12776/ams.v20i3.312
9. Y. Helal, Z. Boumerzoug: Acta Metallurgica Slovaca, 24(2), 2018, 163-173. https://doi.org/10.12776/ams.v24i2.1049
10. A. J. Hassan, T. Boukharouba, D. Miroud: China Welding, 28(1), 2019, 42-48. https://doi.org/10.12073/j.cw.20180811001
11. M. Kimura, M. Kusaka, K. Kaizu, K. Nakata, K. Nagatsuka: International Journal Advance Manufacture Technology, 82, 2016, 489-499. https://doi.org/10.1007/s00170-015-7384-8
12. L. Peng, L. Jinglong, S. Muhammad, L. Li, X. Jiangtao, Z. Fusheng: Materials and Design, 56, 2014, 649-656. https://doi.org/10.1016/j.matdes.2013.11.065
13. I. Kirik, N. Ozdemir: International Journal of Materials Research, 104(8), 2013, 769-775. https://doi.org/10.3139/146.110917
14. I. Kirik, N. Özdemir, F. Sarsilmaz: Materials Testing, 54(10), 2012, 683-687. https://doi.org/10.3139/120.110379

15. P. Sathiya, S. Aravindan, A. Noorul Haq: International Journal of Advanced Manufacturing Technology, 26, 2005, 505-511. https://doi.org/10.1007/s00170-004-2018-6
16. F. Sassani, J.R. Neelam: Welding Journal, 11(67), 1988, 264s-270s. http://files.aws.org/wj/supplement/WJ_1988_11_s264.pdf
17. P. M. Ajith, T. M. Afsal Husain, P. Sathiya, S. Aravindan: Journal of Iron and Steel Research, International, 22(10), 2015, 954-960. https://doi.org/10.1016/S1006-706X(15)30096-0
18. M. Hazra, K.S. Rao, G.M. Reddy: Journal of Materials Research and Technology, 3(1), 2014, 90-100. http://dx.doi.org/10.1016/j.jmrt.2013.12.001
19. G. I. Khidhir, S. A. Baban: Journal of Materials Research and Technology, 8(2), 2019, 1926-1932. https://doi.org/10.1016/j.jmrt.2019.01.010
20. S. Mercan, S. Aydin, N. Ozdemir: International Journal of Fatigue, 81, 2015, 78-90. https://doi.org/10.1016/j.ijfatigue.2015.07.023
21. N. Özdemir: Material Letters, 59, 2005, 2504-2509. https://doi.org/10.1016/j.matlet.2005.03.034
22. F. C. Liu, T.W. Nelson: Material Characterization, 140, 2018, 39-44. https://doi.org/10.1016/j.matchar.2018.03.035
23. D. Ananthapadmanaban, V. S. Rao, N. Abraham, K. P. Rao: Materials and Design, 30, 2009, 2642-2646. https://doi.org/10.1016/j.matdes.2008.10.030
24. I. Mitelea, V. Budau, C. Craciunescu: Journal of Material Processing Technology, 212, 2012, 1892-1899. http://dx.doi.org/10.1016/j.jmatprotec.2012.04.010
25. P. Sathiya, S. Aravindan, A. NoorulHaq: International Journal of Mechanical and Materials, 3, 2006, 309-318. https://doi.org/10.1007/s10999-007-9037-z
26. R. Singh, S. A. Rizvi, S. P. Tewari: International Journal of Engineering Transactions A: Basics, 30(4), 2017, 597-603. https://doi:10.5829/idosi.ije.2017.30.04a.19

OPEN ACCESS

ACTA METALLURGICA SLOVACA

2020, VOL. 26, NO. 3, 84-94

RESEARCH PAPER

EVALUATION OF THE INFLUENCE OF WASTE GLASS POWDER (WGP) ON THE THERMO-MECHANICAL PERFORMANCE OF FIRED CERAMICS

Abayomi Adewale Akinwande[1], Adeolu Adesoji Adediran[2*], Oluwatosin Abiodun Balogun[1], Oladele Bello[1], Abel Barnabas[1], Oluwayomi Peter Balogun[1], Olanrewaju Seun Adesina[2]

[1] Department of Metallurgical and Materials Engineering, Federal University of Technology Akure, P.M.B. 704, Ondo State, Nigeria.

[2] Department of Mechanical Engineering, Landmark University, Omu- Aran, PMB 1001, Kwara State, Nigeria.

*Corresponding author:dladesoji@gmail.com, abypublications@gmail.com, tel.: 2348162542747, Department of Mechanical Engineering, Landmark University, Omu-Aran, PMB 1001, Kwara State, Nigeria.

Received: 30.04.2020
Accepted: 11.07.2020

ABSTRACT

Effects of elevated temperature on thermo-mechanical properties of fired ceramic products reinforced with waste glass powder (WGP) were reported. Samples were produced by the addition of WGP to clay in varied amount and oven dried samples were fired in an electric furnace which was operated 1200 °C. Compressive and flexural strength were examined at room temperature and at elevated temperatures of 100, 300, 500, 700, and 900 °C. Results showed that, compressive strength and flexural strength reduced at elevated temperatures. Thermal conductivity, diffusivity, and emissivity were higher with increasing WGP content, while thermal expansivity and specific heat capacity were lower as percentage WGP increased in the samples. Results on thermal shock resistance showed that WGP reduced shock resistance in the samples, while the cooling rate increased with the percentage addition of WGP. Impact resistance was noted to decrease in samples when fast cooled from high temperature as the rapid cooling rate was observed to increase with WGP addition in samples. It was concluded that for fired clay products incorporated with WGP, the operating temperature should not exceed 700 °C. Also, in an environment whereby cooling is done by air or/and water, an operating temperature of ≤ 300 °C was recommended.

Keywords: clay, flexural, compressive, emissivity, waste glass powder,

INTRODUCTION

Fired clay is a kind of ceramic material made from moulded clay by the process of heat in order to make it hard and strong. It has good resistance to high temperature, having a fusion point higher than 1600 ºC and is corrosion resistant [1,2]. Fired clay materials are used for lining of furnaces as fired bricks and for industrial production of white wares and other products. Some fired bricks are employed in masonry for housing and for roof tiles application [3]. Properties of fired clay products include porosity, high temperature resistance, wear resistance, and high compression. These properties can vary with temperature, which birth the study of the behaviour of fired bricks under different temperature conditions. This study considered thermo-mechanical behaviour of fired clay samples at different thermal conditions because performance of ceramic materials tends to change at elevated temperature. Studies on thermal behaviour of fired ceramics may reveal how additives affect thermal and mechanical behaviour of fired clay bricks and possibly provide information on possible application of such products. In previous study, [4] observed increased bulk and true density as eggshell increased in fired bricks. For water absorption, the value reduced with increasing egg shell content. Coefficient of thermal expansion was noticed to reduce in the samples. At 20 wt. % eggshell addition, compressive strength, and hardness were highest at 8.28 MPa and 8.79 HV respectively while thermal expansion coefficient was lowest at 2.3652 x 10^{-6}/K.

In another report on thermal behaviour of insulating brick developed using saw dust additive [5], ball clay and kaolin used were sieved to 0- 45µm, 45-53 µm, 63-90 µm, 90 – 125 µm and 125-154 µm. The saw dust was sieved to 0-125 µm, 125-154 µm, 154-180 µm and 355-425 µm and was added to the mixture of ball clay and kaolin. Results obtained showed that density and thermal conductivity reduced as particle sizes of kaolin and ball clay increased for different sizes of saw dust considered. Specific heat capacity increased while coefficient of thermal diffusivity reduced as particle sizes of kaolin and clay increased. The effect of coal and wheat husk addition on thermal properties of clay bricks was reported by [6]. From their work, it was observed that thermal conductivity reduced as percentage coal and wheat husk increased from 0 to 50 wt. %. Wheat husk was more effective in improving insulation properties of the clay bricks compared to charcoal due to increased pores formed. Also, it gave reduction of up to 92 % in thermal conductivity. Thermal diffusivity was shown to reduce with increased additives and decrease between 15 and 60 % for charcoal additives of 5 to 50 wt. % while that of wheat husk was 44 to 92 %. Mechanical strength was noted to decrease with increase in water absorption, apparent porosity, and firing shrinkage. Wheat was more effective for insulation than charcoal.

MATERIAL AND PREPARATION PROCEDURE

Clay was obtained from a borrow pit in Awule community, Akure (latitude 7.250771 º, longitude 5.210266 º) in Ondo state, Nigeria by excavation using a shovel and collected into a container. Waste glass bottles which were obtained from a local waste glass seller, were employed in this study. The clay was treated by mixing with water in a container and allowed to settle for 2 days, after which the suspended water was poured away. The clay was further treated by adding fresh water, stirring and allowing settling for another 2 days. The suspended water was poured away and the left over clay was spread in open atmosphere to sundry for 3 days. Dried clay was crushed, milled (using modified ball mill, serial number F-N 178) and sieved to -150 µm before been packed into a container. Similar protocol was obtained with waste glass using an electric sieve shaker. Waste glass powder (WGP) and clay powder sieved to -150 µm were collected, separated, and used in sample preparation.

The clay and waste glass powder were thoroughly mixed in an electric mixer in varying amount. WGP was added to clay in the proportion of 0 to 40 wt. % at 5 wt. % interval. Water was added to clay in the ratio of 1:3 and mixed thoroughly. The slurry obtained was compressed (at 10 MPa) into cylindrical moulds of diameter 50 mm, height 100 mm and diameter 40 mm and height 20 mm, rectangular moulds of dimensions 150 mm × 150 mm × 150 mm, 400 mm x 100 mm x 100 mm and 190 mm × 90 mm × 90 mm. Green bricks produced which initially were left in open air for 24 hours for stability were oven dried for 12 hours at 110 ºC after which they were fired in an electric furnace at 5 ºC/min until 1200 ºC was attained. The samples were soaked for 2 hours at that temperature before been allowed to cool to room temperature and taken out for examination.

(a)

(b)

Fig. 1 Pictures of (a) electric furnace used in firing and (b) bricks samples

TEST PROCEDURE

Mechanical properties

Mechanical properties were studied by initially carrying out compressive strength (for rectangular samples of dimension 150 x 150 x 150 mm) and flexural strength (for rectangular samples of dimension 400 × 100 × 100 mm) test on brick samples at 26–29 ºC (room temperature). Effect of heat on mechanical properties of samples were evaluated by heating to 100, 300, 500, 700, 900, and 1000 ºC, soaked for 1 hour and tested for compressive strength and flexural strength immediately they were brought out from the furnace. The test was carried out in line with [7] for compressive strength and [8] for flexural strength. Percentage reduction in strength (Δ‰) was evaluated using Equation (1) for that of compressive strength and Equation (2) for flexural strength. Flexural strain at fracture (for different temperatures) was evaluated using Equation (3).

$$\Delta C‰ = \frac{C_n - C_i}{C_i} \quad (1.)$$

$$\Delta F‰ = \frac{F_n - F_i}{F_i} \quad (2.)$$

$$\text{Flexural strain } (\alpha) = \frac{6dt}{h^2} \quad (3.)$$

Where, ΔC‰ is percentage reduction in compressive strength,
ΔF‰ is percentage reduction in flexural strength,
F_i/C_i is Flexural/compressive strength at initial temperature,
F_n/C_n is Flexural/compressive strength at new/next temperature,
d is the recorded deflection (mm) at different temperatures,
t is thickness of sample and
h is the distance between two supports.

Resistance to impact was examined by applying a load rate of 5 N/min at the centre of the brick samples from a height of 50 cm until fracture occurred. The number of cycle was recorded for each sample at room temperature (26 – 29 ºC) and at temperatures of 100, 300, 500, 700, 900, and 1000 ºC.

Thermal properties

Cylindrical samples of diameter 40 mm and height 20 mm were tested for thermal conductivity using hot plate method in line with [9], linear and volumetric thermal expansion were evaluated in line with [10] by measuring the dimension of each brick sample at various temperature and evaluated using Equation (4) and (5). Specific heat capacity was accessed by method of mixture using cylindrical samples of diameter 50 mm and height 100 mm [11] while thermal emissivity was examined in line with [12] and thermal diffusivity [13] was calculated using Equation (6).

$$\text{Linear expansion} = \frac{L_2 - L_1}{L_1 \Delta T} \quad (4.)$$

$$\text{Volumetric expansion} = \frac{V_2 - V_1}{V_1 \Delta T} \quad (5.)$$

$$\text{Thermal diffusivity} = \frac{k}{\gamma C_p} \quad (6.)$$

Where L_1 is initial length at previous temperature (m),
L_2 is final length at new temperature (m),
V_1 is initial volume at previous temperature (m^3),
V_2 is final volume at new temperature (m^3),
ΔT is temperature difference (K),
K is thermal conductivity,
γ is density and
C_p is specific heat capacity.

Thermal shock resistance and cooling rate

Thermal shock resistance was determined by three experimental procedures, while cooling rate was evaluated at normalized cooling and rapid cooling;

I. Exp. 1: rectangular bricks samples were heated to 1000 ºC at 5 ºC/min and soaked for 1 hour and then held in air for 10 mins. The process was continued until crack occurred and the number of cycles was recorded in line with [14].
II. Exp. 2: heating samples to 300 ºC at 5 ºC/min, soaking for 1 hour and holding the samples in open air. Air was blown on the samples at room temperature at rate of 12.2 cm^3/s for 10 minutes. The procedure was followed until crack occurred and the number of cycles recorded.
III. Exp. 3: heating samples to 300 ºC at 5 ºC/min, soaking for 1 hour and holding the samples in open air and allowing drip of water 8.38 cm^3/s for 10 mins. The process continued until crack appeared and the number of cycles recorded.
IV. Normalized Cooling rates of samples was evaluated by heating samples to 300, 500, 700, and 900 ºC at 5 ºC/min held for 30 mins and allowed to cool to room temperature in air. Cooling time to room temperature was observed, the cooling rate was evaluated using Equation (7).
V. Fast cooling rate was measured by heating samples to 300, 500, 700, and 900 ºC at 5 ºC/min, held for 30 mins and cooled to room temperature (26 ºC) by applying water at a fast rate (fast cooling rate) of 16.8 cm^3/s on the samples. The time taken was recorded and cooling rate was evaluated using Equation (7). Cooling rate coefficient was obtained as ratio of normalized cooling rate to high cooling rate.

$$\text{Cooling rate} = \frac{T_2 - T_1}{A\ x\ t} \quad (7.)$$

T_2 is final temperature,
T_1 is initial temperature,
A is cross sectional area of sample and
t. time taken to cool.

RESULTS AND DISCUSSION

Morphological representation of some samples at room temperature (26 °C)

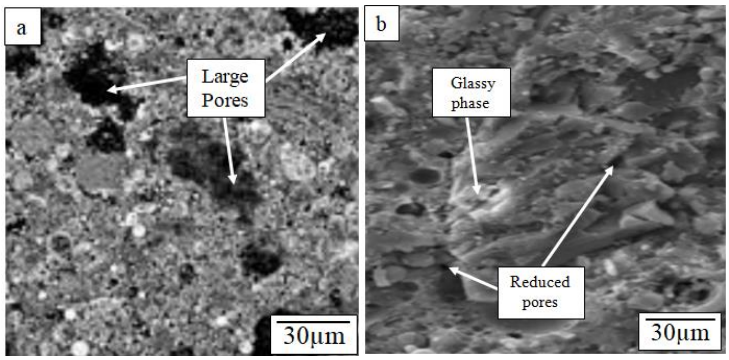

Fig. 2 SEM image samples at (a) 0 wt. % WGP (b) 30 wt. % WGP at room temperature

Figure 2 (a) shows the SEM image of brick sample with 0 % WGP addition at room temperature of 26 °C. Pores are observed in 0 wt. % sample, when compared with bricks containing 30 wt. % WGP which had reduced pores. This explains reason for lower compressive and flexural strength in sample with 0 % WGP when compared with that of 30 wt. % WGP. Figure 2b shows image of 30 wt. % WGP addition, porosity reduced and the presence of glass luster as a result of glassy phase formed at high temperature was evident. The bond between WGP, clay particles and the strong glassy phase formed in samples resulted into improved strength compared to the one of 0 wt. % WGP as reported in Table 1.

Thermo-Mechanical properties at room temperature

a. Mechanical strength at room temperature

Table 1 Compressive and Flexural strength at room temperature (26 °C)

%WGP	0	5	10	15	20	25	30	35	40
CS	7.4	8.2	9.7	11.3	13.3	`13.7	14.5	12.1	11.3
FS	1.05	1.24	1.47	1.79	2.50	2.61	2.63	2.31	2.17
RS	12	12	13	15	18	16	16	14	12
FSt(x 10^{-3})	11	8.1	6.3	4.1	3.3	1.8	0.9	0.6	0.4

CS represents compressive strength (MPa),
FS represents Flexural strength (MPa),
RS represents resistance to impact (number of cycles) and
FSt represents flexural strain (mm/mm).

As WGP increased in proportion, mechanical strength increased (Figure 3). WGP particles filled up the pores in the clay matrix, thereby reducing porosity. As temperature increased during firing, dehydration increased, compactment and stabilization were also enhanced at temperatures between 20 to 600 ºC. As the temperature was being raised, chemical reaction occurred leading to fusion of the clay and WGP particles, which resulted in enhanced strength and hardness in the samples [15][16]. At above 900 ºC, vitrification occurred leading to formation of glassy phase [17] which proportion is dependent on the proportion of WGP added. The glassy phase formed further covered the pores leading to reduction in porosity and enhanced compactment as confirmed in [18]. The consequent result is increased strength and hardness. Care was taken not to fire above 1200 ºC due to possibility of expansion of the glassy phase so as not to allow crack or storage of residual stress. However, glassy phase is brittle; hence, addition of WGP particles to a certain extent may result in decrease in strength which explains the reduction of compressive and flexural strength at 35 and 40 wt. % additions (Table 1). Resistance to impact increased from 0 wt. % to 20 wt. % and reduced further as WGP content increased due to increased glassy phase. The results reported in this study are in line with [19][20], where increase in strength was observed with increasing waste glass addition. Flexural strain reduced continuously from 0 wt. % to 40 wt. % of WGP as indicated in Table 1.

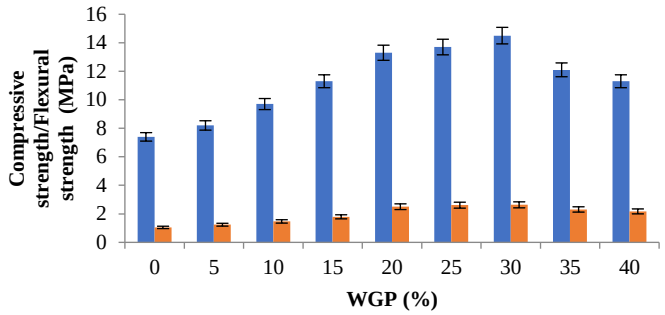

Fig. 3 Variation in compressive/flexural strength at increasing WGP proportion

Thermal properties

a. Thermal conductivity

With increasing waste glass powder (WGP) content, thermal conductivity was rising (Figure 4) which is attributed to reduction in porosity. These pores serve as air trap and reduce thermal transfer since air has poor thermal conductivity. This is backed up with the fact that presence of WGP causes lower volume of pores since the pores are filled with glass powder particles, hence resulting in increased thermal conductivity. The observation is also linked to interlocking of particle of the waste glass powder and clay within the structure because of well graded particle size distribution [5].

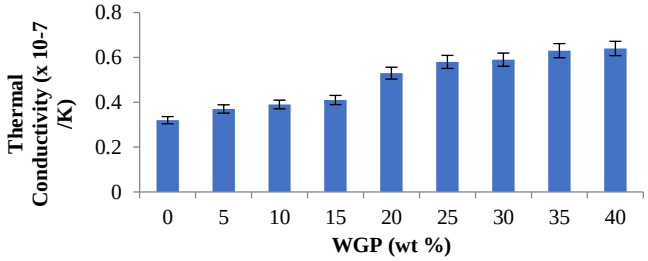

Fig. 4 Effects of WGP on thermal conductivity

Coupled with this, is reduced interparticle distance resulting in low porosity, leading to high bond strength which enhanced thermal movement within the solid clay body. The phenomenon led to high internal vibration of particles when the body was thermally activated thereby resulting in increased transfer of thermal energy from one particle to another. Pore formers has been known to increase pores in bricks leading to reduction in thermal conductivity as reported in [5][21][22] which is due to the fact that the pores serve as air trap and since air is poor conductor, this leads to decrease in thermal conductivity. On the other hand, addition of waste glass in fired bricks results in reduction in porosity which eventually amount to increase in thermal conductivity as observed in this study

b. Thermal diffusivity and emissivity

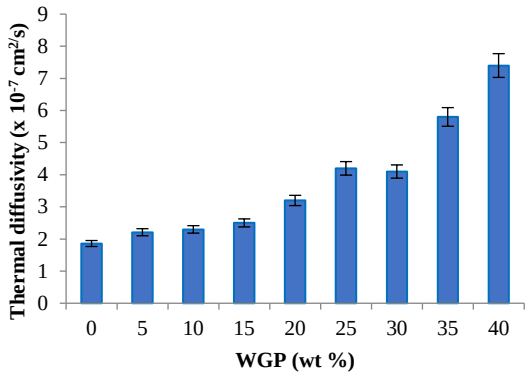

Fig. 5a Effect of WGP content on thermal diffusivity

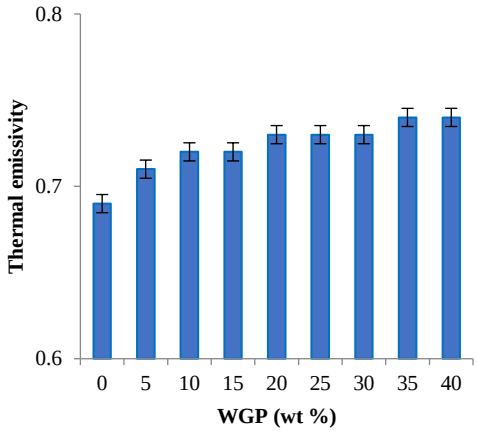

Fig. 5b Effect of WGP content on thermal emissivity

Thermal diffusivity refers to rate at which heat is transferred from the hot end of a material to the cold end of such material [23], while emissivity refers to the ability of a body to emit thermal radiation at the surface [24]. Diffusivity which was evaluated at 300 ºC was observed to be higher with additional WGP content (Figure 5a). This occurred due to reduced porosity leading to shorter interparticle distance and stronger bond between particles, which enabled easy transmission and diffusion of heat within particles. Emissivity increased gradually as WGP increased up to 20 wt. % WGP remained constant up to 35 and 40 wt. % of WGP after which there was progressive rise up to 40 wt. % (Figure 5b). High absorptivity of heat may result into higher emissivity due to lower capacity to retain heat as interparticle distance reduced. Increased porosity results into lower diffusivity as reported in [6]. In this study, the results showed increment in diffusivity due to lower porosity.

c. Specific heat capacity

Specific heat capacity is the "amount of heat needed to raise the temperature of a unit mass of a material by 1K" [25]. The higher the value, the higher the amount of heat energy required to raise the temperature of a unit mass of the object by 1K. Porous materials require much higher energy to raise temperature and in insulating bricks, these pores are filled with air which has poor conducting properties.

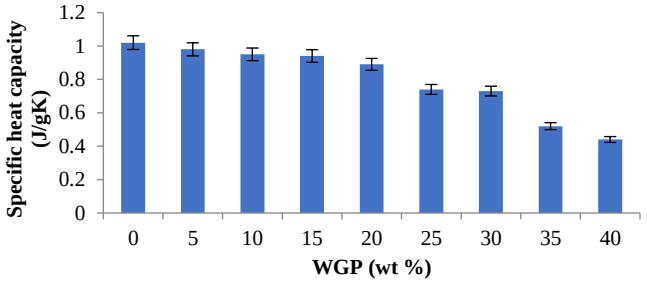

Fig. 6 Effect of WGP content on specific heat capacity

As the pores reduced and particles bond became stronger, the heat energy requirement became lower. This explains reason for the reduction in specific heat capacity as WGP increased (Figure 6). Increase in porosity reduces interparticle distance, hence, requires higher energy to raise the temperature of unit mass by 1K as reported in [5]. Reduction in porosity on the hand, led to shorter interparticle distance, thereby enhancing cohesion. Therefore, decrease in specific heat capacity with higher content of the additive was observed in this study (Figure 6) contrary to the outcome in [5].

Thermo-Mechanical performance at elevated temperature

a. Effects of increased temperature on compressive strength.

Table 2 Percentage reduction in compressive strength at different temperature for WGP-bricks

%WGP content in samples	Compressive strength at 26 °C	Percentage reduction in compressive strength (ΔC‰)					
		100 °C	300 °C	500 °C	700 °C	900 °C	1000 °C
0	7.4	2.8	4.6	6.9	8.9	17.3	22.5
5	8.2	2.3	4.1	6.8	8.1	16.5	20.6
10	9.7	1.2	4.3	6.6	7.7	15.3	19.3
15	11.3	0.9	3.7	5.5	6.9	13.8	18.4
20	13.3	0.8	3.5	5.2	7.6	13.5	16.8
25	13.7	0.6	3.5	4.9	4.7	12.5	15.9
30	14.5	0.6	3.4	4.3	4.2	10.5	11.6
35	12.1	0.6	3.7	4.3	5.1	16.0	14.4
40	11.3	0.6	3.5	6.7	5.3	14.8	18.7

At elevated temperature (Table 2 and Figure 7), compressive strength depreciated due to gradual weakening of the bond between clay particles as well as reduction in adhesion between WGP particles and clay particles. As WGP increased in the samples, the value of ΔC‰ reduced, due to enhanced strength of adhesion between particles as WGP increased in the samples. Going from 100 °C to 700 °C for 0 to 40 wt. % WGP, percentage reduction in compressive strength increased gradually, for each WGP content ranging from 2.8 % to 8.9 % for 0 % WG, 2.3 to 8.1 % for 5 wt. % WGP, 1.2 to 7.7 % for 10 wt. % of WGP, 0.9 to 6.9 % for 15 wt. % of WGP, 0.8 to 7.6 % for 20 wt. % WGP, 0.6 to 4.7 % for 25 wt. % WGP, 0.6 to 4.2 % for 30 wt. % WGP, 0.6 to 5.1 % for 35 wt. % WGP and 0.6 to 5.3 % for 40 wt. % WGP. It was observed that at 100 ºC, ΔC‰ value remained constant at 25 to 40 wt. % WGP content of 0.6 %.

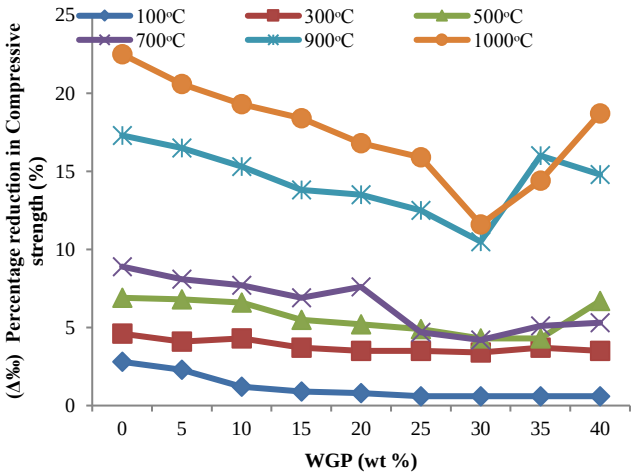

Fig. 7 Percentage reduction in compressive strength at increased temperature

On each temperature of 100 to 700 °C, ΔC‰ value reduced as WGP content increased. From 700 to 900 °C for each sample, ΔC‰ value reduced drastically from 8.9 to 17.3 % for 0 wt. % WGP, 8.1 to 16.5 % for 5 wt. % WGP, 7.7 % to 15.3 % for 10 wt. % WGP, 6.9 to 13.8 % for 15 wt. % WGP, 7.6 to 13.5 % for 20 wt. % WGP, 4.7 to 12.5 % for 25 wt. % WGP, 4.2 to 10.5 % for 30 wt. % WGP, 5.1 to 16 % for 35 wt. % WGP and 5.3 to 14.8 % for 40 wt. % WGP. At 1000 °C, ΔC‰ further fell to 22.5 %, 20.6 %, 19.3 %, 18.4 %, 16.8 %, 15.9 %, 11.6 %, 14.4 % and 18.7 % for 0, 5, 10, 15, 20, 25, 30, 35 and 40 WGP content respectively. The decrease for each of the mix proportion at 900 and 1000 °C is above 10 %, indicating that at temperature up to 900 °C, there was drastic weakening of the bond and degradation of the glass phase present, therefore, the working temperature of this clay samples under consideration is ≤ 700 °C. It was further observed that there was a measure of stability for samples with 25 and 30 wt. % addition of WGP which ΔC‰ values between 100 and 700 °C were less than 5 %, showing that WGP of 25 and 30 wt. %, will be most stable when operation temperature is ≤ 700 °C, beyond that, there could be degradation and drastic depreciation in strength.

b. Effects of increased temperature on flexural strength

Table 3 Percentage reduction in flexural strength at different temperatures

% WGP content in samples	Flexural strength at 26 °C	Percentage reduction in flexural strength (ΔF ‰) 100 °C	300 °C	500 °C	700 °C	900 °C	1000 °C
0	1.05	2.4	3.9	4.7	3.9	12.5	17.3
5	1.24	2.1	3.4	3.9	4.2	11.7	15.8
10	1.47	0.9	2.5	3.4	3.5	11.4	13.6
15	1.79	0.8	2.1	3.3	3.5	9.8	12.8
20	2.50	0.6	2.1	2.9	3.1	7.2	10.2
25	2.61	0.5	1.9	2.4	2.9	6.8	9.8
30	2.63	0.4	1.7	2.1	2.3	6.3	9.7
35	2.31	0.3	1.2	2.3	2.5	6.4	9.9
40	2.17	0.3	0.8	2.1	2.8	8.8	10.1

Flexural strength followed almost the same pattern as obtained in compressive strength in that, at increased temperature (Table 3 and Figure 8), flexural strength reduced, also, due to gradual weakening of the cohesive bond between clay particles plus reduction in adhesion between particles of the WGP additives and clay particles. As WGP increased in the samples, the value of ΔF‰ (where ΔF‰ denotes percentage reduction in flexural strength from one temperature to the next) reduced, due to the effect of increased strength of adhesion between particles as WGP increased in the samples.

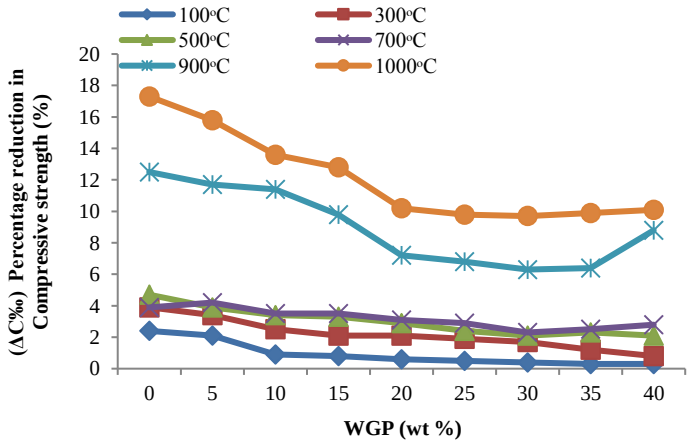

Fig. 8 Percentage reduction in flexural strength at increased temperature

Going from 100 °C to 700 °C for 0 to 50 wt. % WGP, percentage reduction in flexural strength ΔF‰ increased gradually, for each WGP content, ranging from 2.4 % to 3.9 % for 0 % WG, 2.1 to 4.2 % for 5 wt. % WGP, 0.9 to 3.5 % for 10 wt. % of WGP, 0.8 to 3.5 % for 15 wt. % of WGP, 0.6 to 3.1 % for 20 wt. % WGP, 0.5 to 2.9 % for 25 wt. % WGP, 0.4 to 2.3 % for 30 wt. % WGP, 0.3 to 2.5 % for 35 wt. % WGP and 0.3 to 2.8 % for 40 wt. % WGP. It was observed that at 100 °C, ΔF‰ value remained constant at 35 and 40 wt. % WGP content of 0.3 %. At each temperature of 100 to 700 °C, ΔF‰ value reduced as WGP content increased. From 700 to 900 °C for each sample, ΔF‰ value also reduced drastically just like in the case of ΔC‰ for compressive strength. The value (700 to 900 °C) was from 3.9 to 12.5 % for 0 wt. % WGP, 4.2 to 11.7 % for 5 wt. % WGP, 3.5 % to 11.4 % for 10 wt. % WGP, 3.5 to 9.8 % for 15 wt. % WGP, 3.1 to 7.2 % for 20 wt. % WGP, 2.9 to 6.8 % for 25 wt. % WGP, 2.3 to 6.3 % for 30 wt. % WGP, 2.5 to 6.4 % for 35 wt. % WGP and 2.8 to 8.8 % for 40 wt. % WGP. At 1000 °C, ΔF‰ further fell to 17.3 %, 15.8 %, 13.6 %, 12.8 %, 10.2 %, 9.8 %, 9.7 %, 9.9 % and 10.1 % for 0, 5, 10, 15, 20, 25, 30, 35 and 40 WGP content respectively. The high increase in value was attributed to the fact that at temperature up to 900 °C, there was drastic weakening of the bond and degradation of the glass phase present. This further confirms that, the working temperature of ceramic samples in this study is less than ≤ 700 °C.

c. Evaluation of flexural strain at different temperature

Table 4 Flexural strain at different temperatures

% WGP content in samples	Flexural strain at 26-29 °C	Flexural strain (at fracture) at different temperatures (α) 100 °C	300 °C	500 °C	700 °C	900 °C	1000 °C
0	0.0110	0.0113	0.0125	0.0137	0.0158	0.0213	0.0286
5	0.0081	0.0115	0.0121	0.0137	0.0149	0.0204	0.0256
10	0.0063	0.0111	0.0146	0.0131	0.0132	0.0195	0.0234
15	0.0041	0.0101	0.0118	0.0118	0.0122	0.0142	0.0196
20	0.0033	0.0087	0.0098	0.0097	0.0117	0.0118	0.0178
25	0.0018	0.0056	0.0098	0.0056	0.0099	0.0103	0.0165
30	0.0009	0.0056	0.0099	0.0023	0.0096	0.0089	0.0146
35	0.0006	0.0078	0.0087	0.0014	0.0056	0.0076	0.0139
40	0.0004	0.0106	0.0086	0.0011	0.0034	0.0053	0.0133

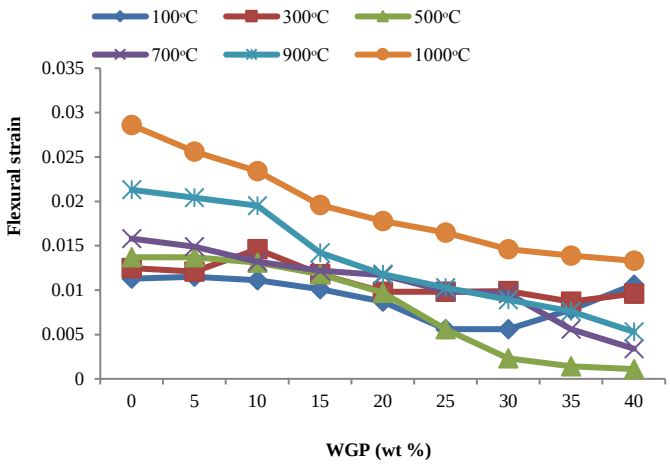

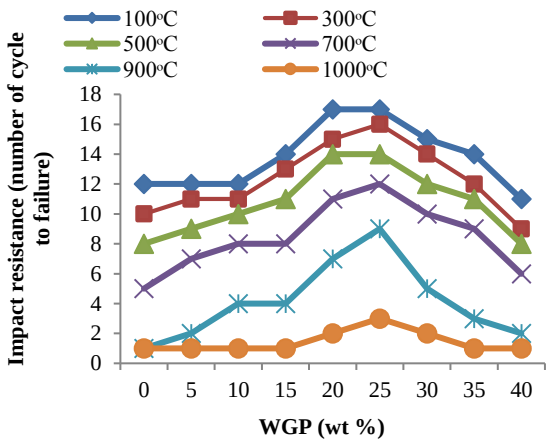

Fig. 9 Effects of increased temperature on flexural strain

Flexural strain was observed to increase at increased temperature (Table 4 and Figure 9), while flexural strength reduced with increased temperature as a result of the weakening of the bond and easier flow of the particles, aided by thermal stress. At room temperature, flexural strain reduced with increased WGP proportion in samples. At 100 ºC, the value reduced from 0 wt. % to 30 wt. % addictive after which there was increase in the value at 35 – 40 wt. % due to increased flow which was attributed to increased thermal energy of particles. At 300 ºC, strain reduced from 0 wt. % of additive, peaked at 10 wt. % additive and further reduced as WGP proportion increased. At 500 to 1000 ºC, there was reduction in strain as WGP increased from 0 wt. %. Going from 100 to 1000 °C, for each mix proportion, strain was observed to increase due to increased flow.

d. Effects of increased temperature on impact resistance

Table 5 Number of cycle to failure at different temperatures

% WGP content in samples	Number of cycle to failure at 26 °C	Impact resistance (number of cycle to failure) 100 °C	300 °C	500 °C	700 °C	900 °C	1000 °C
0	12	12	10	8	5	1	1
5	12	12	11	9	7	2	1
10	13	12	11	10	8	4	1
15	15	14	13	11	8	4	1
20	17	17	15	14	11	7	2
25	18	17	16	14	12	9	3
30	16	15	14	12	10	5	2
35	14	14	12	11	9	3	1
40	12	12	10	8	5	1	1

Impact resistance was evaluated by number of cycle to failure for samples at different temperatures. The value at room temperate (26 °C) increased as WGP amount increased up to 25 wt. % before declining at 30 wt. % (Table 5 and figure 10). The resistance to impact was due to closeness of particles and strength of bond between particles. At 30 wt. % the brittle nature of the glassy phase had a toll on impact resistance which explains reduction in the number of cycles to failure from 30 to 40 wt. %.

At increased temperature, the instability of the particles due to increased excitation resulted in increased kinetic energies of particle and led to lower compactment of particles. This led to lower adhesion between clay and glass particles, thereby causing reduction in resistance to impact.

At 100 ºC, impact resistance for all samples remained almost constant due to lower stress level induced in the samples. As temperature increased, from 300 to 1000 ºC, residual stress increased in the samples resulting in further reduction in

Figure 10: Effects of increased temperature on impact resistance.

impact resistance evaluated by number of cycles to fracture. At 700 to 900 to 1000 °C, the impact resistance depreciated greatly, owing to increased residual stress and instability of particles as a result of thermal excitation. From 26 °C to 300 °C, difference in number of cycle to failure for all samples was in the range of 1 to 2 which explains a relative stability in impact resistance at those temperatures for all samples. At application which requires impact, temperature should be ≤ 300 °C.

e. Linear and volumetric thermal expansion at different temperatures

Table 6 Variation in Linear thermal expansion at different temperature

% WGP content in samples	Linear thermal expansion at different temperature 100 °C (x10^{-5}/K)	300 °C (x10^{-5}/K)	500 °C (x10^{-5}/K)	700 °C (x10^{-5}/K)	900 °C (x10^{-5}/K)	1000 °C (x10^{-5}/K)
0	0	0.97	3.92	5.27	8.28	12.37
5	0	0.88	3.34	5.05	7.45	12.04
10	0	0	2.77	4.79	7.74	11.45
15	0	0	2.42	4.54	6.73	11.13
20	0	0	2.19	4.13	6.45	7.12
25	0	0	1.83	1.84	3.13	6.43
30	0	-1.24	1.14	1.75	3.79	8.43
35	0	-0.89	2.71	2.63	8.24	7.34
40	0	-0.15	2.71	2.14	8.24	6.32

Increase in thermal conductivity on the other hand brought about lowering of thermal expansivity since particles are bonded strongly. Thermal expansivity reduced with increasing WGP proportion leading to strong adhesion between clay and WGP particles. The results for thermal expansivity agrees with [4] which also recorded reduction in thermal expansion coefficient as egg shell content increased in fired clay but contrary to result obtained in [6], whereby thermal conductivity reduced with increased content of additive. In this study and in [4], porosity reduced with increased additive while in [6] porosity increased with increased additive which explained the difference in that, with reduced porosity, thermal conductivity increased, and vice versa, in the case of increased porosity with increased proportion of additives. Linear and volumetric thermal expansivity were evaluated at different temperatures of 100 to 1000 ºC by measuring change in dimension at those temperatures. It was observed that at higher temperature, linear expansivity increased (Table 6 and Figure 11) owing to weaker bond within particles, which led to increase in interparticle distance, hence resulting in higher degree of expansion.

For 100 ºC, there was no linear expansivity indicating dimensional stability at that temperature because of the fact that the thermal stress exposure was not enough to cause substantial weakening of the bond between particles. At 300 ºC, the linear expansion only occurred at 0 and 5 wt. % of WGP while there was contraction for samples containing 30 to 40 wt. % WGP proportion. For samples containing 10 to 25 wt. %, there was 0 values for expansion due to thermal stability at that temperature. This indicates that the thermal stress was only enough to cause vibration of the particles about their mean position, without any dissociation of the bond, even though the strength of the bond reduced which was

explained by lower reduction in compressive and flexural strength at this temperature (Table 2 and 3). It was further observed that at temperature (300 to 500 °C), linear thermal expansivity reduced from 0 to 30 wt. % owing to the strong bond and lower heat capacity of the glassy phase at such temperature, but at 35 and 40 wt. %, the value increased indicating weakening of the bond. Increment in expansivity value from 500 to 700 ºC was 57 % from 5.27 to 8.28 $x10^{-5}$/K for 0 wt. %, 47.5 % from 5.05 to 7.45 $x10^{-5}$ /K for 5 wt. %, 61.6 % from 4.79 to 7.74 $x10^{-5}$ /K for 10 wt. %, 48.2 % from 4.54 to 6.73 $x10^{-5}$ /K for 15 wt. %, 56.2 % from 4.13 to 6.45 $x10^{-5}$ /K for 20 wt. %, 70 % from 1.84 to 3.13 $x10^{-5}$/K for 25 wt %, 116.6 % from 1.75 to 3.79 $x10^{-5}$ /K for 30 wt. %, 213 % from 2.63 to 8.24 $x10^{-5}$ /K for 35 wt. % and 285 % from 2.14 to 8.24 $x10^{-5}$/K for 40 wt. %.

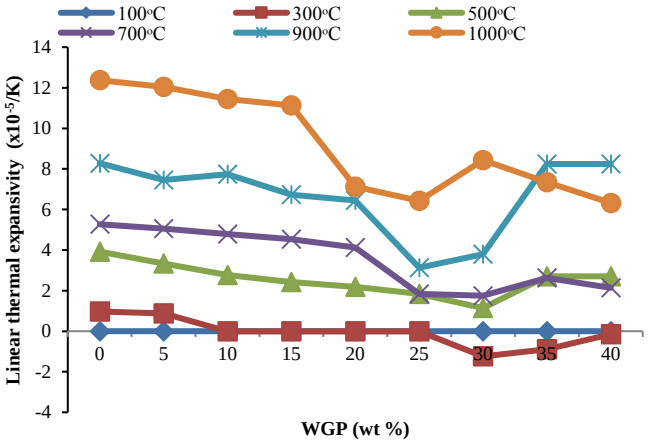

Fig. 11 Effects of WGP on linear thermal expansion at different temperatures

From this percentage increase, it was noted that as WGP content increased, the percentage rise in expansivity increased, indicating high level of degradation of the glassy phase and weakening of the bond between particles. This still further confirms that the working temperature of the set of ceramic samples analyzed in this study should not be greater than 700 °C. Percentage increase in expansivity increased at 1000 ºC at 49 %, 62 %, 48 %, 65 %, 63 %, 127 %, 70 %, for 0 to 30 wt. % additions. This can be attributed to the further degradation of the glassy phase and weakened adhesion between the clay and WGP. In the case of 35 and 40 wt. % WGP, expansivity reduced from 8.24 for both, to 7.34 and 6.32 $x10^{-5}$/K respectively due to slight contraction.

Table 7 Variation in Volumetric thermal expansion at different temperature

%WGP content in samples	Volumetric thermal expansion at different temperature					
	100 ºC ($x10^{-5}$/K)	300 ºC ($x10^{-5}$/K)	500 ºC ($x10^{-5}$/K)	700 ºC ($x10^{-5}$/K)	900 ºC ($x10^{-5}$/K)	1000 ºC ($x10^{-5}$/K)
0	0	0.262	0.273	0.345	0.412	0.852
5	0	0.215	0.258	0.322	0.378	0.794
10	0	0	0.229	0.305	0.354	0.772
15	0	0	0.194	0.215	0.322	0.764
20	0	0	0.183	0.217	0.294	0.621
25	0	0	0.164	0.217	0.293	0.574
30	0	-0.184	0.154	0.158	0.214	0.525
35	0	-0.172	0.132	0.149	0.233	0.574
40	0	-0.198	-0.121	0.137	0.199	0.599

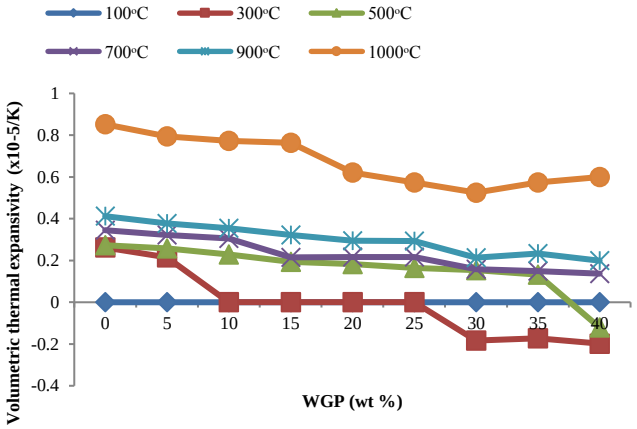

Fig. 12 Effects of WGP on volumetric thermal expansion at different temperatures

Volumetric thermal expansivity was evaluated by measuring increment in the dimension of the rectangular prism sample. This property follows the same trend as in the case of linear expansion with the same reason at each temperature. With increased temperature, the value increased and with increasing WGP content, the trend reduced down the line.

Thermal shock resistance and cooling rate

a. Experimental results on thermal shock resistance

Effects of WGP on thermal shock resistance were measured using 3 ways of experimenting:

Table 8 Number of cycle at which crack appeared for Exp. 1, 2 and 3

WGP	0	5	10	15	20	25	30	35	40
Number of cycles in Exp. 1	21	22	23	15	14	16	16	10	10
Number of cycles in Exp. 2	65	62	60	60	43	36	34	29	21
Number of cycles in Exp. 3	44	44	45	43	38	36	34	22	19

Figure 13 shows the number of cycles for each case. For case Exp. 1, the number of cycles after samples was exposed to 1000 ºC increased from 21 to 23 for 0 wt. % to 10 wt. % of WGP, at further increased amount of WGP, the value reduced to 15 at 15 wt. % content remained constant until it fell at 35 wt. % of the additive. Going by [26], WGP content should not be more than 10 % in bricks for refractory. For Exp. 2, shock resistance based on number of cycles recorded decreased from 65 cycles to 21 cycles from 0 to 40 wt. % of WGP. This is due to the brittle nature of the glass phase formed and can be deduced that increased proportion of WGP particles resulted in lower thermal shock resistance of bricks exposed to air cooling. For Exp. 3, water was employed as a means of cooling; the shock resistance measured by number of cycles, reduced from 0 wt. % WGP content to 40 wt. % WGP content. Therefore, thermal shock resistance in the samples reduced as WGP content increased. In environment whereby cooling is done by combine action of air and water, ≤15 wt. % WGP addition to bricks might suffice in clay materials, since from 0 to 15 wt. % difference in the number of cycles for Exp. 1, 2 and 3 was in the range of 2 to 5 cycles.

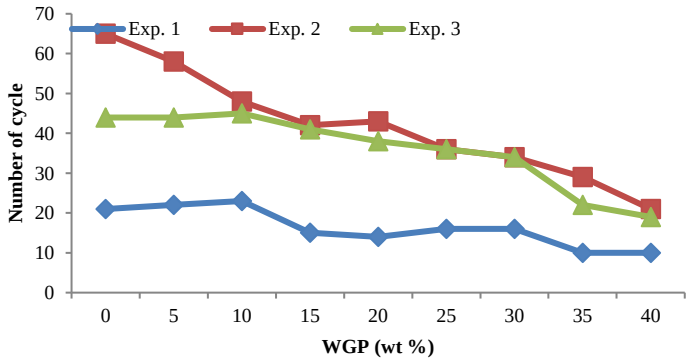

Fig. 13 Effect of WGP content on thermal fatigue

b. Cooling rate

i. Normalized cooling

It was observed that with increasing WGP content, cooling rate increased (Figure 14) with WGP addition, due to enhanced thermal conductivity. Highest cooling rate was recorded at 40 wt. % for each of the temperatures considered. Therefore, in applications whereby normal cooling rate is employed, increased WGP content in fired bricks is recommended.

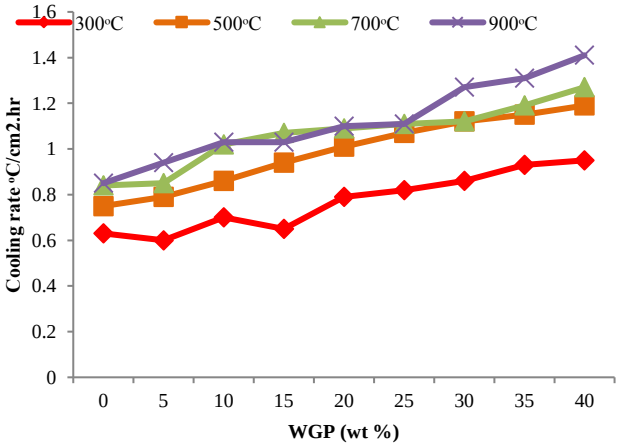

Fig. 14 Effect of WGP content on cooling rate

ii. Rapid cooling (Fast cooling rate per cross section)

Figure 15, shows the effects of WGP on cooling rate of samples at fast cooling rate using water. The incorporation of WGP into bricks at increasing weight content resulted into higher cooling rate due to high emissivity at elevated temperatures. At high temperature, particles are highly excited leading to mobility and increased interparticle spacing. The process of rapid cooling results into forceful dissipation of already absorbed energy in solid bodies, causing inherent particles to maintain disoriented positions at low temperature as the heat is been dissipated. This caused distortion in the arrangement and orientation of particles which resulted in increased brittleness in the samples. Furthermore, at high temperature of 900 °C where degradation of glassy phase was more pronounced, as cooling rate became high, the glassy phase were not allowed to re-form causing uneven distribution of glass particles within the clay matrix as shown in Figure 18. This initiates high level of brittleness because of high strain energy induced around the unevenly distributed glass particles, resulting in low strength as expressed in Figure 18.

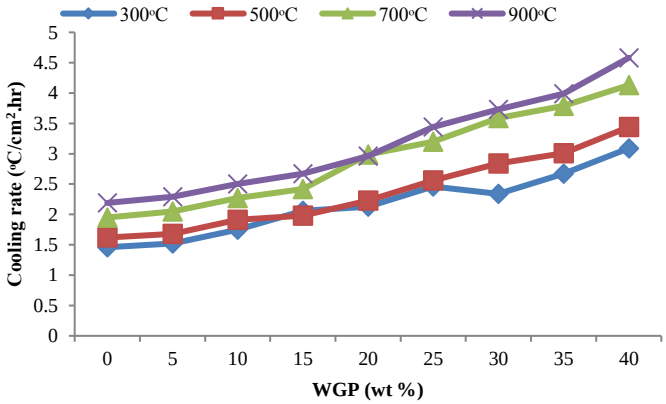

Fig. 15 Effect of WGP on High cooling rate per cross section of samples

iii. Cooling rate coefficient

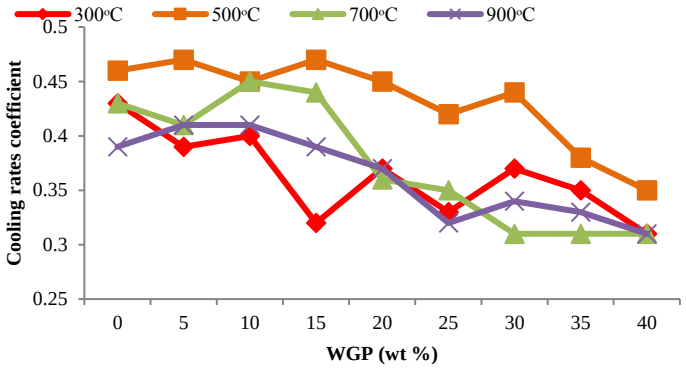

Fig. 16 Cooling rate coefficient with increasing WGP

Figure 16 shows the coefficient of cooling rate at different temperature with increasing WGP content. The cooling rate at 500 °C is the highest indication that normalized cooling rate for all samples is more effective than fast cooling at that temperature. Highest cooling rate coefficient for all samples was recorded at 500 °C for 15 wt. % WGP, indicating that for applications which may involve normalized cooling and fast cooling, temperature should not exceed 500 °C for all composition. Therefore, WGP composition of 15 wt. % gave the optimum value.

Morphological behaviour: effect of fast cooling on strength performance of clay sample

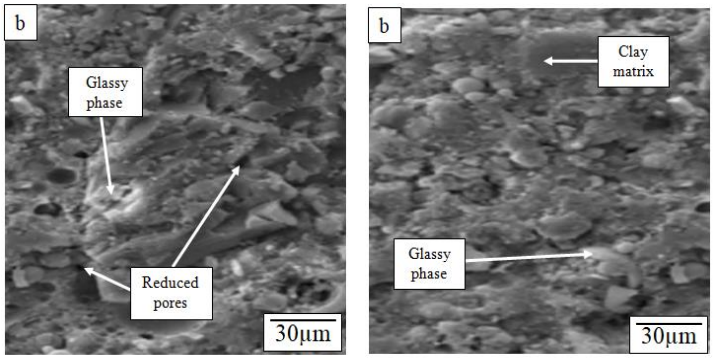

Fig. 17 Surface image of sample with 30 wt. % WGP (a) and 35 wt. % WGP (b), before rapid cooling.

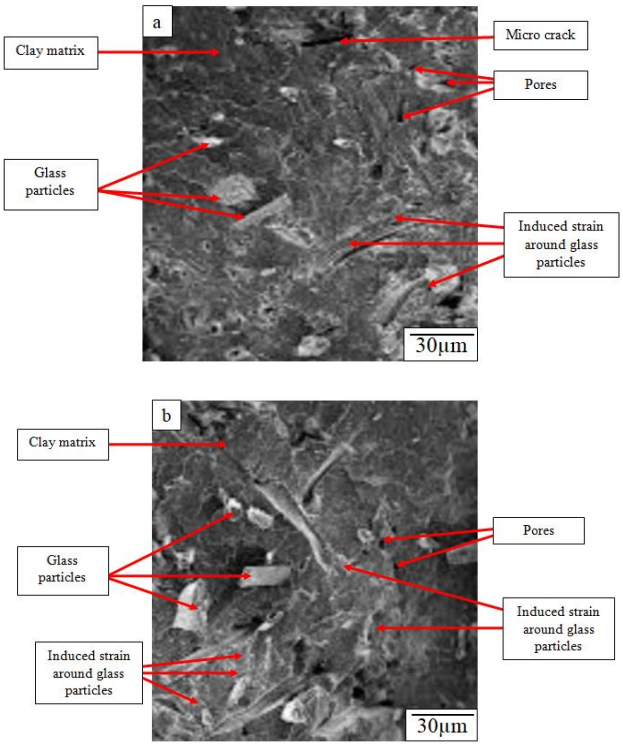

Fig. 18 Surface image of sample with 30 wt. % WGP (a) and 35 wt. % WGP (b), cooled rapidly from 900 °C to room temperature

Table 9 Impact resistance (number of cycle to failure) after fast cooling

% WGP content in samples	Number of cycle to failure at 26 °C	Impact resistance (number of cycle to failure) of samples after fast cooling			
		300 °C	500 °C	700 °C	900 °C
20	18	7	5	2	1
25	16	8	6	2	1
30	16	7	6	2	1
35	14	5	3	1	1
40	12	5	3	1	1

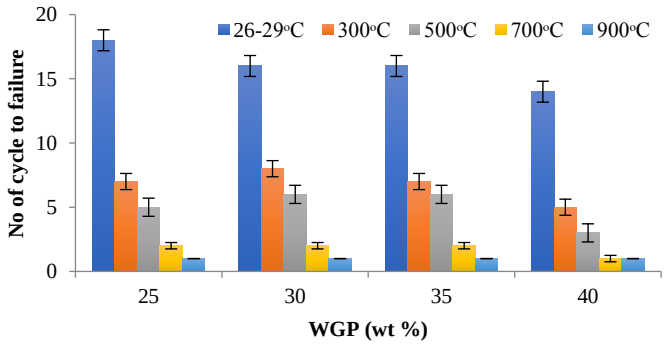

Fig. 19 Impact resistance (number of cycle to failure) of samples at room temperature (26-29 °C) and those fast cooled to room temperature from 300, 500, 700 and 900 °C

Impact resistance of samples after brick samples were fast cooled from high temperature reduced when compared to impact resistance of samples that were not fast cooled. For 20 wt. % WGP, the number reduced from 18 cycles to 7, 5, 2, 1 when fast cooled from 300, 500, 700 and 900 °C respectively, as indicated in Table 9, which indicates that fast cooling of brick samples from high temperature enhances brittleness or ease to fracture in samples. For 25 wt. % WGP, the number reduced from 16 cycles for sample tested at room temperature to 8, 6, 2 and 1 cycles for samples fast cooled from 300, 500, 700 and 900 °C respectively. In the case of 30, 35 and 40 wt. % WGP fast cooled, number of cycle to failure was 7, 6, 2, and 1 for 30 wt. % WGP, 5, 3, 1, 1 for 35 wt. % WGP and 5, 3, 1, 1 for 40 wt. % WGP (Table 9). From the results, it is clear that fast cooling reduces resistance to impact (Figure 19).

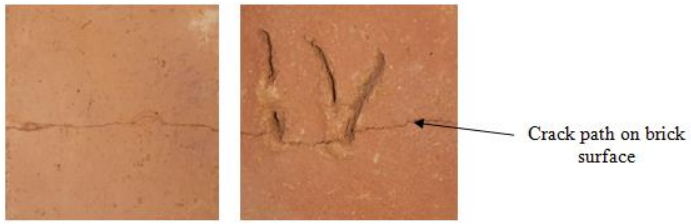

Fig. 20 Image showing crack path on surface of bricks during test

Comparing compressive strength of samples tested at room temperature and those tested after rapid cooling, it was observed that there was great reduction in strength. At fast cooling rate, particles are disarranged and disoriented leading to high strain energy stored in samples which aids ease to fracture in samples. The effect was more pronounced as temperature increased from 300 to 500 to 700 to 900 °C. Respective reduction in strength while comparing values at 26-29 °C to 300, 500, 700 and 900 °C was 45 %, 50 %, 80 % and 89 % for 25 wt. % WGP, 46 %, 50 %, 84 % and 88 % for 30 wt. % WGP, that of 35 wt. % WGP was 53 %, 60 %, 83 %, and 88 %. For 40 wt. % WGP, the reduction was 54 %, 64 %, 82 % and 90 % respectively (Figure 21).

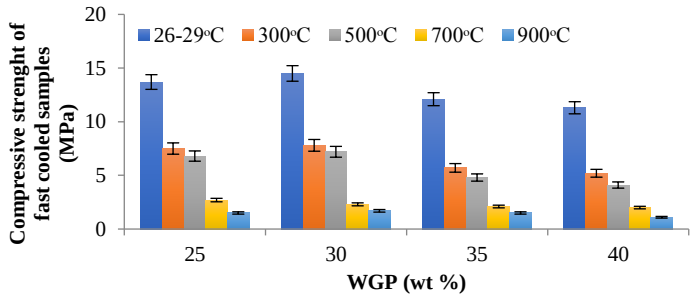

Fig. 21 Comparison of compressive strength of samples at room temperature (26-29 °C) and those fast cooled to room temperature from 300, 500, 700 and 900 °C

For flexural strength (figure 22), respective reduction in strength while evaluating from 26-29 °C to 300, 500, 700 and 900 °C was 52 %, 54 %, 93 % and 99 % for 25 wt. % WGP, 52 %, 53 %, 91 % and 98 % for 30 wt. % WGP, that of 35 wt. % WGP was 53 %, 50 %, 81 % and 99 % and for 40 wt. % WGP, the reduction was 51 %, 53 %, 94 % and 99 % respectively. Analyzing the percentage reduction for compressive strength, the effect was more pronounced at temperatures of 700 and 900 °C with reduction varying from 80 to 84 % for 700 °C and 88 to 90 for 900 ^{0} C. In the case of flexural strength, the reduction was also more pronounced at temperatures of 700 and 900 °C varying from 81 to 95 % for 700 °C and 98 to 99 for 900 °C for samples containing 25 to 40 wt. % of WGP. The effect had higher toll on flexural than compressive strength and at 900 °C, highest percentage reduction was recorded in flexural strength.

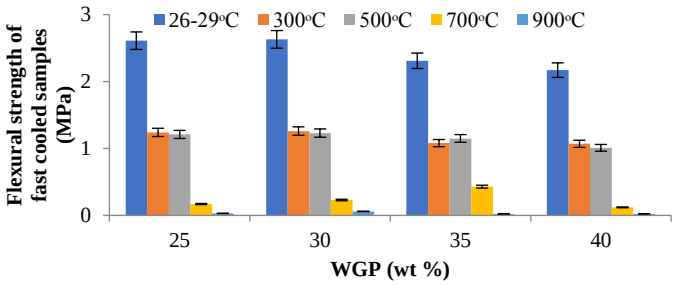

Fig. 22 Comparison of flexural strength of samples at room temperature (26-29 °C) and those fast cooled to room temperature from 300, 500, 700 and 900 °C

CONCLUSIONS

Effects of elevated temperature and waste glass powder (WGP) content on thermo-mechanical properties of fired ceramic products were examined in this study and response of samples to different temperatures were analyzed. From the results obtained, the following conclusion were made

- With increased temperature from 26-29 ºC to 700 ºC, mechanical performance tends to reduce gradually due to gradual weakening of bond and degradation of the glassy phase present in the samples
- At up to 900 ºC the performance reduced drastically due to high extent of bond weakening and fastened degradation of the glassy phase coupled with increased thermally induced residual stress and high excitation of particles/atoms, hereby, dictating an operating temperature of ≤ 700 ºC for samples.
- Thermal conductivity, diffusivity and emissivity increased with increasing WGP content while thermal expansivity and specific heat capacity reduced as percentage WGP increased in the samples
- For samples heated to 1000 ºC, thermal shock resistance improved from 0 to 10 wt. % WGP while at further addition of WGP, the resistance reduced, in this case refractory bricks, WGP should not exceed 10 wt. %.
- Thermal shock resistance remains stable in samples at WGP content of ≤15 wt. %, beyond this, there was reduction (for samples air/water cooled from 300 ºC). Therefore, for ceramic products to be exposed to operating temperature of $\leq 300^0$ C, WGP should be ≤ 15 wt. %.
- Higher thermal conductivity and lower specific heat capacity resulted into increased cooling rate at higher WGP addition, hence for fast cooling rate applications, increased proportion of WGP (between 5 to 40 wt. %) may be recommended, however for applications whereby compressive and flexural strength are important as well as increased cooling rate, WGP content of between 5 to 30 wt. % may be suitable, since the strength reduced at 35 and 40 wt. % at room temperature, as shown in Table 2 and 3.
- The coefficient of cooling rate at 500 ºC was the highest indication that normalized cooling rate for all samples is more efficient than fast cooling at that temperature
- Rapid cooling for heat treated bricks reduces strength largely, hence not recommended for fired clay bricks.

Acknowledgments: Authors are grateful for the support of the Metallurgical and Materials Engineering Department, Federal University of Technology Akure, Glass and Ceramic Laboratory, Federal Polytechnic, Ado-Ekiti and Landmark University Centre for Research, Innovation, and Development (LUCRID) through SDGs 9 Group Innovation, Industry and Infrastructure.

REFERENCES

1. R. Bermejo, R. Danzer: Mechanical Characterization of Ceramics: Designing with Brittle Materials, *Comprehensive Hard Materials*, 2, 2014, 285-298, https://doi.org/10.1016/B978-0-08-096527-7.00028-3
2. F.O. Aramide, O.D. Adepoju, A.A. Adediran, A.P.I. Popoola: Studies on the combined effects of titania and silicon carbide on the phase developments and properties of carbon-clay based ceramic composite. Cogent Engineering, 6, 2019, 1584938, https://doi.org/10.1080/23311916.2019.1584938
3. A. Shakir, A. Mohammed: Manufacturing of Bricks in the Past, in the Present and in the Future: A state of the Art Review, International Journal of advances in applied Science, 2(3), 2013, 145-156, https://doi.org/10.11591/ijaas.v2i3.1751
4. N. Tangboriboon, W. Pannangpetch, K. Aranyik, K. Petcharoen, A. Sirivat: Embedded Eggshells as a Bio-Filler in Natural Rubber for Thermal Insulation Composite Foams, Progress in Rubber Plastics Recycling Technology, 31, 2015, 189-206, https://doi.org/10.1177/147776061503100304.
5. E. Bwayo, K. Obwoya Sam: Coefficient of Thermal Diffusivity of Insulation Brick Developed from Sawdust and Clays. Journal of Ceramics, 2014, 1-6, https://doi.org/10.1155/2014/861726
6. S. Ahmad, Y. Iqbal, R. Muhammad: Effects of Coal and Wheat Husk Additives on the Physical, Thermal and Mechanical Properties of Clay Bricks, Boletin de la Sociedad Espanola de Ceramica y Vifrio, 56(3), 2017, 131-138, https://doi.org/10.1016/j.bsecv.2017.02.001
7. ASTM C 1314-18: Standard Test Methods for Compressive Strength of Masonry Prisms, *ASTM International*, West Conshohocken, PA, 2018.
8. ASTM 293/C293M: Standard Test Methods for Flexural Strength of Masonry bricks (Using Simple Beam with Centre-Point Loading), *ASTM International*, West Conshohocken, PA, 2016
9. ASTM E1225-13: Standard Test Method for Thermal Conductivity of Solids Using Guarded-Comparative–Longitudinal Heat Flow Technique. *ASTM International*, West Conshohocken, PA, 2013
10. ISO 17139:2014(en): Thermophysical Properties of Ceramic Composites-Determination of Thermal Expansion. International Standard Organization, 2014.
11. ASTM E1269-11: Standard Test Method for Determining Specific Heat Capacity by Differential Scanning Calorimetry. *ASTM International*, West Conshohocken, PA, 2018
12. ASTM C1470-20: Standard Guide for Testing the Thermal Properties of Advanced Ceramics. *ASTM International*, West Conshohocken, PA, 2020.
13. ASTM E2585-09: Standard Practice for Thermal Diffusivity by the Flash Method. *ASTM International*, West Conshohocken, PA, 2009
14. ASTM C1525-18: Standard Test Method for Determination of Thermal Shock Resistance for Advanced Ceramics by Water Quenching. *ASTM International*, West Conshohocken, PA, 2018
15. J. Y. Hwang, X. Huang, A. Garkida: Waste Colored Glasses as Sintering aid in Ceramic Tile Production. Journal of Minerals and Materials Characterization and Engineering, 5(2), 2006, 119-129, https://doi.org/10.4236/jmmce.2006.52008
16. M. Abuh, C. A. Agulanna, P. E. Chimezie, J. U. Bethel–Wali: Implications and Characteristics of Waste Glass Cullet-Kaolinite Clay Ceramic. Journal of Applied Science and Environmental Science, 23, 2019, 513-518, https://doi.org/10.4314/jasem.v23i3.22
17. P. Praveen, E. Chandrasekaran, G. Viruthagiri: The effect of temperature on ceramic bricks with replacing waste glass in low volume ratio. International Journal of Advanced Science and Research, 3(2), 2018, 79-86
18. Chao-Wei Tang: Properties of Fired Bricks by Incorporation TFT-LCD Waste Glass Powder with Reservoir Sediments. Sustainability, 10 (7), 2018, 2503. https://doi.org/10.20944/preprints201806.0229.v1
19. H. H. Abdeen, S. M. Shihada: Properties of fired clay bricks mixed with waste glass. Journal of Scientific Research and Reports, 13(4), 2017, 1-9. https://doi.org/10.9734/jsrr/2017/32174
20. I. Demir: Reuse of waste glass in building brick production. International Journal of Waste Management and Research, 27, 2009, 572-577. https://doi.org/10.1177/0734242x08096528
21. V. Ducman, T. Kopar: Sawdust and paper-making sludge as pore-forming agents for lightweight clay bricks. Journal of Industrial Ceramics, 21, 2001, 81-86
22. M. E. Borredon, E. Vedrenne, G. Vilarem: Development of Eco-Friendly Porous Fired Clay Bricks using Pore Forming Agents: A Review. Journal of Environmental Management, 143, 2014, 186-196. https://doi.org/10.1016/j.jenvman.2014.05.006
23. A. Salazar: On Thermal Diffusivity. European Journal of Physics, 24, 2003, 351-358, https://doi.org/10. 1088/0143-0807/24/4/353
24. Y. Zhang, Q. Li, H. Zhou: Theory and Calculation of Heat Transfer in Furnaces, *Emission and Absorption of Thermal Radiation*, 2016, 45-75,

https://www.researchgate.net/publication/304108475_Emission_and_Absorption_of_Thermal_Radiation
25. K. Radmanovic, I. Dukicand, S. Pervan: Specific Heat Capacity of Wood. Drvna Industrija, 65, 2014, 151-157, https://doi.org/10.5552/drind.2014.1333
26. Y. Shuaib-Babata, S. Yaru, S. Abdulkareem, Y. Busari, I. Ambali, S. Kabiru, Ajao, G. Mohammed: Characterization of Baruten Local Govertment Area of Kwara State (Nigeria) Fireclays as Suitable Refractory Materials. Nigerian Journal of Technology, 37, 2018, 374-386, https://doi.org/10.4314/njt.v37i2.12

OPEN ACCESS

ACTA METALLURGICA SLOVACA

2020, VOL. 26, NO. 3, 95-99

RESEARCH PAPER

EFFECT OF COLD DEFORMATION AND ANNEALING PHENOMENA ON THE MICROSTRUCTURAL CHANGES AND MICRO-HARDNESS IN Al-Mg-Si ALUMINIUM ALLOYS

Abdelouahab Noua[1,2] , Meryem Guemini[1,2], Toufik Ziar[2,3*], Hichem Farh[2,3], Rebai Guemini[1,2]

[1] Department of Material Sciences, Faculty of Exact Sciences, Larbi Ben M'hidi University of Oum El Bouaghi, Algeria.

[2] Active devices and material laboratory (LCAM), Larbi Ben M'hidi University of Oum El Bouaghi, Algeria.

[3] Department of Material Sciences, Faculty of Exact Sciences, Larbi Tebessi University of Tebessa, Algeria.

*Corresponding author: toufik1_ziar@yahoo.fr; Tel.: +213662584466; Fax: +213 03242354. Department of Material Sciences, Faculty of Exact Sciences, Larbi Tebessi University of Tebessa ,12000, Algeria.

Received: 27.06.2020
Accepted: 29.06.2020

ABSTRACT

Aluminium alloys are of particular interest because of their low density, low cost and ease of thermo-mechanical processing. During the recent years, much interest has been shown in the development of alloys with optimal mechanical properties which can be retained at high temperatures. The purpose of the present investigation is to study the microstructure of two Al-Mg-Si alloys containing transition elements after cold deformation 10%, 20 %, 30%, 40% and 50% reduction in thickness and annealing at 1 hour at different temperature by using the optical microscopy, transmission electron microscopic (TEM), Vickers hardness measurement. We notice that the micro-hardness increases with the increasing of the deformation level. The coarse particles, with a particle size of about 2 to 3 µm, give rise to a heavily local deformation of the Aluminium matrix. The formation of well-defined substructure due to the arrangement of dislocations is observed after an increase in annealing temperature.

Keywords: Al-Mg-Si alloys; Dispersoid particles; Cold deformation, Recrystallization; Precipitation

INTRODUCTION

Al-Mg-Si alloys **(EN AW 6xxx** alloys**)** are structural hardening Aluminium alloys. They have notable overall properties with a good aptitude to hot deformation by rolling and cold drawing [1, 2]. The excellent mechanical and electrical properties of these alloys enabled their use in various sectors such as aerospace, automotive and transport of electricity [3-5]. The transition elements such as zirconium, chromium and manganese, which have low solubility and very slow diffusion rates in the α-Aluminium solid solution, are generally added to EN AW 6xxx alloys to produces fine dispersoid particles. These fine particles dispersion retard the crystallization and increase the microstructure stability at high temperature due to their low solid solubility and diffusivity in Aluminium [6, 7]. It has been shown that the addition of transition elements to EN AW 6xxx alloys inhibit recrystallization when the alloys are pre-heated before deformation [8-10]. In EN AW 6xxx alloys, the nucleation of the dispersoid particles such as Zr-containing dispersoids, Mn-containing dispersoids, and Cr-containing dispersoids, which play the role of recrystallization inhibition, has been studied [11-15]. The needle-shaped Mn-containing dispersoids formed by using the rapid heating are much more effective than the fine spherical dispersoids formed by using the slow heating for grain refinement during the recrystallization process [16].

The grain growth and recrystallization will change the mechanical and chemical proprieties of the alloys. The information of the deformed state and annealing phenomena was detailed by Humphreys and Hatherly [17]. There is a succession of interesting processes for recrystallization dealing with the rearrangement of defects in the deformed crystals and conclude with the replacement of the deformed grain by a new set of strain-free crystals. The change in the recrystallization behaviour due to the presence of the second phase particles have been studied Sooner [18-20].

The cold rolling is a process that transforms the metal between two smooth or fluted rolls, rotating in the opposite direction. Due to this rotational movement and of the compression generated by the cylinders, there is a continuous reduction in the initial thickness by plastic deformation of the metal [1]. They are normally provided in planar shape whose width is dictated by that of the starting plate which they are cast, the length itself being limited by the constraints of transport. In recent years, the influence of cold rolling on the precipitation processes in EN AW 6xxx alloys is widely studied [21-23.]. It shows that the precipitation and growth of the second phase are accelerated significantly by this process. The larger grains have a preferred orientation (texture) when the alloy is more deformed [24, 25]. A study by Zhang [25] showed the effect of deformation and annealing on electrical conductivity, mechanical properties and texture of Al-Mg-Si alloy cables.

EXPERIMENTAL PROCEDURE

Materials

The Al-Mg-Si alloys were provided by Alcan International Limited of Canada. They were prepared by a direct chill casting process (DC) in a 178 mm of moulds. Then they were given a 10%, 20 %, 30%, 40% and 50% reduction in thickness by cold rolling in the air. The as-rolled alloys with the reduction in thickness of 50% (reduction in thickness) followed by an annealing for 1 h at different temperatures were chosen to study the effect of cold deformation on the microstructural changes and mechanical properties of as-rolled alloys. The chemical composition of the investigated alloys is given in Table 1. Alloy 1 contained at about 0.13wt. % Zr, while the alloy 2 was Zr-free and contained 0.65wt. % Mn. The as-cast specimens were heat-treated for 10 hours (h) at 550°C, cold-deformed by 10%, 20 %, 30%, 40% and 50% reduction in thickness and then annealed for 1 h at 350°C and 450°C and after that water quenched in order to follow the nucleation and growth of the dispersoids particles.

Table 1 Chemical composition of the two alloys

Alloys	Si	Fe	Cu	Mn	Mg	Cr	Zr	Al
Alloy 1	0.62	0.21	0.42	0.006	1.01	0.002	0.13	bal
Alloy 2	1.30	0.23	0.004	0.65	0.79	0.001	-	bal

Metalographic preparation

Specimens for optical microscopy examination of each heat examination each heat treatment were mounted, ground on successive papers 180, 250, 350, 450, 600 and 800 and polished with 1-micron diameter diamond paste. They were finally polished on cloth with an alumina oxide particles suspension (OPS). The polished specimens were etched in Keller's reagent (1.5% HF - 2.5% HNO3 - 95% water) for about 15 s.

Thin foils for TEM were prepared by spark machining to form discs 3 mm in diameter. The discs were subsequently grounded with fine silicon-carbide emery paper to about 200 mm thick. Final thinning was by jet polishing using a Struers Tenupol Unit with a solution of 33% HNO3 in Analar grade methanol at -10 to -15 volts and a temperature of -20 to -30°C. When the electropolishing was completed the specimens were removed from the solution as quickly as possible and washed with Analar methanol. The specimens were dried between filter papers and then stored in a specimen grid box under vacuum.

Optical microscopy

Optical examination was carried out with an Olympus BH-2 microscope which contained a differential interference contrast (DIC) facility and polarised light.

TEM microscopy

Electron microscopy examination was carried out with an EM 300 electron microscope at 100 KeV. A liquid nitrogen-cooled decontaminator, an eccentric goniometer and double tilt holder were used to prevent the contamination after extended observation of an area of the thin foil.

Hardness measurements

Hardness measurements were performed using Vickers hardness tester. The test samples used for hardness measurements were 1×1 cm in size. Hardness data were determined with a load of 10 Kg (~ 98.06 N). Each measure of Vicker's hardness represents the mean value of at least 10 indentations

RESULTS AND DISCUSSION

Figure 1 shows the variation in microhardness as a function of different deformation level (0%, 10%, 20%, 30%, 40% and 50%) by cold rolling for the two alloys. An increase in microhardness is observed with the increase of the deformation level [5, 24, 26]. This increase in hardness is probably due to the high density of dislocations introduced by deformation of the two alloys by cold rolling, which leads to hardening of the alloys. This result confirms the results obtained by some researchers [5, 26].

The variation of the microhardness (HV) as a function of different deformation levels (0%, 10%, 20%, 30%, 40% and 50%) and then annealed for 1 h at 350°C and 450°C, and then water quenched of the two alloys is shown in Figure 2 and Figure 3.

The decrease in hardness is observed with the increasing of the annealing temperature in both alloys. This reduction in microhardness is attributed to the phenomenon of softening of the alloy pushed by the annealing treatment, which makes the increase in the ductility of the cold-rolled Al-Mg-Si alloy.

Figure 4 and Figure 5 show the optical micrographs of the two alloys in the cold deformed state and the microstructural change during the annealing of the cold-rolled solution treated alloys. Specimens of the two alloys are taken in the long-transverse direction.

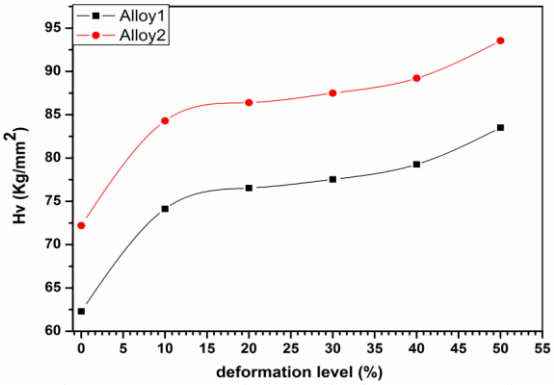

Fig. 1 Variation of microhardness as a function of deformation level of the two alloys

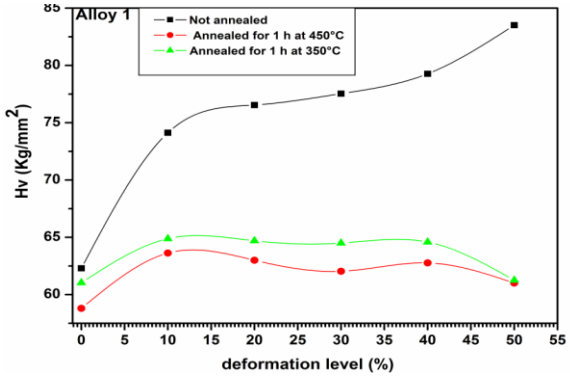

Fig. 2 Variation of the microhardness (HV) as a function of the deferent deformation level and then annealed for 1 h at 350°C and 450°C of alloy 1

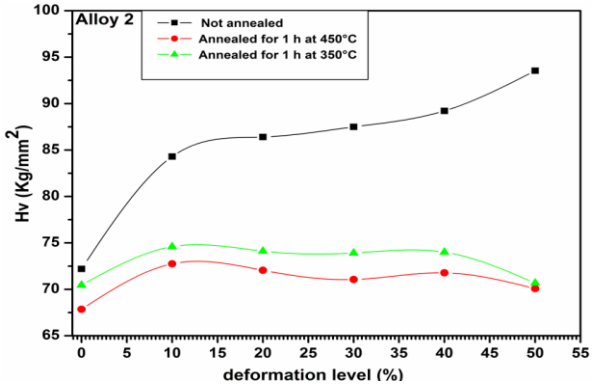

Fig. 3 Variation of the microhardness (HV) as a function of the deferent deformation level and then annealed for 1 h at 350°C and 450°C of the alloy 2

The large grains can be seen to be strongly elongated in the rolling direction in the deformed state and after annealing up to 350°C. In a few areas, insoluble coarse particles originating from the cast structure appear to align themselves along the rolling direction. Alloy 1 shows only sub-structure inside the grains and less precipitate free zones along grain boundaries. Coarse particles were also observed elongated along the rolling direction. Some of them appear to be broken during the rolling. Optical micrographs revealed the sub-grain structure in the two alloys but more accentuate in the alloy 1. The main significant change in the microstructure was observed after annealing in the temperature 350°C.

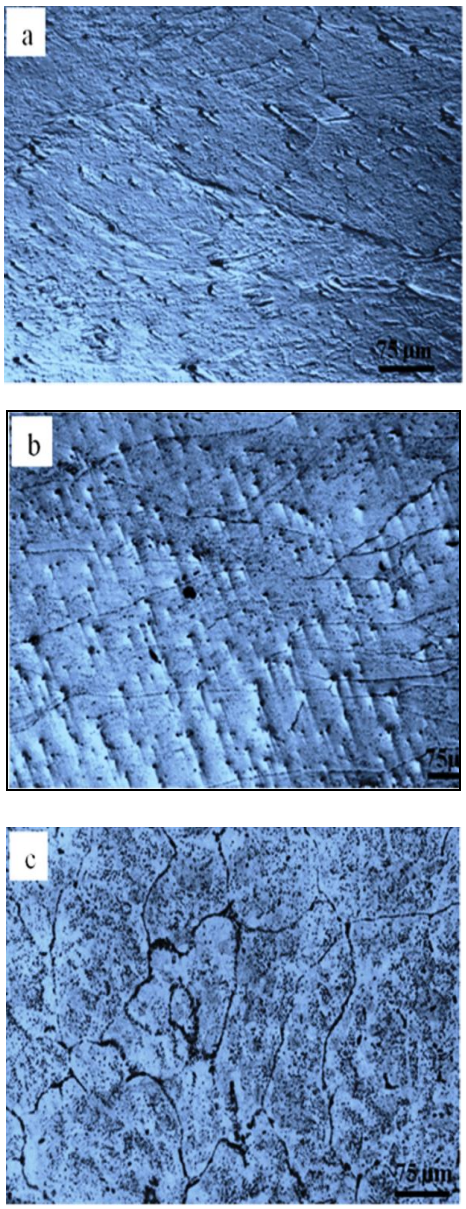

Fig. 4 Optical micrographs of alloy 1 showing the microstructure change after rolling at room temperature to 50% reduction and annealing for 1 hour at: (a) as-rolled, (b) 350°C and (c) 450°C

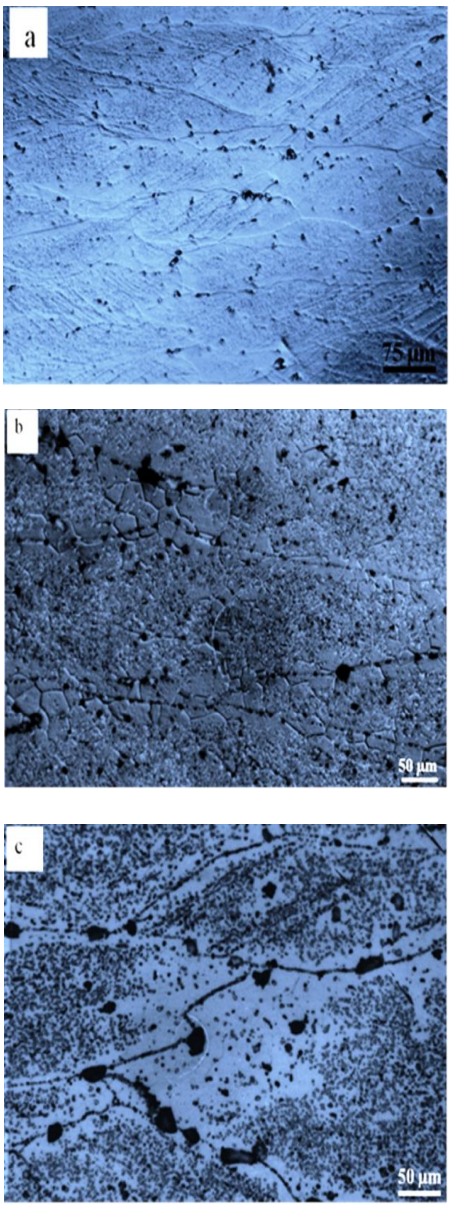

Fig. 5 Optical micrographs of alloy 2 showing the microstructure change after rolling at room temperature to 50% reduction and annealing for 1 hour at: (a) as-rolled, (b) 350°C and (c) 450°C

Transmission electron micrographs in the longitudinal direction of the two alloys heat-treated for 10 h at 550°C and then cold deformed by 50% reduction in thickness and then annealed for 1 h at different temperatures are shown in Figure 6 and Figure 7.

After deformation, the microstructure of the two alloys are characterised by dislocation networks and well-defined cell structure, Figure 6a and Figure 7a. The co-existence of dispersoid particles and un-dissolved coarse particles is observed in the two alloys.

Coarse particles which mainly remain along grain boundaries are elongated along the rolling direction. Some of them look to be broken. Large particles generate a heterogeneous distribution of dislocations during deformation associated with a local high dislocation density at particle-matrix interfaces which could act as recrystallization nuclei during annealing. Electron microscopic observations show also that in all cases the coarse second phase particles were associated with a high dislocation density.

The dispersoid particles distribution is fairly homogeneous except in the regions around the coarse particles where the precipitate free zones (or PFZ's) were observed. Some coarse particles, with a particle size of about 2 to 3 µm, give rise to a heavily local deformation of the Aluminium matrix. In the initial state cell interiors were filled with dislocations as well as sub-grain walls. Cleaning of cell interior and sharpening of cell boundaries were observed after an increase in ageing temperature. Hence sub-grain growth occurred; this result is in good agreement with the literature results [9, 10].

On annealing, well-defined sub-grains were formed (Figure 6b and Figure 7b) and at lower temperatures of annealing these were seen to grow by the migration of low angle boundaries at a rate controlled by the coarsening of the particles [18]. Most of the grain boundaries are not mainly straight but lie in contact with coarse particles. The irregular dislocation structure are replaced by a more regular fine-scale structure in which some cells begins to expand and serve as recrystallization nuclei. A good example of this phenomenon in aluminium has been found after very large rolling reductions (>95%), a stable fine-grained microstructure was formed on annealing, whereas at lower strains, normal discontinuous recrystallization occurred [18].

Fully recrystallized microstructure, Figure 6c and Figure 7c were achieved after annealing at 350°C for alloy 2 and 450°C for alloy 1.

Transmission electron micrographs revealed the precipitation of free silicon particles occurring during the recovery and recrystallization process. A mixed particle structure consisting of large coarse particles, resulting from the casting, and free silicon particles and dispersoid particles formed before deformation were also observed.

The dispersoid particles were not observed to be deformed after the cold deformation. PFZ's along the elongated grain and around the coarse particles were also observed. During the move of the sub-grain boundary, reacting with other dislocations will annihilate some dislocations, but the majority of them will enter the boundary. Hence the density of dislocations will increase.

The remaining coarse particles with a diameter greater than 2 µm give rise to local deformation of the Aluminium matrix in their vicinity. This effect was more pronounced with a particle with a higher particle size.

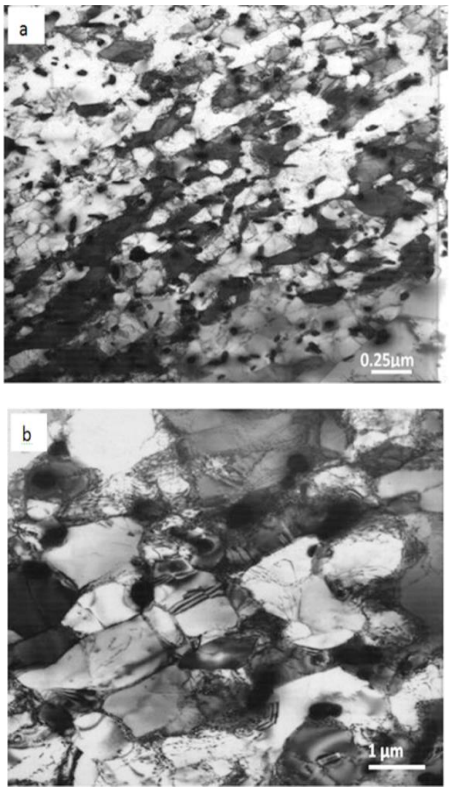

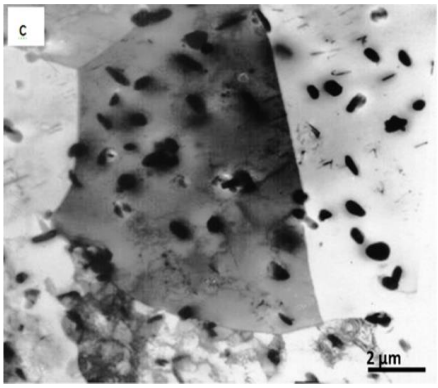

Fig. 6 TEM of alloy 1 showing the microstructure change after rolling at room temperature to 50% reduction and annealing for 1 hour at :(a) as-rolled, (b) 350°C and (c) 450°C

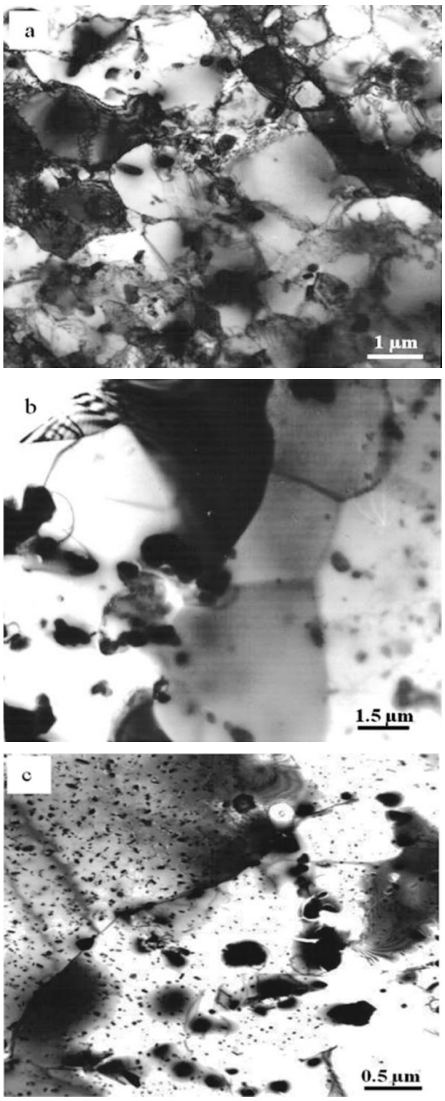

Fig. 7 TEM of alloy 2 showing the microstructure change after rolling at room temperature to 50% reduction and annealing for 1 hour at (a) as-rolled, (b) 350°C and (c) 450°C

CONCLUSIONS

Deformation by rolling Al-Mg-Si alloys causes an increase in microhardness and the annealing treatment decreases this microhardness, this increase in the microhardness due to the high density of dislocations introduced by deformation by cold rolling which accelerate the precipitation of the hardening phases.
The structural change which occurs during the annealing is mainly due to the generation of sub-grains, from the elongated cell-structure, which was observed in the deformed matrix. Annealing at 350°C has little effect on the dislocation network. After a further increase in ageing temperature, the sub-grains grow by consuming the surrounding cell-structure; the dispersoid particles coarsen and become less effective in retarding recrystallization.
The formation of a well-defined substructure due to the arrangement of dislocations is observed after the annealing temperature was increased. Large particles generate a heterogeneous distribution of dislocations during deformation associated with a local high dislocation density at particle-matrix interfaces, which could act as recrystallization nuclei during annealing.

Acknowledgements: Authors are grateful for the support of experimental works by research project (PRFU) under code number: B00L02UN120120190002 approved, on 01/01/2019, by the Ministry of Higher Education and Scientific Research in Algeria.

REFERENCES

1. H. Farh, T. Ziar, H. Belghit, M. Khechba, A. Noua, F. Serradj: Defect and Diffusion Forum, 397, 2019, 51. http://dx.doi.org/ 10.4028/www.scientific.net/ddf.397.51
2. Y. Totik, R. Sadeler, I. Kaymaz, M. Gavgali: J. Mater. Process. Technol, 147, 2004, 60. http://dx.doi.org/10.1016/j.jmatprotec.2003.10.026
3. T. Kvackaj, J. Bidulska, M. Fujda, R. Kocisko, I. Pokorny, O. Milkovic: Mater. Sci. Forum, 633-634, 2010, 273-302 https://doi.org/10.4028/www.scientific.net/MSF.633-634.273
4. H. Belghit, H. Farh, T. Ziar, M. Zidani, M. Guemini: Arch. Metall. Mater, 63(4), 2018, 1643. https://doi.org/10.24425/amm.2018.125088
5. M. Zidani, L. Bessais, H. Farh, M.D. Hadid, S. Messaoudi, D. Miroud, M.K. Loudjani, A.L. Helbert, T. Baudin: Steel Compos Struct, 22 (4), 2016, 745. http://dx.doi.org/10.12989/scs.2016.22.4.745
6. Y. Wuhua, L. Zhenyu, Z.W. Chuanyang: Mater & Design, 34, 2012, 78. https://dx.doi.org/10.1016/j.matdes.2011.07.003
7. Belov: Mater. Sci. Forum, 217-222, 1996, 293. http://dx.doi.org/10.4028/www.scientific.net/msf.217-222.293
8. T. Ziar, H. Farh, R. Guemini: Acta Metall Slovaca, 22(3), 2016, 138. http://dx.doi.org/10.12776/ams.v22i3.697
9. R. Guemini, A. Boubertakh, G.W. Lorimer: J Alloy Compd, 486 (1–2), 2009, 451. http://dx.doi.org/10.1016/j.jallcom.2009.06.207
10. H. Farh, R. Guemini : Appl. Phys. A-Mater, 119, 2015, 285. http://dx.doi.org/10.1007/s00339-014-8963-5
11. P.J. Apps, M. Berta, P.B. Prangnell: Acta Mater, 53 (2), 2005, 499. http://dx.doi.org/10.1016/j.actamat.2004.09.042
12. L. Lodgaard, N. Ryum: Mater. Sci. Eng A, 283, 2000, 144. http://dx.doi.org/10.1016/s0921-5093(00)00734-6
13. M .Cabibbo, E. Evangelista, C. Scalabroni, E. Bonetti: Mater. Sci. Forum, 503-504, 2006, 841. http://dx.doi.org/10.4028/www.scientific.net/msf.503-504.841
14. H. Farh, K. Djemmal, R. Guemini, F. Serradj: Ann Chim-Sci Mat, 35(5), 2011, 283. http://dx.doi.org/10.3166/acsm.35.283-289
15. D.H. Lee, J.H. Park S.W. Nam: Mat. Sci. Technol, 15(4), 1999, 450. http://dx.doi.org/10.1179/026708399101505923
16. Y. Xu, H. Nagaumi, Y. Han, G. Zhang, T. Zhai: Metall. Mater Trans A, 48(3), 2017 ,1355. http://dx.doi.org/10.1007/s11661-016-3881-0
17. R. Hu, T. Ogura, H. Tezuka, T. Sato, Q. Liu: J. Mater. Sci. Technol, 26(3), 2010, 237. http://dx.doi.org/10.1016/s1005-0302(10)60040-0
18. F. Humphreys, M. Hatherly: Recrystallization and related annealing phenomena. Elsevier, Oxford, 2004. http://dx.doi.org/10.1016/b978-008044164-1/50016-5
19. T, Ozawa: Bull. Chem. Soc. Japan, 38 (11), 1965, 1881. http://dx.doi.org/10.1246/bcsj.38.1881
20. E.J. Mittemeijer: Recrystallization and Grain Growth. In: Fundamentals of Materials Science. Springer, Berlin, 2010. http://dx.di.org/10.1007/978-3-642-10500-5_10
21. V. Kumar, I.V. Singh, B. K Mishra: Acta Metall Sin, 27(2), 2014, 359. http://dx.doi.org/10.1007/s40195-014-0057-z
22. H. L. Yu, A. K. Tieu, C. Lu, X.H. Liu, C. Kong: Mater Sci Eng A, 568, 2013, 212. http://dx.doi.org/10.1016/j.msea.2013.01.048
23. B. Mirzakhani, Y. Payandeh : Mater Des, 68, 2015, 127. http://dx.doi.org/10.1016/j.matdes.2014.12.011
24. H. Farh, R. Guemini, F. Serradj, K. Djemmal: Turk. J. Phys, 34(2), 2010, 117. Doi:10.3906/fiz-1004-27
25. J. Zhang, M. Ma, F. Shen, D. Yi, B. Wang: Mater. Sci Eng A, 710, 2018, 27. https://doi.org/10.1016/j.msea.2017.10.065
26. B. Wang, X. H Chen, F.S. Pan, J.J. Mao,Y. Fang: Trans. Nonferrous Met. Soc. China, 25, 2015, 2481. https://doi.org/10.1016/S1003-6326(15)63866-3

OPEN ACCESS

ACTA METALLURGICA SLOVACA

2020, VOL. 26, NO. 3, 100-103

RESEARCH PAPER

FACILE DECORATION OF SILVER NANOWIRES MICROSTRUCTURE WITH CARBON NITRIDE NANOPARTICLES AS A MEMBRANE FOR WATER TREATMENT

Thuyet Minh Nguyen[1*], Hung Thai Le[1], Khanh Quoc Dang[1]

[1] School of Materials Science and Engineering, Hanoi University of Science and Technology, Hanoi, Vietnam

*Corresponding author: thuyet.nguyenminh@hust.edu.vn, tel.:+84 24 3868 0409, School of Materials Science and Engineering, Hanoi University of Science and Technology, No.1 Dai Co Viet, Hai Ba Trung, Hanoi, Vietnam

Received: 09.06.2020
Accepted: 27.07.2020

ABSTRACT

Silver nanowires (AgNWs) decorated by carbon nitride nanoparticles (CNPs) have been successfully synthesized using glucose as a carbon source, melamine as a nitrogen source and $AgNO_3$ as a silver source via the hydrothermal process and applying in the preparation of fouling membranes. Together, the freshly synthesized AgNWs and CNPs produced through redox reaction of glucose and melamine, processes the in-situ assembly of the coaxial 1D nanostructure of Ag covered by CNPs. The obtained CNPs with the uniform size of around 20 nm were aggregated on the surface of AgNWs which has average diameter of 50 nm. The fabricated AgNWs/CNPs membrane performances an enhanced photocatalytic activity under visible-range irradiation and shows excellent dye degradation catalyst.

Keywords: Silver nanowire, carbon nitride nanoparticle, membrane, hydrothermal method, photocatalytic

INTRODUCTION

Recently, membrane filtration technology has been widely applied due to its reliability and facile operation [1]. Up to different pollutants, the membrane fouling can be categorized into organic fouling, inorganic fouling, and biofouling [2]. Whatever kind of fouling happens, it will lead to a critical decrease in filtration activity, thus increasing maintenance price and shortened life-time of the membrane. Therefore, huge efforts have been invested to comprehend this problem as an urgent need.

Up to now, various nanomaterials have been demonstrated and decorated into membrane matrixes to form nanocomposite membranes in order to achieve specific desired properties. Among them, Silver nanowire (AgNWs) have attracted a lot of attention in modifying membrane materials due to their superior antibacterial characteristics. The AgNWs based nanocomposites membranes show crucial antibacterial and anti-biofouling behavior, which is assigned to the release of ion Ag+ [3].

Graphitic carbon nitride (CNPs) having the similar 2D layered structure of graphene possesses excellent visible photocatalysis as well as low cost and simple synthetic process that makes it the most attractive materials in the field of photocatalytically environmental purification [4-7]. However, the CNPs still has a limit due to the recombination of photo-induced charge carriers. Therefore, many approaches have been developed to improve electron-hole separation in pure CNPs [8-11]. Compared to other strategies, noble metal decoration has been regarded as a facile method for remedying the issue. According to several reports, CNPs combined with silver nanostructures can effectively improve charge separation performance, thus leading to boost the photocatalytic activity of the composite.To the best of our knowledge, the synthesis of AgNWs decorated by CNPs nanoparticles and its photocatalytic effect has not been reported yet.

Herein, the AgNWs/g-CNPs nanocomposite was synthesized via the simple mixing process from two fresh nanomaterials AgNWs and CNPs which were fabricated through the hydrothermal method. The as-synthesized composites were characterized by different analyses, then it could be used to introduce to the membrane for real applications.

MATERIAL AND METHODS

Materials and processing

In this study, Silver nitrate (AgNO3**)** was used as the precursor in the preparation of AgNWs. Firstly, the oven was turned on within 15 minutes to heat the glass bottle contained 20ml ethylene glycol (EG). During heating time, 17mg NaCl was supplemented and waited until the temperature reached to 100ºC then 20 mg $AgNO_3$ was added to the solution. Continuously, the temperature was increased slowly in 10 minutes to reach 135 – 140ºC, and 300 mg PVP was poured into. In next 8 minutes, the temperature was heated up to 155-160ºC and finally 250 mg $AgNO_3$ was added to the solution. This amount of $AgNO_3$ played the role of providing the Ag atoms toward the formation of Ag nanowires. To complete the reaction, the solution was heated at 160ºC for 6 hours and then cooled to the room temperature. In addition, centrifugal technique was used to dislodge the liquid and remove EG and excess PVP. Finally, the AgNWs was stored in ethanol to from the Ag nanowire suspension.

To synthesis of CNPs, 400 mg Melamine was dissolved in 80 ml DI water. This solution was ultrasonic vibrated for 1 hour then transferred into a 100ml Teflo-line stainless steel autoclave and reacted under the solvothermal condition at 180ºC in 24 hours. Finally, the yellow product which is known as CNPs was collected after 5 times of centrifugal operation at 10000 rpm in 15 minutes. The obtained CNPs then was dried overnight in the oven under vacuum at 60ºC.

The CNPs/AgNWs cellulose ester membranes was fabricated by a process as follows. Firstly, CNPs/AgNWs was prepared by adding 20 mg CNPs into 30 ml AgNWs 0.1 mg/mL, stirring in 2 hours, filtrating by 200nm filter paper then washing and drying in vacuum for 6 hours. Secondly, 100 mg dried CNPs/AgNWs powder were added into DMF and well dispersed by ultrasonic. Then the cellulose ester was dissolved, heated up and kept at 60ºC until the dissolution was completely. Finally, the solution was degassed at 60ºC and then scattered on class petri-dish. The nascent membrane was dipped in pure water at room temperature to induce phase inversion.

Characterization

Morphological structures of samples were characterized by Scanning electron microscopy (SEM) and transmission electron microscopy (TEM). The crystal structure was examined by X-ray diffraction (XRD)at a scanning rate of 10 min^{-1} in the range of 10–80. To investigate the optical properties the UV-Vis absorption spectra were collected at room temperature. Methylene Blue photodegradation of the synthesized samples under visible light was investigated as well.

RESULTS AND DISCUSSION

Figure 1 shows the synthesized Ag nanowire suspension, the XRD pattern and SEM images of dried AgNWs confirmed that the AgNWs have been synthesized successfully. Thus, from the XRD parttern (Fig. 1b), there are two obvious peaks with the positions in coherence with a standard spectrum of silver metal (JCPDS file No. 04-0783) at $2\theta \sim 38^0$ and $2\theta \sim 44^0$. These peaks correspond to the 111 and

200 reflections, respectively, of the silver cubic lattice indicating that the AgNWs were obtained in a crystalline form [12-14]. The morphology of the synthesized nanowires was observed by the scanning electron microscope, the results are presented in Figs 1c and d. These SEM images indicate that the prepared AgNWs sample consisted of uniform wires of solid form with smooth surface and have an average diameter and an average length of 50 nm and 30 µm, respectively that could be estimated from the insert images in Fig 1.

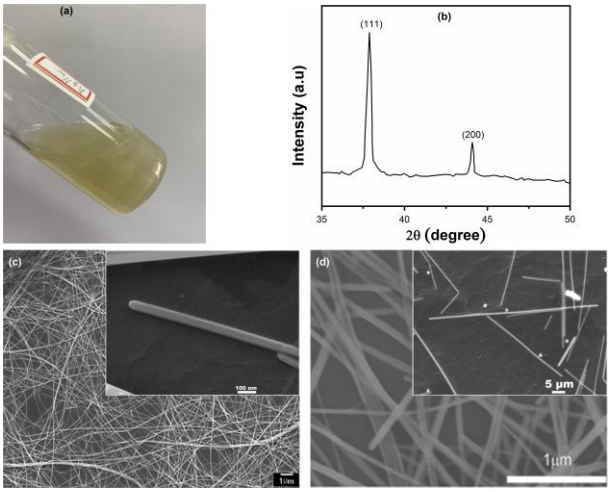

Fig. 1 (a) Ag nanowire in ethanol solvent. (b) XRD pattern of Ag nanowire. (c), (d), SEM images of Ag nanowires

In this work, melamine was used as the initial material for the synthesis of CNPs via the hydrothermal process which was mentioned in the early part of this paper. The prepared powder has yellow color as being seen in Fig. 2a and Fig. 2b. The morphology of the powders was probed by SEM and shown in Fig. 2c and Fig. 2d. The results indicate that the fabricated CNPs are uniform with the near-spherical shape and an average particle size of about 20 nm.

The CNPs/AgNWs nanocomposites was synthesized in the decoration procedure, CNPs powder was added into the AgNWs solution and stirred for 2h. Finally, the CNPs/AgNWs composite was achieved by filtration, washing, and drying. The morphology of the obtained CNPs/AgNWs sample was observed by SEM and presented in figure 3a. The result indicates that the nanocomposites were successfully synthesized with a large amount of the CNPs decorated firmly on the surface of the AgNWs. This would be beneficial for the transfer of the electrons to the surface, improving the electron-hole separation and boost the photocatalytic activity of the composite [7, 8].

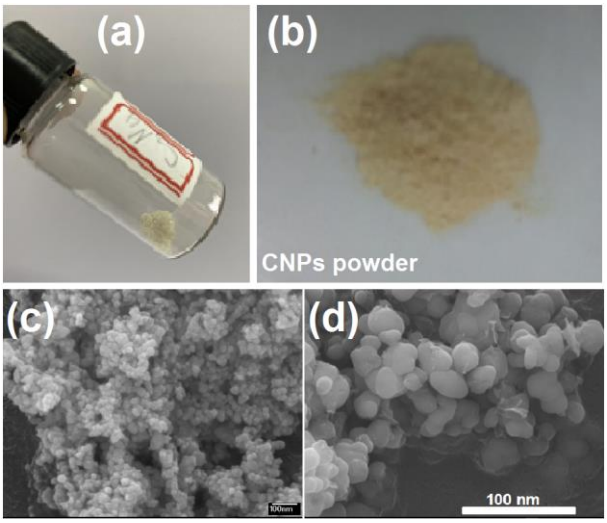

Fig. 2 (a), (b) The as-synthesized CNPs powder, and (c), (d) their SEM images

The as-fabricated CNPs/AgNWs nanocomposites then was used to prepare CNPs/AgNWs cellulose ester membranes by using the wet phase inversion process [15]. In that process, CNPs/AgNWs composite was dispersed in polymer matrix. Fig. 3b shows that the dispersion is uniformly. Fig. 3c shows the real image of the prepared CNPs/AgNWs cellulose ester membrane scattered on a class petri-dish.

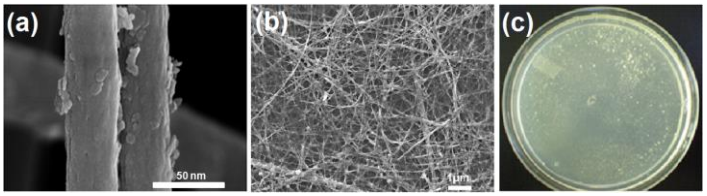

Fig. 3 SEM images of (a) the AgNWs decorated by CNPs and (b) The distribution of CNPs/AgNWs in polymer matrix and (c) the CNPs/AgNWs cellulose ester membrane

To study the optical properties, the UV-Vis absorption spectra of the samples were collected at room temperature and the results are presented in the figure 4. In case of the synthesized AgNWs sample, we have to note that the UV-Vis absorption goes along with the length direction (known as longitudinal plasma band) and along with the width direction to be called transverse plasma band [16, 17]. Figure 4 shows the UV-Vis spectra of the prepared AgNWs with a standard ultraviolet-visible absorption of pure silver nanowires, indicating the typical characteristic of AgNWs related to the localized surface plasmon resonances [18, 19]. Indeed, the presence of a small absorption peak at 350 nm which is similar to the bulk silver could be attributed to the plasmon response of long silver nanowires, whereas the maximum peak at about 380 nm maybe attributed to the transverse plasmon mode of silver nanowires. However, a peak at 410 nm corresponding to silver nanoparticles did not show up in the spectrum. In case of the CNPs the absorbance curve exposes an absorption edge at around 460 nm, corresponding to a bandgap of 2.270 eV that has been confirmed from other previous studies [4, 8, 20]. The result also shows that the absorption edge of the as-synthesized CNPs/AgNWs exposes a slight shift to 480 nm. Moreover, the light absorption ability of the CNPs/AgNWs is much higher in comparison with the CNPs. In addition, the composite also exhibits a wider range absorption to visible range compared with CNPs, indicating that the open of band gap of the composite which may result from charges transfer from the AgNWs to the CNPs. It is the fact that the wider light absorption range and stronger absorption ability can benefit the photoactivity significantly.

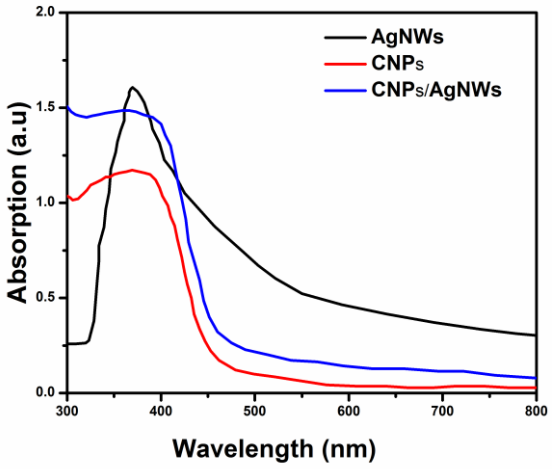

Fig. 4 UV-Vis absorption spectra of the synthesized AgNWs, CNPs and CNPs/AgNWs samples

In order to examine the photocatalytic activity of the synthesized materials and the performance of the membrane, the photodecomposition rate of methylene blue (MB) under visible light irradiation was conducted (Fig. 5). In experiment procedure, the feed stream of MB (100 ppm) is pumped to the coated side of the photocatalytic membrane and flows in parallel with the surface of the membrane. The permeate flow moves through the membrane in a direction perpendicular to the membrane surface while the solar-simulator was placed on top as the light source (Xenon lamp with 400 nm cut-off filter, 500W). The permeate flow was recycled back to the feed tank during the operation. The nanofiltration performance was evaluated after employing the membranes into photocatalytic filtration for different times.

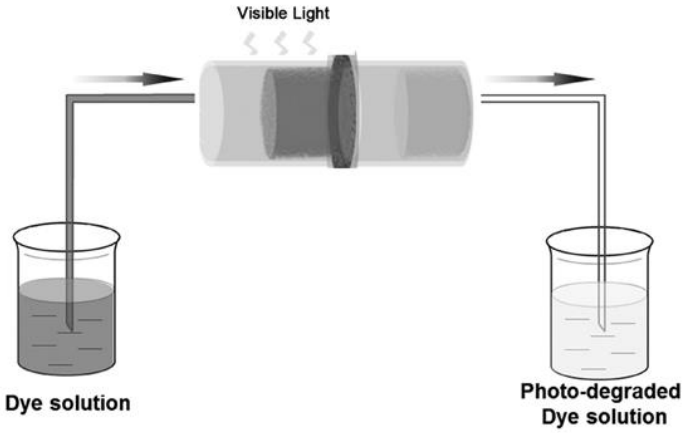

Fig. 5 The photodecomposition rate of methylene blue (MB) under visible light irradiation analysis

Figure 6 illustrates the relation between MB normalized concentration (C/C0) and reaction time of AgNWs, CNPs, and CNPs/AgNWs composite, respectively. The AgNW exhibits a very low catalytic activity with 7% of MB decomposed after 100 mins. In contrast, CNPs shows a higher photocatalytic efficiency with approximately 65 % of degraded dye. Interestingly, by combing CNPs and AgNWs, only 10 % of MB remains in the solution, indicating that visible-light MB degradation is significantly enhanced due to the decoration of CNPs on the surface of AgNWs that reduces the penetration of light into the photocatalyst and generates larger amount of photon adsorbed on the catalyst surface [8]. In addition, it could be attributed that the plasmon effect of AgNWs [21] can enhance electron ejection to CNPs, thus leading to improve photocatalyst efficiency. However, due to the lack of active sites AgNW shows a very poor activity. These results demonstrate that the hybrid materials CNPs/AgNWs is an appropriate material for the best performance with the dye degraded time of 100 min. It also indicates the high performance of membrane in water treatment.

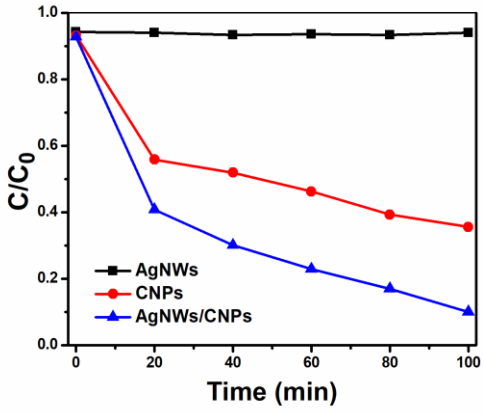

Fig. 6 Methylene blue dyes decomposition of various samples under visible light (> 400 nm)

CONCLUSION

Slive nanowires (AgNWs), carbon nitride nanoparticles (CNPs), a hybrid AgNWs/CNPs composite, and the CNPs/AgNWs membrane were successfully fabricated via a simple route. The characteristics of the as-synthesized materials were systematically studied.

The synthesized AgNWs show the high quality of crystalline structure with an average diameter of 50 nm and an average length of 30 µm. The obtained CNPs powder has a yellow color and are uniform with the near-spherical shape and the average diameter of about 20 nm. The SEM pictures illustrated that the CNPs/AgNWs nanocomposites consisted of a large amount of the CNP nanoparticles decorated firmly on the surface of the AgNWs. This hybrid material not only exposed the wider light absorption range and stronger absorption ability but also exhibited the best performance with the dye degraded time of 100 mins in compare to the individual components. The results indicate that the CNPs/AgNWs composite could be a promising material for the excellent membrane fouling application.

Acknowledgments: This research is funded by the Hanoi University of Science and Technology (HUST) under project number **T2018-TĐ-007**

REFERENCES

1. W. Guo, H.-H. Ngo, J. Li: Bioresource Technology, 122, 2012, 27-34. https://doi.org/10.1016/j.biortech.2012.04.089
2. T. Nguyen, F.A. Roddick, L. Fan: Membranes, 2(4), 2012, 804-840. https://doi.org/10.3390/membranes2040804
3. X. Zhao, Y. Chen, H. Xuan, C. He: New Journal of Chemistry, 40(1), 2016, 441-446. https://doi.org/10.1039/C5NJ02030A
4. G. Mamba, A.K. Mishra: Applied Catalysis B: Environmental, 198, 2016, 347-377. https://doi.org/10.1016/j.apcatb.2016.05.052
5. C. Zhang et al.: Chemosphere, 214, 2019, 462-479. https://doi.org/10.1016/j.chemosphere.2018.09.137
6. J. Zhu, P. Xiao, H. Li, S.A.C. Carabineiro: ACS Applied Materials & Interfaces, 6(19), 2014, 16449-16465. https://doi.org/10.1021/am502925j
7. L. Wang, C. Wang, X. Hu, H. Xue, H. Pang: Chem Asian J, 11(23), 2016, 3305-3328. https://doi.org/10.1002/asia.201601178
8. C. Li, Z. Sun, L. Liu, W. Huang, S. Zheng: RSC Advances, 6(93), 2016, 91002-91011. https://doi.org/10.1039/C6RA17906A
9. B. Lin; et al.: Applied Surface Science, 357, 2015, 346-355. https://doi.org/10.1016/j.apsusc.2015.09.041
10. Y. Liao, S. Zhu, Z. Chen, X. Lou, D. Zhang: Physical Chemistry Chemical Physics, 17(41), 2015, 27826-27832. https://doi.org/10.1039/C5CP05186J
11. S. Bellamkonda, R. Shanmugam, R.R. Gangavarapu: Journal of Materials Chemistry A, 7(8), 2019, 3757-3771. https://doi.org/10.1039/C8TA10580D
12. Z. Cheng, L. Liu, S. Xu, M. Lu, X. Wang: Scientific Reports, 5(1), 2015, 10718. https://doi.org/10.1038/srep10718
13. B. Bari; et al.: Journal of Materials Chemistry A, 4(29), 2016, 11365-11371. https://doi.org/10.1039/C6TA03308C
14. G. Malandrino, S.T. Finocchiaro, I.L. Fragalà: Journal of Materials Chemistry, 14(18), 2004, 2726-2728. https://doi.org/10.1039/B408981B
15. J.M. Gohil, R.R. Choudhury: Chapter 2 - Introduction to Nanostructured and Nano-enhanced Polymeric Membranes: Preparation, Function, and Application for Water Purification. In.: *Nanoscale Materials in Water Purification*, edited by S. Thomas, D. Pasquini, S.-Y. Leu, D. A. Gopakmar, Elsevier, p. 25-57, https://doi.org/10.1016/B978-0-12-813926-4.00038-0
16. B. Liu; et al.: Nanoscale Research Letters, 12(1), 2017, 212. https://doi.org/10.1186/s11671-017-1963-6
17. D. Rossouw, G.A. Botton: Physical Review Letters, 110(6), 2013, 066801. https://doi.org/10.1103/PhysRevLett.110.066801
18. M. Rothe; et al.: Scientific Reports, 9(1), 2019, 3859. https://doi.org/10.1038/s41598-019-40380-5
19. K. Guo; et al.: Journal of Materials Chemistry A, 1(24), 2013, 7229-7234. https://doi.org/10.1039/C3TA10495H

20. J. Liu, T. Zhang, Z. Wang, G. Dawson, W. Chen: Journal of Materials Chemistry, 21(38), 2011, 14398-14401. https://doi.org/10.1039/C1JM12620B

21. J. Niedziółka-Jönsson, S. Mackowski: Materials, 12(9), 2019, 1418. https://doi.org/10.3390/ma12091418

OPEN ACCESS

ACTA METALLURGICA SLOVACA

2020, VOL. 26, NO. 3, 104-110

RESEARCH PAPER

PROGRESSIVE CMT CLADDING FOR RENOVATION OF CASTING MOLD

Janette Brezinová [1]*, Miroslav Džupon[2], Ján Viňáš[1], Anna Guzanová[1], Viktor Puchý[2], Jakub Brezina[1], Dagmar Draganovská[1], Marek Vojtko[2]

[1] Department of Engineering Technologies and Materials, Faculty of Mechanical Engineering, Technical University of Košice, Mäsiarska 74, 040 01 Košice, Slovakia

[2] Institute of Materials Research, Slovak Academy of Sciences, Watsonova 47, 040 01 Košice, Slovakia

*Corresponding author: janette.brezinova@tuke.sk, tel.:+421556023542, Faculty of Mechanical Engineering, Technical university of Košice, 042 00, Košice, Slovakia

Received: 08.06.2020
Accepted: 30.07.2020

ABSTRACT

The paper presents the results of the research focused on the possibility of renewal of molded parts of molds in high-pressure casting of aluminum alloys by arc cladding. Two materials - Thermanit 625 and Thermanit X - were tested. Cladding layers were produced by CMT - Cold Metal Transfer technology in a protective atmosphere of Ar. The clad resistance in the molten melt of the aluminum alloy EN AB AlSi8Cu3 for 120 and 300 minutes was evaluated. Furthermore, ball-on-disc wear resistance of clads was assessed. The results were compared with the reference material - AISI / SAE 309 base tool steel.

Keywords: high pressure casting, cladding, high temperature corrosion, ball-on-disc

INTRODUCTION

High-pressure die casting technology (HPDC) is a balanced system of interrelations between the properties of aluminum alloy melt, the design of mold including the inlet and venting as well as conditions of mold cavity filling, in particular the melt velocity in mold and the hydrodynamic pressure [1]. Die-casting technology is a complex of interrelationships between alloy properties, mold design, and die casting operations. From the point of view of production efficiency and improvement of casting quality, besides technological parameters of die casting metal, the design solution of the mold and its technological service life are decisive. The technological service life of the mold is limited by the quality requirements prescribed for the casting and by the tolerance interval of the technological parameters for die casting. Molded parts and cores for aluminum alloy casting are usually made of chromium and chromium molybdenum tool steels. In the die casting process, molded parts and cores are subjected to intense thermal, mechanical and chemical loads. High melt flow rates of aluminum alloys (up to 120 $m.s^{-1}$), high pressures (up to 120 MPa) and high maximum surface temperatures of the molded parts (up to 550°C) lead to erosion, abrasion, corrosion and thermal fatigue of the mold. The heat load of the foundry cores is even higher (up to 600°C) because they are not connected to the mold cooling system. Thermal cyclic loading from 80°C to 550°C leads to high tensile stresses on the surface of mold, core moldings and consequently to the formation and propagation of thermal cracks. [2-4] Frequent contact of the molding surface with the melt causes the formation of build-ups (sticking) due to corrosion and consequently shortening the service life of the molding parts and cores. Any decomposition change of mold parts and cores will also affect the quality and dimensions of castings [5].

A key component of this technology is the mold and mainly its shape part - the mold inserts. The goal of the research is the renovation of surface which include arc cladding methods and are nowadays very actual. [6-9] Optimization of arc processes are oriented to reduce the heat input underlayer. [10-13] To reduce the number of defects and beginning of nucleation unwanted phases such as heterogenic areas. These are in the middle and high alloy steel located in heat affected zone under cladding layers. [14-17] One of the possibilities of restoring functional surfaces of injection molds or coremakers is with arc welding by CMT (Cold Metal Transfer) [18-20]. As an improvement of short circuit GMAW process, cold metal transfer (CMT) welding is characterized by low heat input, spatter free metal transfer, excellent gap-bridging ability and elegant bead formation. Molds renovated this way are heat-treated and machined to the required dimensions and surface quality. Latest published research on mold restoration by welding aims to identify ways and possibilities to increase mold surface lifetime using CMT welding and to verify the suitability of the chemical composition of newly developed additive materials for mold restoration [21-25].

During the production of aluminum castings, the aluminum melt comes into contact with the mold surface. It is necessary to ensure the correct filling of the mold cavity, the direction of metal flow in the mold cavity, so that its walls do not wear prematurely and to limit the local temperature rise, which would lead to excessive wear and deterioration of the surface cleanliness of the casting. The aim is to choose the mold material so as to ensure good wear resistance and a low coefficient of friction [26-36].

The aim of the research is testing of Ni and Fe based materials for purpose of HPDC mold restoration by CMT welding. Tests were focused on resistance of weld clads against dissolution in AlSi8Cu3 aluminum alloy melt and wear resistance.

MATERIAL AND METHODS

Cladding process

In the CMT process, when the electrode wire tip makes contact with the molten pool, the servomotor of the 'robacter drive' welding torch is reversed by digital process control. This causes the wire to retract promoting droplet transfer. During metal transfer, the current drops to near-zero and thereby any spatter generation is avoided. As soon as the metal transfer is completed, the arc is re-ignited and the wire is fed forward once more with set welding current reflowing [12, 22, 37].

A typical CMT welding electrical signal cycle can be defined as the period required to deposit a droplet of molten electrode into the weld pool. The analysis of current and voltage waveform is essential to study the energy distribution of different phases in droplet transfer process [38]. The cycle is divided into three phases as follows:

(i) The peak current phase: This is a constant arc voltage corresponding to a high pulse of current causing the ignition of the welding arc easily and then heats the wire electrode to form droplet.

(ii) The background current phase: The phase corresponds to a lower current. The current is decreased to prevent the globular transfer of the little liquid droplet formed on the wire tip. This phase continues until short circuiting occurs.

(iii) The short-circuiting phase: In this phase, the arc voltage is brought to zero. At the same time, the return signal is provided to the wire feeder which gives the wire a back-drawing force. This phase assists in the liquid fracture and transfer of material into the welding pool [39].

The complex waveform of the welding current in the CMT process and the 'back feeding' of the filler wire that mechanically forces the metal transfer make it difficult to understand the relation between welding parameters, metal transfer and heat transfer as shown in Fig.1. [22, 27]

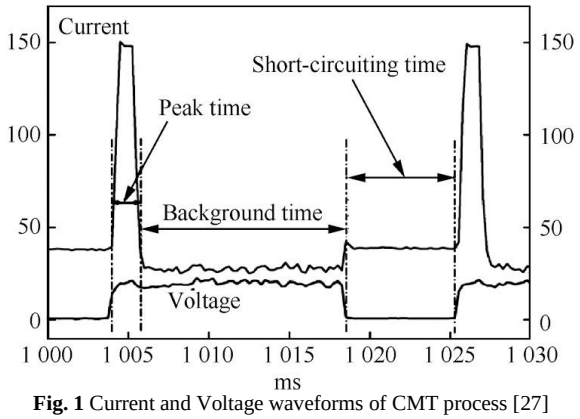

Fig. 1 Current and Voltage waveforms of CMT process [27]

Used filler material

Thermanit 625 (T 625) and Thermanit X (T X) welds were deposited on steel plates of 10 mm thick, made from AISI/SAE 309 (1.4828) steel using Fronius Trans Puls Synergic 5000 by CMT - Cold Metal Transfer welding machine in protection atmosphere of Ar. Welding parameters: 155 A, 16.5 V, 8.5 m.min^{-1}, wire feed 8 m.min^{-1}. Spectral chemical analyzer Belec Compact Port was used for chemical composition of basic material (BM) and weld clads. Chemical composition is given in Table 1. Mechanical properties of materials declared by material producer are shown in Table 2.

Table 1 Chemical composition of used materials, wt. % (Fe bal.)

	C	Mn	Si	Cr	V	Mo	Nb	Ni	Ti	Co
1.4828	0.075	0.41	1.15	19.48	0.06	0.07	-	13.92	0.01	0.035
T 625	0.004	0.86	0.56	20.42	0.01	8.13	3.1	bal.	0.004	0.004
T X	0.101	7.92	0.86	18.81	0.08	0.02	-	9.85	0.007	0.056

Table 2 Mechanical properties of used materials, average values

	YS [MPa]	UTS [MPa]	Elongation A_5 [%]
1.4828	260	500-750	30
T 625	420	760	30
T X	350	600	40

Immersion test

The test set a goal to simulate real operating conditions in HPDC mold and to find resistance of welds against dissolution in melt processed. Principle laid in immersion of BM and weld clads in the melt of aluminum alloy EN AB 46200-EN AB AlSi8Cu3(DIN EN 1706). Test coupons with dimensions of 20x20x10 mm were taken from BM and T 625 and T X welds. The aluminum alloy was embedded into ceramic crucibles and heated in a laboratory furnace to the melting point of the alloy. The temperature of alloy was maintained at 680±20°C temperature, which is a casting temperature of the alloy in HPDC machine with cold filling chamber. All weld samples were completely immersed in the melt in vertical position during the test for 120 and 300 minutes. After the time period, the samples were removed from the melt and cooled freely in the still air. On both surfaces of the samples, melt freely solidified and created a layer sticked on coupon surface. Coupons were next cut and metallographic sections were made for metallographic analyses using light optical microscope OLYMPUS GX71.
Interactions between the weld of T 625 and T X and solidified melt were observed by EDX microanalyses of element distribution after 120 and 300 minute exposure (680±20°C) using environmental scanning electron microscope SEM EVO MA15 with integrated analytical units EDX and WDX was used. For SEM analyses, regime SEI (Secondary Electron) with an accelerating voltage of 20 kV and a distance from the sample surface of 10 mm were used, and BSE (Backscaterred Electron) regime – allowing to observe chemical contrast.

Wear resistance test

Surfaces of welds were processed by grinding to a surface roughness Ra < 0.2 μm. Dry friction wear test (ball-on-disc) was performed on tribometer HTT, by CSM Instruments. Testing conditions: room temperature, 45% relative humidity, SiC ball of 6 mm in diameter, track radius varied from 3 to 7 mm, linear ball speed was 0.1 m.s^{-1}, the normal load Fp was 3N, 5N and 10N, respectively. During the test, tangential forces were measured, and friction coefficients were calculated. Wear tracks were subsequently observed by scanning electron microscopy and wear patterns, type of damage, and wear micromechanisms were identified. The mass losses of the materials were measured by the confocal profilomether and the specific wear rates (W) were calculated based on the volume loss (V) at the distances (L) and the normal load (Fp) according to ISO 20808.

RESULTS AND DISCUSSION

Metallographic sections through BM (Fig. 2 a) and a transition area to clad (Fig. 2 b, c) – solidified met interface. In both cases clads reacted with the aluminum alloy melt with different intensity, creating layer of reaction products on the phase interface.

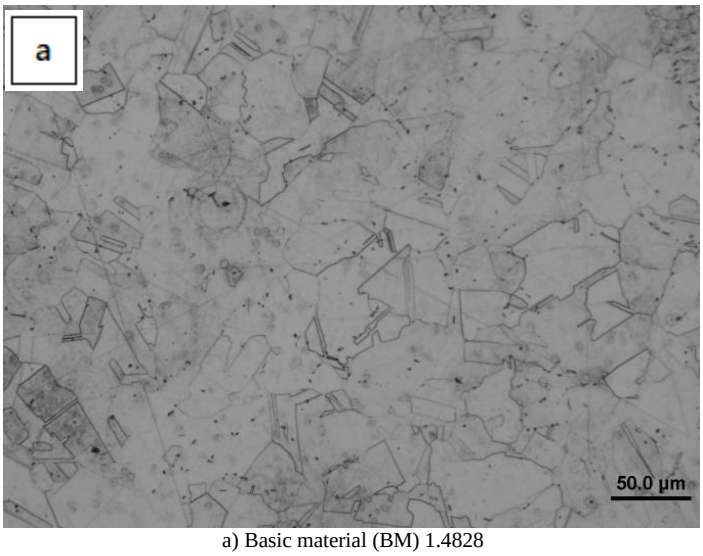

a) Basic material (BM) 1.4828

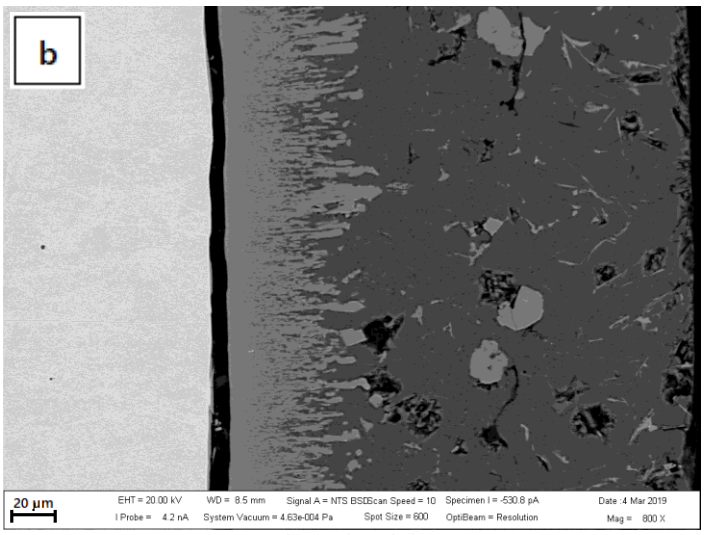

b) BM/680°C/300´/AlSi8Cu3

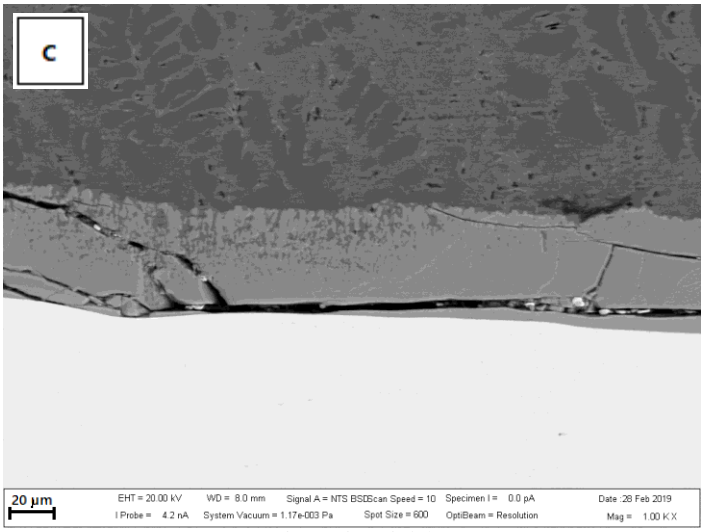

c) BM/680°C/120´/AlSi8Cu3

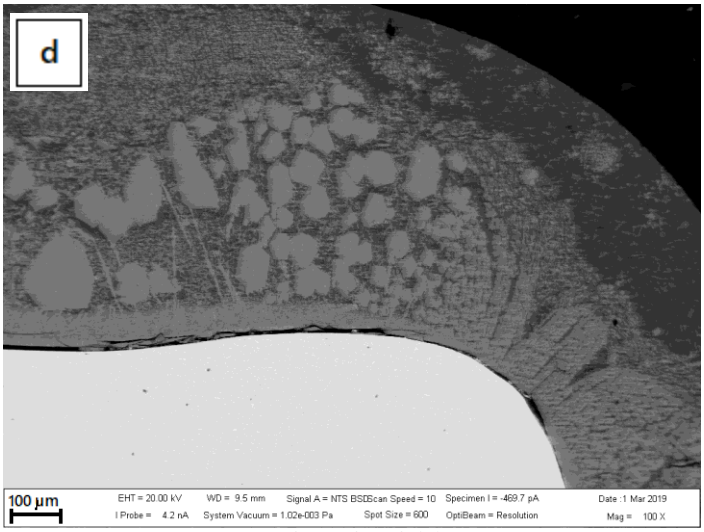

d) T 625/680°C/120´/AlSi8Cu3

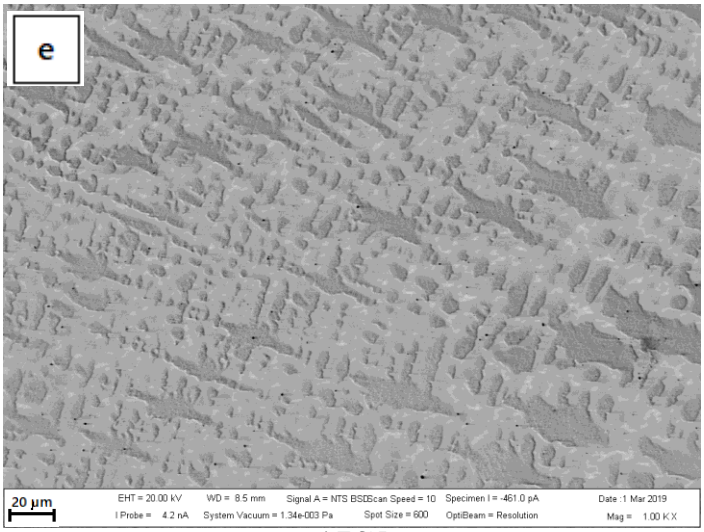

e) T 625

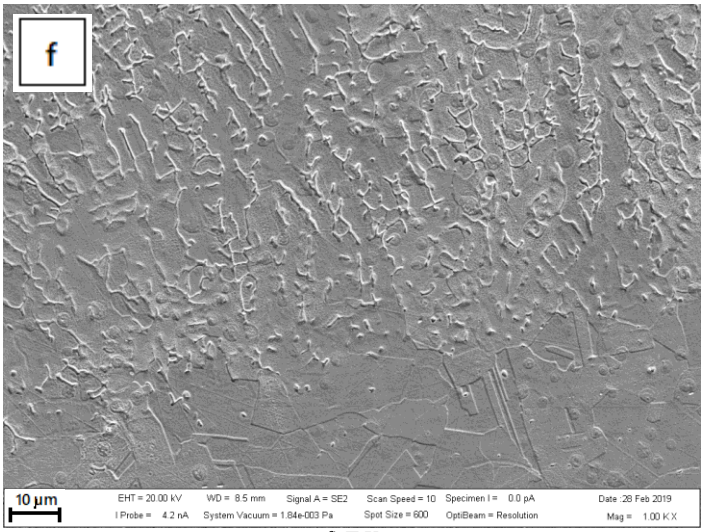

f) T X

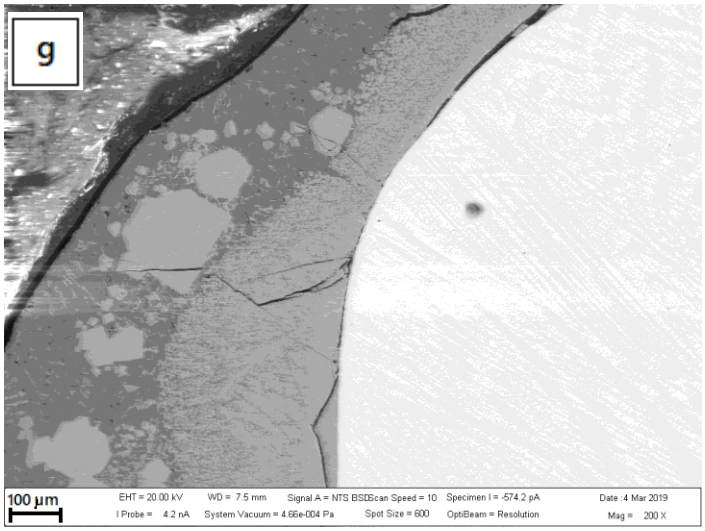

g) T 625/680°C/300´/AlSi8Cu3

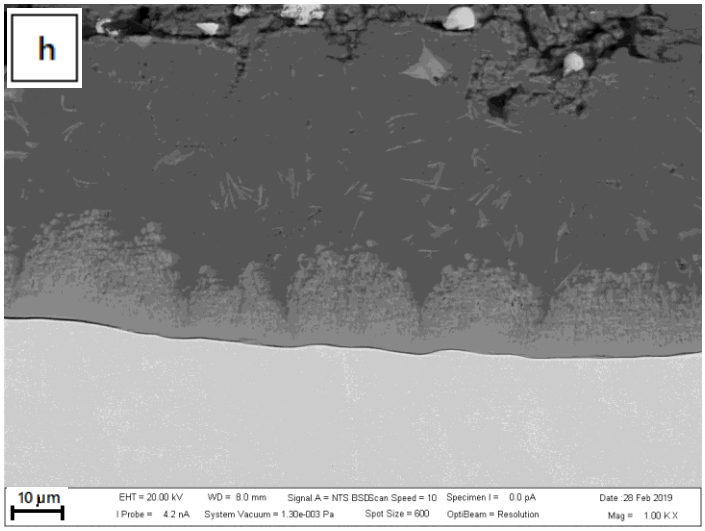

h) T X/680°C/120´/AlSi8Cu3

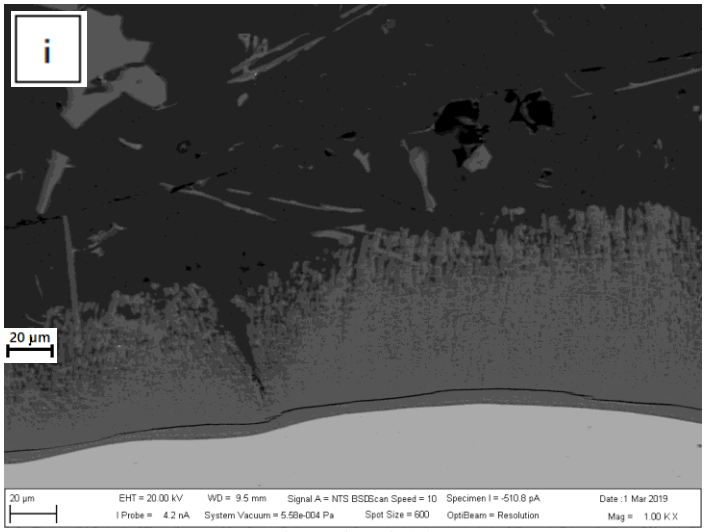

i) T X/680°C/300´/AlSi8Cu3

Fig. 2 Base material and clads T 625 and TX with full immersion in EN ABAlSi8Cu3 aluminum alloy at 680 ± 20 ° C for 120 and 300 min

Based on the microstructure of reaction products layer it can be stated that intense reaction of aluminum melt with T 625 clad took place at the areas of corners and edges of the samples (Fig. 2 d, g). The structure of the clads metal is shown in Fig. 2 e and f. Thickness of reaction products indicated higher resistance of T X clad (Fig. 2 h, i) and base material AISI/SAE 309 against dissolution in the aluminum alloy melt compared to the resistance of T 625 clad. During the 120 and 300 minute exposures of T 625 clad in the aluminum alloy melt a complex reaction of aluminum alloy EN AB AlSi8Cu3 with alloying elements present in the clads was observed. Using the qualitative elemental EDX microanalysis on the surface of the T 625 and T X clads an individual complex phase based on chromium, nickel, iron, molybdenum and niobium were observed in Fig. 3, result in Table 3. and Fig. 4, result in Table 4.

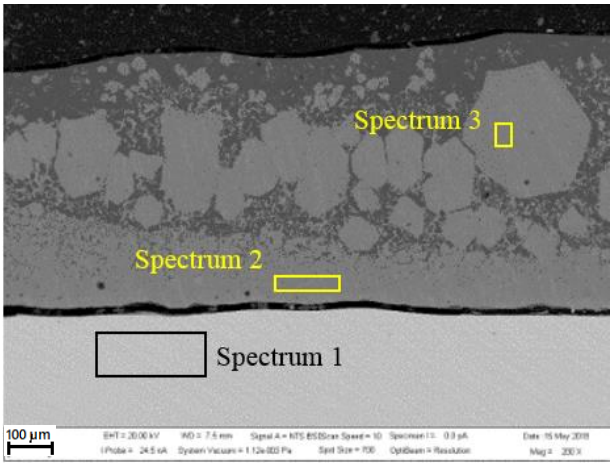

Fig. 3 Thermanit 625/680°C/300´/AlSi8Cu3 – area EDX semiquantitative microanalyses

Table 3 Thermanit 625/680°C/300´/AlSi8Cu3 – results EDX semiquantitative microanalyses

Spectrum 1		Spectrum 2		Spectrum 3	
Elem	Wt. [%]	Elem	Wt. [%]	Elem	Wt. [%]
Al	0.42	Al	53.02	Al	51.17
Si	0.44	Si	9.59	Si	10.89
Ti	0.20	Cr	12.98	Cr	14.40
Cr	21.98	Mn	0.33	Mn	0.58
Mn	0.40	Fe	10.32	Fe	14.15
Fe	15.29	Ni	8.75	Ni	3.39
Ni	52.68	Nb	1.40	Nb	1.05
Nb	2.50	Mo	3.62	Mo	4.37
Mo	6.11	Total	100	Total	100
Total	100				

Spectrum 1 confirms the chemical composition of the Ni deposit T 625 without diffusion of elements from the AlSi8Cu3 melt into the clad material. At the boundary of the deposit and the melt, Al, Si, Cr elements were detected in the solid state in concentrations corresponding to the composition of the melt, which formed the base of the compact interetallic layer. In the region formed by the solidified melt AlSi8Cu3 and the mixture of intermalic phases based on Al-Si-Nb-Cr-Fe, elements in the sense of spectrum 3 were detected.
The results of the chemical composition of the investigated areas are consistent with the chemical composition of the materials used. In the sub-clad layers (Spectrum 2), they correspond to the mixing of the additive material with the base material due to the used arc cladding technology.

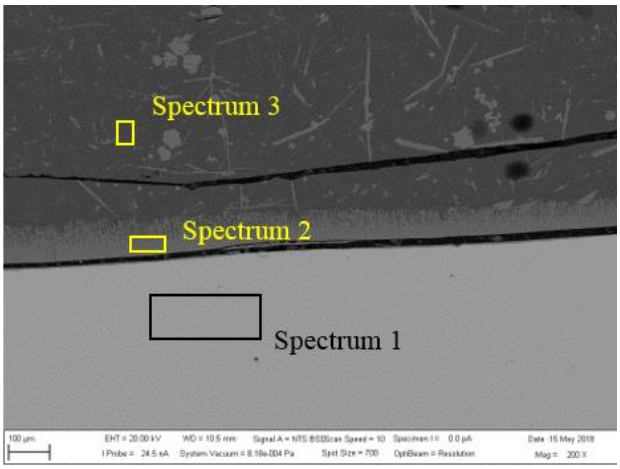

Fig. 4 Thermanit X/680°C/300´/AlSi8Cu3 – area EDX semiquantitative microanalyses

100 µm

Table 4 Thermanit X/680°C/300´/AlSi8Cu3 – results EDX semiquantitative microanalyses

Spectrum 1		Spectrum 2		Spectrum 3	
Elem	Wt. [%]	Elem	Wt. [%]	Elem	Wt. [%]
Si	1.03	Al	61.62	Al	57.05
Cr	19.93	Si	9.49	Si	14.52
Mn	6.06	Cr	7.18	Mn	0.58
Fe	64.15	Mn	1.77	Fe	27.19
Ni	8.83	Fe	19.93	Ni	0.66
Total	100	Total	100	Total	100

The T X cladding layers formed a reaction product based on Al-Fe-Si-Cr-Mn, spectrum 2. When comparing the compact phase formed on the clads, the Ni-based T 625 cladding layers has a higher tendency to dissolve in the melt. The melt resistance of the AlSi weld T X and the AISI 309 material is comparable with respect to the thickness of the compact layer of intermetallic compounds that have formed at the boundary. Thermal fatigue is a complex of physical and chemical interactions of a flowing melt in a mold cavity. A partial criterion by which we can qualitatively evaluate the resistance to thermal fatigue is the tendency to react the AlSi melt and the clad material. Based on the performed experiments, it is possible to hypothesize that the application of T 625 clad metal to the renovation of the mold surface will not increase the resistance to thermal fatigue due to the higher intensity of dissolution in the melt.

Wear resistance test

After a short initial stage, the course of friction coefficients was stable and reproducible (Fig. 5 a-c). Dependence of the specific wear rate (W) on applied load Fp is shown in Fig. 5 d.

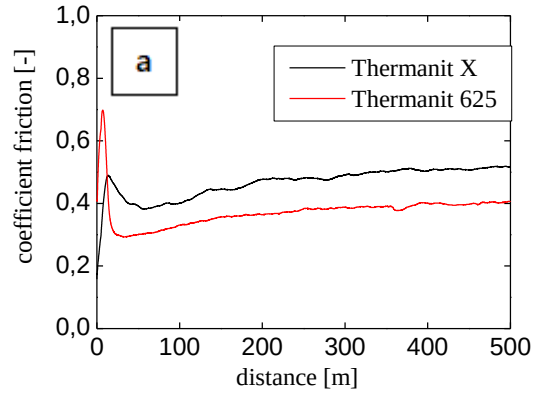

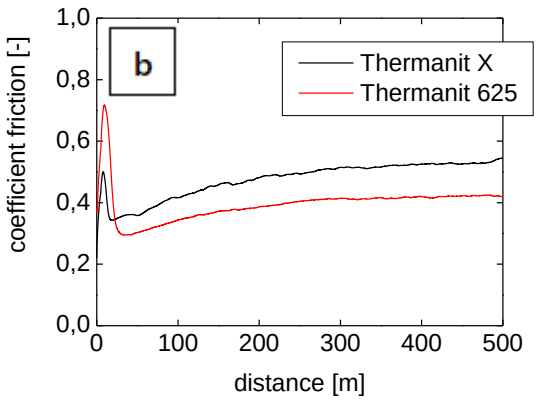

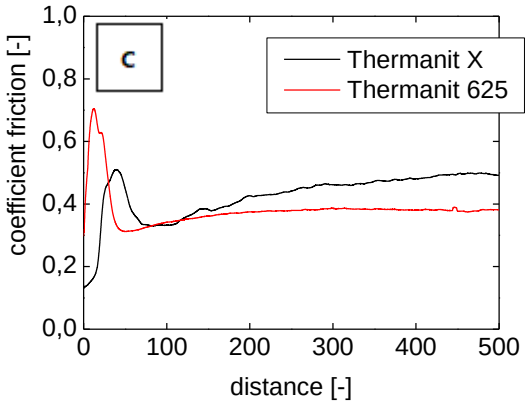

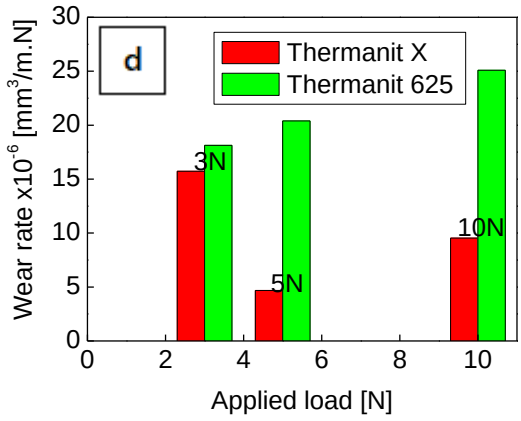

Fig. 5 Course of friction coefficients during tests at loads 3N (a), 5N (b) and 10N (c), dependence of specific wear rate (W) on applied load Fp (d)

Basic tribological characteristics of the clads T 625 and T X are listed in Table 5.

Table 5 Results of tribological test

Materials	Load Fp [N]	Wear track L [m]	Radius [mm]	COF [-] Start	Min.	Max.	Mean	Std. Dev.	Volume loss V [mm^3]	W [×10^{-6} mm^3/m.N]
T 625	3	500	3.0	0.41	0.28	0.75	0.37	0.051	0.0272	18.13
	5	500	4.5	0.38	0.29	0.75	0.40	0.059	0.0510	20.40
	10	500	6.5	0.30	0,29	0.75	0.38	0.062	0.1255	25.10
T X	3	500	7.0	0.16	0,16	0.54	0.47	0.045	0.0236	15.73
	5	500	3.0	0.22	0,22	0.55	0.48	0.057	0.0117	4.68
	10	500	5.0	0.14	0,13	0.55	0.43	0.072	0.0477	9.54

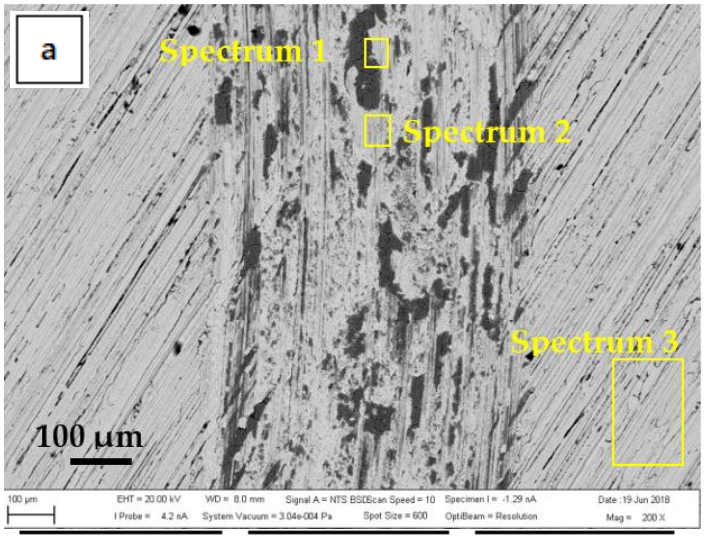

EDX spectrum 1		EDX spectrum 2		EDX spectrum 3	
Elem	Wt. [%]	Elem	Wt. [%]	Elem	Wt. [%]
O	31.89	O	6.59	O	2.13
Si	1.19	Al	0.17	Al	0.36
Ti	0.19	Si	0.88	Si	0.34
Cr	15.18	Ti	0.21	Cr	21.64
Fe	8.85	Cr	20.68	Mn	0.56
Ni	36.27	Mn	0.34	Fe	13.05
Nb	1.65	Fe	12.18	Ni	53.30
Mo	4.79	Ni	50.43	Nb	2.39
Total	100.00	Nb	2.46	Mo	6.23
		Mo	6.05	Total	100.00
		Total	100.00		

b

Fig. 6 Wear track at normal load 10 N: T 625, (a) EDX spectrum, (b) EDX analysis

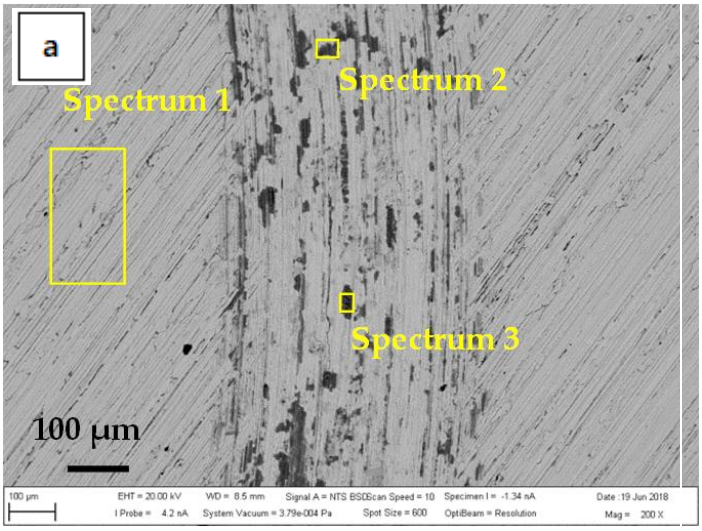

EDX spectrum 1		EDX spectrum 2		EDX spectrum 3	
Elem	Wt. [%]	Elem	Wt. [%]	Elem	Wt. [%]
O	1.57	O	24.62	O	32.88
Si	0.87	Si	2.74	Si	3.43
Cr	19.81	Cr	15.13	Cl	0.34
Mn	6.04	Mn	4.49	K	0.25
Fe	62.91	Fe	46.89	Ca	0.15
Ni	8.80	Ni	6.13	Cr	12.96
Total:	100.00	Total:	100.00	Mn	3.70
				Fe	40.74
				Ni	5.55
				Total:	100.00

b

Fig. 7 Wear track at normal load 10 N: (a) T X EDX spectrum, (b) EDX analysis

In Fig. 6 and 7 document the examined surface area after adhesive wear. The chemical composition at selected locations of the friction surface was determined by EDX analyzes. On the surface of the sample from T 625, the presence of Ni and Cr in particular was recorded in individual spectra. The elements T X san and the surface found elements Si, O and Cr.

CONCLUSION

Immersion test confirmed a complex reaction of aluminum alloy EN AB AlSi8Cu3 with alloying elements present in T 625 clad after 120 and 300 minute exposure especially in the area of corners and edges of the sample. Resistance of T X clad and underlying material AISI/SAE 309 in aluminum alloy melt was higher than the resistance of T 625 clad. Based on the experiments carried out it can be stated that the evaluated types of clads are not suitable for renovation of the shape parts of molds, because the elements are dissolved in contact with the aluminum alloy and degradation occurs in the areas of corners and edges. For this type of renovation a combination of clads and duplex PVD coating can be recommended. Adhesive wear was the dominant wear mechanism. T X and T 625 clad materials were pressed into the surface roughness of the static counterpart - SiC ball. The fragments of the intensively plastically deformed material T X and T 625 during the tribological test formed microbonds that were subsequently broken and formed a wear track pattern. The remains of the pressed material abraded the wear track. Part of energy generated during wear test was dissipated in tribo system and manifested by heat generation. As a result, the temperature of the tribo-couple increased locally. The intense plastic deformation of the surface of the tested clads and the local heating in the air created conditions for local oxidation of a part of the wear track. The complex of tribodegradation factors limiting the service life of functional surfaces is also affected by thermal fatigue. Ongoing cyclic tests of newly formed surfaces show an increase in thermal fatigue resistance of claded surfaces made with T 625 additive material, where the Ni matrix plays an important role, with high resistance to thermal influence. Against the base material, an increase in the resistance to thermal fatigue was also recorded on the cladding layers formed by the T X additive material.

Acknowledgments: This work was supported by scientific grant agency of the Ministry of Education of the Slovak Republic VEGA No. 1/0497/20, KEGA 001STU-4/2019 project of the Slovak Research and Development Agency APVV-16-0359 and the part of project Center for research of control of technical, environmental and human risks for permanent development of production and products in mechanical engineering (ITMS:26220120060).

REFERENCES

1. J. Hirsch: Transactions of Nonferrous Metals Society of China, 24(7), 2014, 1995-2002. https://doi.org/10.1016/S1003-6326(14)63305-7
2. V. Nunes et al.: Surface and Coatings Technology, 332(25), 2017, 319-331. https://doi.org/10.1016/j.surfcoat.2017.05.098
3. J. Viňáš et al.: Materials, 11(4), 2018, 1-13. https://doi.org/10.3390/ma11040459
4. Y. Zhu et al.: Materials Science and Engineering: A, 379(1-2), 2004, 420-431. https://doi.org/10.1016/j.msea.2004.03.020
5. J. Lin et al.: Surface and Coatings Technology, 201(6), 2006, 2930-2941. https://doi.org/10.1016/j.surfcoat.2006.06.024
6. J. Viňáš et al.: International Journal of Materials Research, 104(2), 2013, 183-191. https://doi.org/10.3139/146.110842
7. J. Brezinová et al.: Metals-Basel, 6(36) 2016, 1-12. https://doi.org/10.3390/met6020036
8. J. Brezinová et al.: Metals-Basel, 9(1232), 2019, 1-23. https://doi.org/10.3390/met9111232
9. J. Viňáš et al.: Materials Science Forum, 862, 2016, 41-48. https://doi.org/10.4028/www.scientific.net/MSF.862.41
10. J. Brezinová et al.: Metals-Basel, 10(164), 2020, 1-17. https://doi.org/10.3390/met10020164
11. P. Mohyla, K. Foldynová: Metal Science and Heat Treatment, 56, 2014, 206-209. https://doi.org/10.1007/s11041-014-9732-y
12. K. Furukawa: Welding International, 20(6), 2006, 440-445. https://doi.org/10.1533/wint.2006.3598
13. J. Viňáš et al.: Proceedings of the Institution of Mechanical Engineers, Part B: Journal of Engineering Manufacture, 227(12), 2013, 1841-1848. https://doi.org/10.1177/0954405413493405
14. J. Brezinová et al.: Key Engineering Materials, 586, 2014, 91-95, https://doi.org/10.4028/www.scientific.net/KEM.586.91
15. J. Viňáš et al.: Sadhana-Academy Proceedings In Engineering Sciences, 38, 2013, 477-490. https://doi.org/10.1007/s12046-013-0119-3
16. J. Viňáš et al.: Materials Science, 55(1), 2019, 46-51, https://doi.org/10.1007/s11003-019-00250-x
17. J. Viňáš et al.: Chemické listy, 105(17), 2011, 858-859.
18. J. González et al.: Procedia Manufacturing, 13, 2017, 840-847. https://doi.org/10.1016/j.promfg.2017.09.189
19. J. Viňáš et al.: Materials Science Forum, 862, 2016, 33-40. https://doi.org/10.4028/www.scientific.net/MSF.862.33
20. C.G. Pickin, S.W. Williams, M. Lunt: Journal of Materials Processing Technology, 211(3), 2011, 496-502. https://doi.org/10.1016/j.jmatprotec.2010.11.005
21. M. Marônek et al.: CMT welding of steel sheets treated by nitrooxidation In: *International Conference on Advances in Welding Science and Technology for Construction, Energy and Transportation: AWST 2010, held in Conjunction with the 63rd Annual Assembly of the International Institute of Welding: IIW 2010*: Istanbul: 11-17 July 2010 p. 773-777
22. S. Selvi, A. Vishvaksenan, E. Rajasekar: Defence Technology, 14(1), 2018, 28-44. https://doi.org/10.1016/j.dt.2017.08.002
23. B. Gungor, E. Kaluc, E. Taban, A. Sik: Materials and Design, 54, 2014, 207-211. https://doi.org/10.1016/j.matdes.2013.08.018
24. M. Student et al.: Strojnicky Casopis, 69(4), 2019, 133-146. https://doi.org/10.2478/scjme-2019-0048
25. V. Hutsaylyuk et al.: Vacuum, 2020, 109514, (in print). https://doi.org/10.1016/j.vacuum.2020.109514
26. C. Mitterer, F. Holler, F. Üstel, D. Heim: Surface & Coatings Technology, 125, (1-3), 2000, 233-239. https://doi.org/10.1016/S0257-8972(99)00557-5
27. A. Srivastava, V. Joshia, R. Shivpuria, R. Bhattacharya, S. Dixit: Surface & Coatings Technology, 163-164, 2003, 631-636. https://doi.org/10.1016/S0257-8972(02)00690-4
28. V. Hutsaylyuk et al.: Metals 2019, 9(280), 1-14. https://doi.org/10.3390/met9030280
29. A. Chaus et al.: Journal of Materials Engineering and Performance, 27, 2018, 3024-3034. https://doi.org/10.1007/s11665-018-3387-6
30. Y. Turygin et al.: Investigation of the electron beam positioning accuracy at electron beam welding. In.: *Procedia Engineering, International Conference on Manufacturing Engineering and Materials, ICMEM 2016, 6. - 10. June 2016*, Nový Smokovec, Slovakia, p. 489-494. https://doi.org/10.1016/j.proeng.2016.06.696
31. K. Bobzin, T. Brögelmann, U. Hartmann, N.C. Kruppe: Surface & Coatings Technology, 308, 2016, 374-382. https://doi.org/10.1016/j.surfcoat.2016.09.040
32. Ł. Tomaszewski et al.: Vacuum, 121, 2015, 223-229. https://doi.org/10.1016/j.vacuum.2015.08.027
33. B. Park, D.H. Jung, H. Kim, K.C. Yoo, J.J. Lee, J. Joo: Surface & Coatings Technology, 200(1-4), 2005, 726-729. https://doi.org/10.1016/j.surfcoat.2005.01.064
34. F.J.G. Silva, R.C.B. Casais, R.P. Martinho, A.P.M. Baptista: Journal of Nanoscience and Nanotechnology, 12, 2012, 9187-9194. https://pubmed.ncbi.nlm.nih.gov/23447976/
35. M.F.C. Andrade, R.P. Martinho, F.J.G. Silva, R.J.D. Alexandre, A.P.M. Baptista: Wear, 267(1-4), 2009, 12-18. https://doi.org/10.1016/j.wear.2008.12.114
36. J. Viňáš et al.: Journal of Adhesion Science and Technology, 27(2), 2013, 196-207. https://doi.org/10.1080/01694243.2012.701538
37. Z. Sun et al.: The International Journal of Advanced Manufacturing Technology, 80, 2015, 2007-2014. https://doi.org/10.1007/s00170-015-7197-9
38. J. Feng, H. Zhang and P. He: Materials and Design, 30(5), 2009, 1850-1852. https://doi.org/10.1016/j.matdes.2008.07.015
39. B. Mezrag, F. Deschaux-Beaume, M. Benachour: Science and Technology of Welding and Joining, 20(3), 2015, 189-198. https://doi.org/10.1179/1362171814Y.0000000271

OPEN ACCESS

ACTA METALLURGICA SLOVACA

2020, VOL. 26, NO. 3, 111-115

RESEARCH PAPER

HEAT TREATMENT EFFECT ON INTERFACE MICROSTRUCTURE AND HARDNESS OF A MEDIUM CARBON STEEL CLADDED BY AISI 316 STAINLESS STEEL

Andrea Di Schino[1*]

[1] Università degli Studi di Perugia, Dipartimento di Ingegneria, Perugia, Italy

*Corresponding author: andrea.dischino@unipg.it, Università degli Studi di Perugia, Dipartimento di Ingegneria, Via G. Duranti 93, 06125 Perugia, Italy

Received: 30.05.2020
Accepted: 30.07.2020

ABSTRACT

Aim of this paper is to analyze the interface properties of a austenitic stainless steel cladded by carbon steel. The considered cladding process as performed by an external supplier was performed by submerged arc welding (SAW). A layer is created between stainless steel and carbon steel interface of the cladded plate, caused by chemical element diffusion. High hardness local values were determined in the carbon steel at interface with stainless steel. Heat treatments were carried out aimed to remove such hardness peaks. Results show that a sub-critical heat treatments are not suitable to remove them. On the other hand, microstructure refinement as obtained by quenching and tempering (Q&T) heat treatment allowed e reduction of local steel hardenability with consequent interface hardness reduction.

Keywords: cladding; hardness: heat treatment

INTRODUCTION

Steel clad plates are widely used in several fields [1–3]: among them, carbon steel plates overlaid by nickel containing alloys (especially austenitic stainless steels) are one of the most commonly used material. In fact, they guarantee elevated tensile properties coupled with corrosion resistance, as a consequence of the presence of both carbon and stainless steel. As a matter of fact, due to their surface properties, stainless steels are applied in all fields facing challenging requirements of corrosion resistance [4,5]. It is known that they are widely used in automotive applications [6], as construction and building materials [7,8], in the energy sector [9-11], in aeronautical applications [12] and in food industry [13-15]. Recently many efforts have been carried out aimed to develop stainless steels suitable for 3D printing by selective laser melting [16]. However, their low yield strength does not favor their application as structural materials. Based on the above considerations it is clear that overlaying carbon steel plates by stainless steels properly faces with several engineering applications requiring high tensile properties together with resistance in corrosive environments. Since the cladding layer correspond to about 20% of the total plate thickness, in this family of materials Cr and Ni contents are reduced in comparison to stainless steel plates with a following estimated material cost reduction ranging 30-50% [17, 18]. The most common methods adopted to clad carbon steel plates by stainless steels or Ni alloys include explosion welding [19], roll bonding and welding overlay [20-22]. Focusing about welding overlay, it is worth to be mentioned that many welding methods are nowadays used: shielded metal arc welding (SMAW) [23], submerged arc welding (SAW) [24], tungsten inert gas welding (TIG) [25], CO_2 arc welding [26,27] and laser welding [28]. All these techniques were applied on order to clad Q235 carbon steel plates by AISI 304 stainless steel. It is anyway well known that also austenitic stainless steel could be attacked by corrosion phenomena [29] in severe aggressive environments. This is mainly due to chromium carbides precipitation at steel grain boundaries after material exposition at temperatures ranging 540–860°C. As a consequence of such precipitation, a local Cr content lowering is detected at grain boundaries: therefore the stainless steel loss its corrosion resistance. At same way, also clad plates will behave at the same way [30]. In such materials element diffusion at interface needs to be considered when evaluating the corrosion resistance. Many previous works reported that there is a diffusion width between the carbon steel and the welded overlay, making the stainless steel and carbon steel well bond together [31]. A large literature has been developed concerning, such aspect (*e.g.*[32]). Results showed that chemical element diffusion at the interface, appears is the main mechanism affecting the bonding of steel plate [33–34]. This mechanism is mainly affected by the overlaying conditions, which also a strong effect on microstructure at interface. Carbon and stainless steel interface is characterized by different microstructural features and properties determining the local mechanical characteristic of the clad plate. It is reported that following to element diffusion process a 15 μm layer is formed at interface. Such layer is characterized by stable mechanical characteristics. It is also shown that microstructure is not affected by any grain growth process [35]. The sub surface mechanical properties gradually changes moving along the thickness direction [36]. As a consequence such transition layer is beneficial generating a stable bonding between the two metals. This also assures a good mechanical resistance transition along the thickness. Carburization in the stainless steel side has been found and decarburization in carbon steel is detected [37]. Many studies were carried out aimed to assess the corrosion behavior at the inner surface of ultra-supercritical boilers. Often a hardness peak is detected at stainless/carbon steel interface [38]: such peak needs to be carefully taken as low as possible for the possible deleterious effect they should excerpt in the material performance. Therefore, a specific heat-treatment is required in order to improve hardness values at metals interface [39-45].

Aim of this paper is to analyze the interface properties of a austenitic stainless steel cladded by carbon steel. The effect of heat treatment is reported in terms of microstructure and hardness at interface.

EXPERIMENTAL

Carbon steel was plates sizing 400 mm x 400 x 15 mm were cladded by an external supplier with AISI 316 L. Two welding passes have been performed. The steel was received in the Q&T condition. The two steels chemical composition is reported in Table 1.

Table 1 Chemical composition (mass, %)

Alloy	Cr	Ni	Mo	Mn	C	Fe
AISI 316 L	18	8	1	1.5	0.02	Balance
Steel A	0	0	0	1.0	0.20	Balance

The welding supplier declared plate manufacturing process parameters were: weld metal dilution of 40%, 7 kg/h deposition, a deposit efficiency of 95%. Main welding parameters were: welding current=500 A, arc voltage=30 V, travel speed= 2 mm/s, stick out=35 mm, overlap=9 mm, heat input max=5.3 kJ/mm, preheat temperature=150 °C. A medium-C steel (steel A) was chosen as a substrate. Longitudinal and transverse metallographic specimens, taken from plates have been prepared for metallographic examination. In particular, the bi-metals interface has been assessed by Light Microscopy (LM) and Scanning Electron Microscopy (SEM). The low-alloy steel has been etched by Nital 2%, whilst the microstructure of the AISI 316L weld overlay has been revealed by etching with 50% HNO3+50% H_2O. Hardness through-thickness profiles have been measured (HV_{10}) using steps of 0.3 and 0.5 mm at various locations on longitudinal sections. Specimens have been machined from the clad plate and heat treated at a laboratory scale. The effect of final heat treatment conditions on

hardness and microstructure have been investigated performing some stress-relieving (SR) treatments on specimens machined from the clad plate. The original specimens have been also fully re-treated to simulate a Q&T treatment after cladding of as-rolled plates. The heat treated samples have been assessed for microstructure and hardness. The following cases have been considered:

Table 2 Heat treatment conditions

	Tests	
Material state	**Hardness**	**Microstructure**
Q&T+ cladding	√	√
SR at 640 °C	√	√
SR at 660 °C	√	√
Q&T (920 °C/ 670°C)	√	√
Q&T (980 °/670°C)	√	√
Q&T (1000 °C/670 °C)	√	√

RESULTS

Defects relating to the overlay welding process were not detected. The different welding passes are put in evidence. A first welding pass with 2.0-2.5 mm thickness is detected followed by a second one ranging 1.2-2.0 mm (Figure 1). The heat affected zone (HAZ) is easily recognized in steel A after etching (Figure 2). The coarse grained heat affected zone (CGHAZ) is detected between adjacent welding passes in proximity of the fusion line. A detail of the CGHAZ is reported in Figure 2. Steel A microstructure is that typical of Q&T medium-C steels (Figure 3). The dendritic structure of the weld overlay (second pass) is evident in Figure 4.

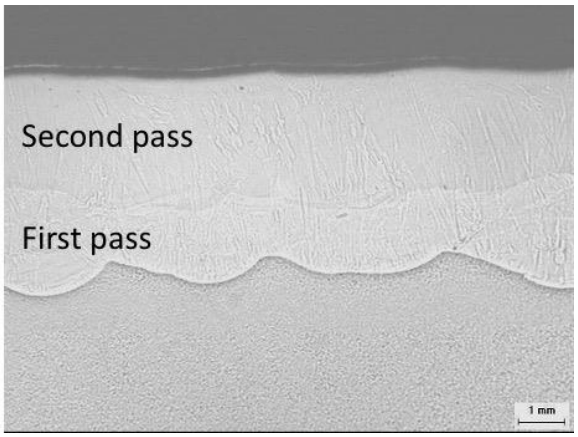

Fig. 1 Weld over-layed material (polished section)

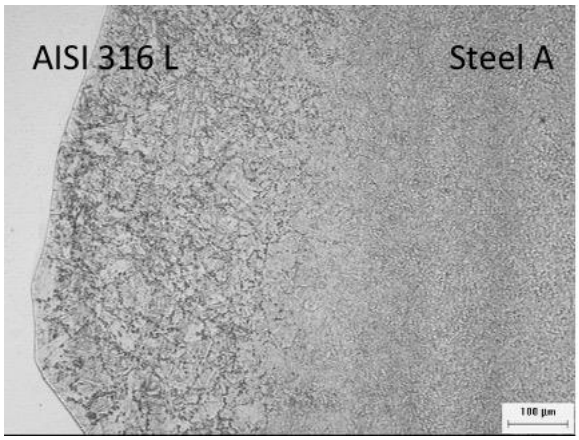

Fig. 2a Detail of CGHAZ (2% Nital etching) (LM image)

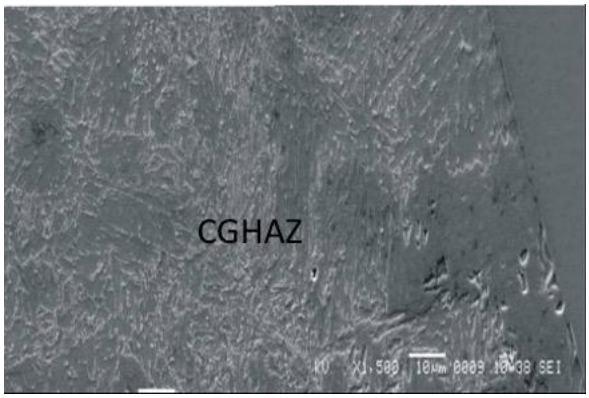

Fig. 2b Detail of CGHAZ (2% Nital etching) (SEM image)

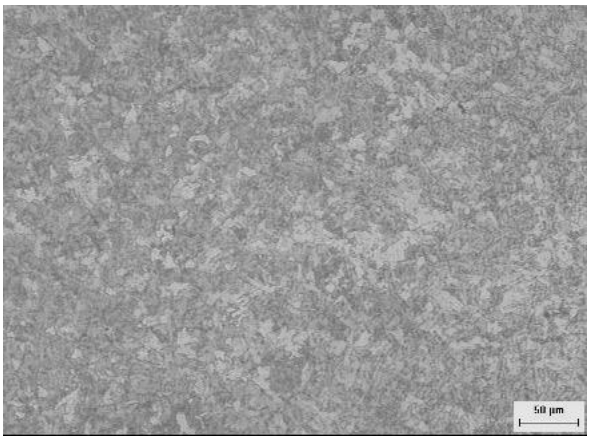

Fig. 3 Steel A substrate (Q&T material)

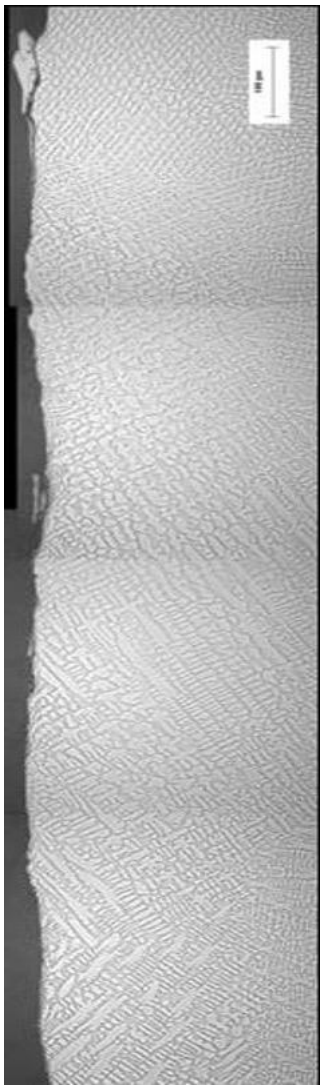

Fig. 4 AISI 316L cladding (etching: 50% HNO3, 50% H2O)

Examples of indentation array adopted to evaluate HV_{10} hardness thickness profiles are reported in Figure 5. The hardness profiles (Figure 6) report hardness peaks (*e.g.* 250 to 270 HV_{10}) in steel A steel in proximity of the fusion line in the coarse grained heat affected zone.

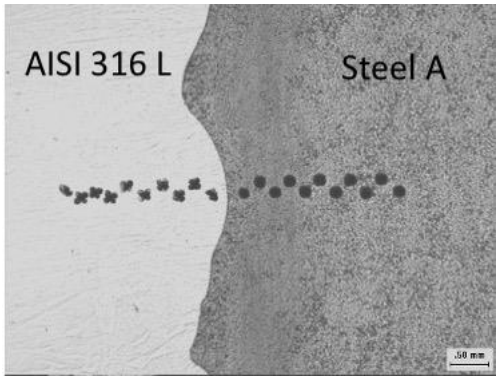

Fig. 5 Interface indentation through thickness profiles

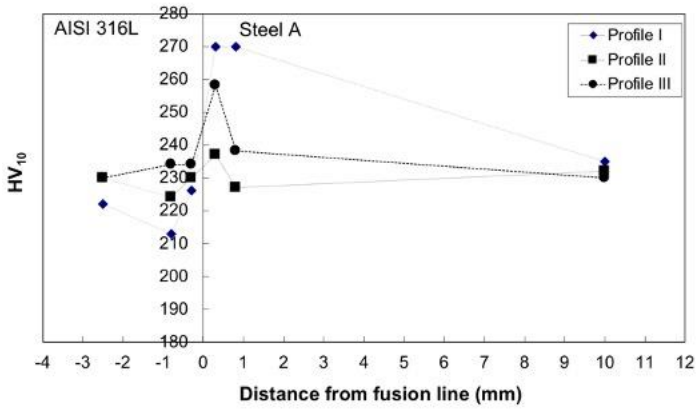

Fig. 6 Interface hardness profiles

Since such hardness peaks are not desired in such kind of products (brittle interface), different heat treatments (as reported in Table 2) were performed aimed to investigate their effect on interface hardness.

SR effect

Measured hardness profiles on the clad material after SR at 640 and 660 °C are reported in Figures 7 and 8. The hardness peaks in the coarse grain heat affected zone (*e.g.* 255 to 260 HV_{10}) are still present after SR, close to the fusion line even if a bit reduced in comparison to the as-received material. This means that SR is not effective to remove hardness peaks in the CGHAZ.

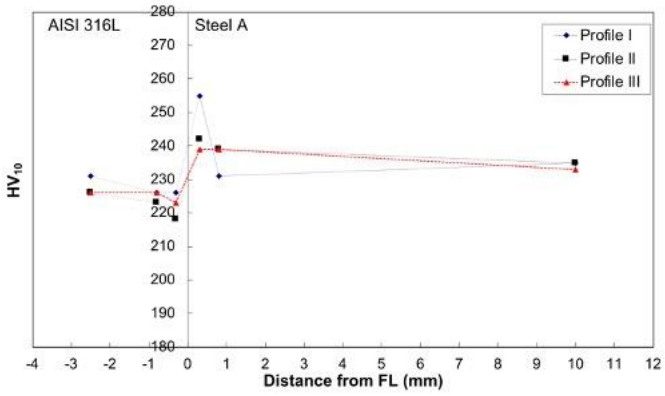

Fig. 7 Interface hardness profiles after SR@ 640 °C

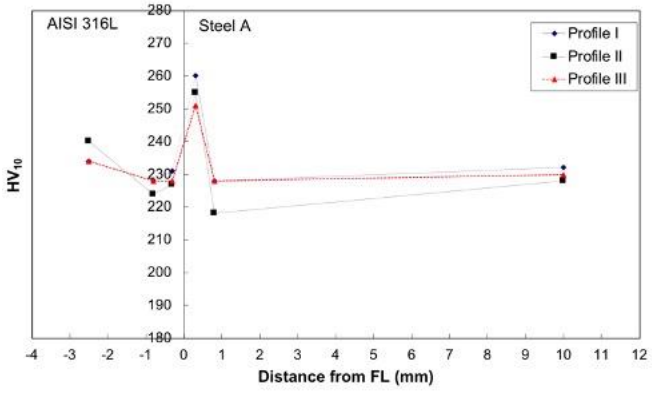

Fig. 8 Interface hardness profiles after SR@ 660 °C

Specimens were quenched and tempered: three different austenitizing temperatures (920 °C, 980 °C and 1000 °C) were exploited aimed to put in evidence the effect of prior austenite grain size; one tempering temperature (670°C) was analyzed, based on results from SR treatment effect, reporting about a poor sub-critical temperature effect. The austenitization temperatures were chosen aimed to reproduce the standard (unclad) medium-C plates austenitizzazione (920 °C), recommended annealing temperatures for AISI 316L stainless steel (980°C and 1000 °C). Such temperatures were also chosen since still practicable in furnaces during an industrial process. The measured hardness profiles on the clad material after quenching and tempering are reported in Figures 9.

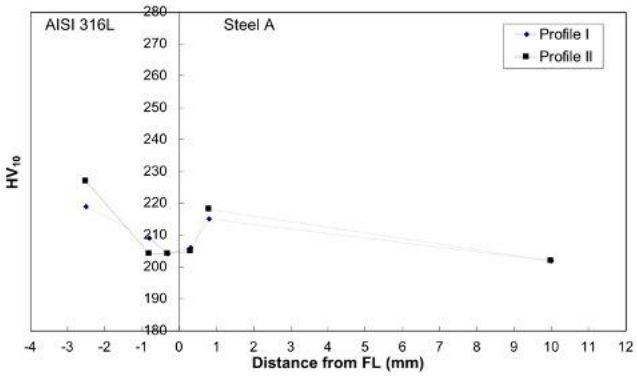

a

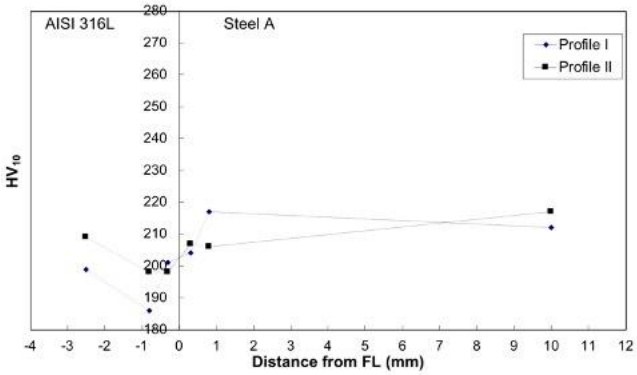

b

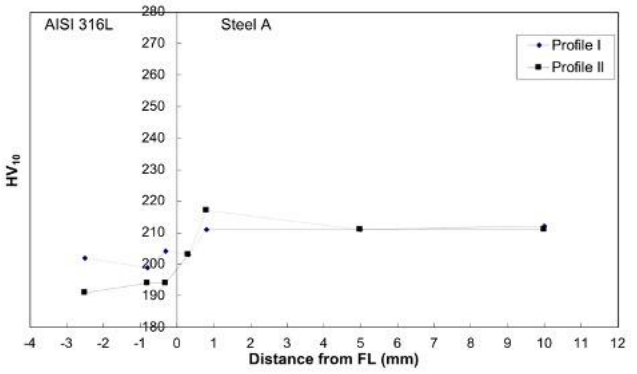

c

Fig. 9 Interface hardness profiles after Q&T at 920 °C/670 °C (a), 980 °C/670 °C (b) 1000 °C/670 °C (c)

The hardness peaks in the coarse grain heat affected zone of the carbon steel, close to the interface, disappeared: as a matter of fact all the measured values are lower than 220 HV_{10}. Microstructures at interface, after quenching and tempering, show a austenite grain size refinement, if compared to as-received material (Figure 10). Such grain refinement reduces the local steel hardenability, thus favoring the formation of lower hardness microstructure.

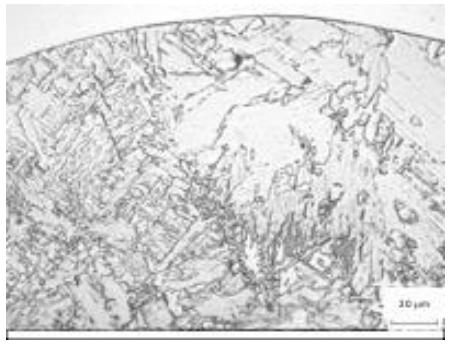

a

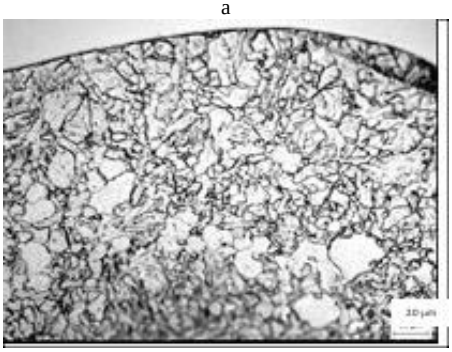

b

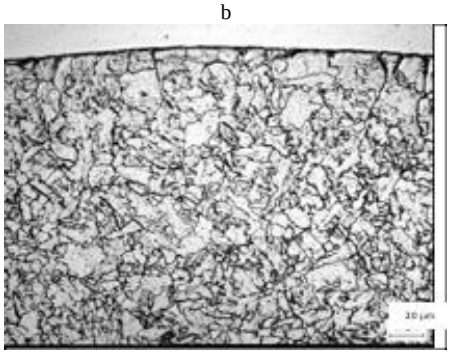

c

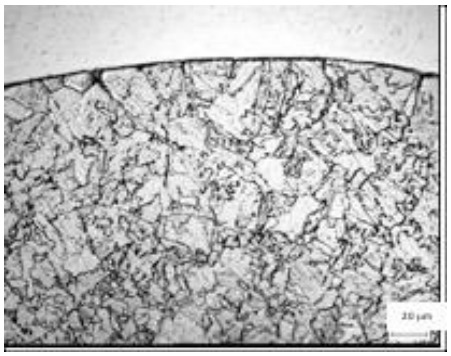

d

Fig. 10 Interface microstructure. a) as received material; b) 920 °C/670°C; c) 980°C/670°C; d) 1000 °C/670°C

The above result suggest that an alternative process route should be followed for manufacturing clad plates, consisting in the weld overlay of as-rolled plate, to be only subsequently quenched and tempered. The experienced temperature,

allowing the hardness peak reduction, as compatible to those of industrial Q&T processes.

CONCLUSIONS

From the results above reported it can be concluded that:

- Some hardness peaks (e.g. 250 to 270 HV10) were revealed in the carbon steel near the fusion line in the coarse grained heat affected zone.
- The hardness peaks in the coarse grained heat affected zone of the carbon steel at 0.3 mm distance from interface, disappeared after quenching and tempering, being all values lower than 220 HV_{10}. This means that the re-austenitizing treatment, carried out at temperatures below those detected at 0.3 mm from interface, implies austenite grain size refining and that such effect promotes hardenability (hence hardness) reduction after tempering.
- This suggest that an alternative process route or manufacturing clad plates, consisting in the weld overlay of as-rolled plate, to be only subsequently quenched and tempered.

REFERENCES

1. K.S. Lee, D.H. Yoon, Kim, H.K., Y. N. Kwon, Y.S. Lee: Mater. Sci. Eng. A, 556, 2012, 319. https://doi.org/10.1016/j.msea.2012.06.094
2. C.Y. Liu, Q. Wang, Y.Z. Jia, R. Jing, B. Zhang, M.Z. Ma, R.P. Liu: Mater. Sci. Eng. A, 556, 2012, 1. https://doi.org/10.1016/j.msea.2012.06.046
3. S.U. Hang, X.B. Luo, F. Chai, J.C Shen, X.J. Sun, F. Lu: J. Iron Steel Res. Int., 22, 2005, 977. https://doi.org/10.1016/S1006-706X(15)30099-6
4. P. Marshall: *Austenitic stainless steels: Microstructure and Mechanical Properties*. Springer, Netherlands, 1984.
5. A. Di Schino: Metals, 10, 2020, 327. https://doi.org/10.3390/met10030327
6. R. Rufini, O. Di Pietro, A. Di Schino: Metals, 8, 2018, 519. https://doi.org/10.3390/met8070519
7. A. Di Schino, P.E. Di Nunzio, G.L. Turconi: Mater. Sci. Forum, 558-559, 2007, 1435. https://doi.org/10.4028/www.scientific.net/MSF.558-559.1435
8. A. Di Schino, J.M. Kenny, G. Abbruzzese: J. Mater. Sci., 37, 2002, 5291. https://doi.org/10.1023/A:1021068806598
9. G. Napoli, A. Di Schino, M. Paura, T. Vela: Metalurgija, 57, 2018, 111.
10. A. Di Schino: Acta Metall. Slovaca, 22, 2016, 266. http://dx.doi.org/10.12776/ams.v22i4.815
11. D.K. Sharma, M. Filipponi, A. Di Schino, F. Rossi, J. Castaldi: Metalurgija, 58, 2019, 347.
12. A. Gloria, R. Montanari, M. Richetta, A. Varone: Metals, 9, 2019, 662. https://doi.org/10.3390/met9060662
13. A. Di Schino, L. Valentini, J.M. Kenny, Y. Gerbig, I. Ahmed, H. Haefke: Surf. Coat. Technol. 161, 2002, 224. https://doi.org/10.1016/S0257-8972(02)00557-1
14. G. Bregliozzi, S.I. Ahmed, A. Di Schino, J.M. Kenny, H. Haefke: Tribol. Lett., 17, 2004, 697. https://doi.org/10.1007/s11249-004-8075-z
15. L. Valentini, A. Di Schino, J.M. Kenny, Y. Gerbig, H. Haefke: Wear, 253, 2002, 458. https://doi.org/10.1016/S0043-1648(02)00140-0
16. C. Zitelli, P. Folgarait, A. Di Schino: Metals, 9, 2019, 731. https://doi.org/10.3390/met9070731
17. A. Di Schino, P.E. Di Nunzio: Acta Metall. Slovaca, 23, 2017, 62. https://doi.org/10.12776/ams.v23i1.852
18. C. Li, G. Quin, Y. Tang, B. Zhang, S. Lin, P. Geng: J. Mater. Res. Tech., 9, 2020, 2522. https://doi.org/10.1016/j.jmrt.2019.12.083
19. Y. Wang, X. Li, X. Wang, H. Yan: Fusion Eng. Des., 137, 2018, 91. https://doi.org/10.1016/j.fusengdes.2018.08.017
20. Q. Qin, D. Zhang, Y, Zang, B. Guan: Adv. Mech. Eng., 7, 2015, 1. https://doi.org/10.1177/1687814015594313
21. Y. Li, H. Liu, Z. Wang: Mater. Sci. Eng. A, 731, 2018, 377. https://doi.org/10.1016/j.msea.2018.06.039
22. A. Mousawi, S. Barrett, S. Al-Hassani: J. Mater. Process. Technol., 202, 2008, 224. https://doi.org/10.1016/j.jmatprotec.2007.09.028
23. M. Tian, H. Chen, Y. Zhang, T. Wang, Z. Zhu: Heat Treat. Metal, 40, 2015, 110. https://doi.org/10.13251/j.issn.0254-6051.2015.06.024
24. T. Qiu, B. Wu, Q. Chen, W. Chen: Neiranji Gongcheng/Chinese Internal Combustion Engine Engineering, 34, 2013, 83.
25. H. Liao, K. Song, Y. Cao, M. Zeng: Hot Working Technol., 41, 2012, 148.
26. W. Wang, Y, Wang, M. Liu, F. Cheng, W. Wu: Hanjie Xuebao/Transactions of the China Welding Institution, 31(6), 2010, 89.
27. J. Zhang, Z. Ju: Steel Constr., 27, 2012, 48.
28. S. Missori, F. Murdolo, A. Sili: Weld J., 83(2), 2004, 65s.
29. J. Xin, Y. Song, J. Fang, J. Wei, C. Huang, S. Wang: Fusion Engineering and Design, 133, 2018, 70. https://doi.org/10.1016/j.fusengdes.2018.05.078
30. G. Aydogdu, M. Aydinol: Corr. Sci., 8, 2006, 3565. https://doi.org/10.1016/j.corsci.2006.01.003
31. H. Li, L. Zhang, B. Zhang, Q. Zhang: Materials, 12, 2019, 509. https://doi.org/10.3390/ma12030509
32. Z. Li, X. Wang, Y. Luo: Materials, 11, 2018, 2326. https://doi.org/10.3390/ma11112326
33. Y. Jing, Y.Qin, A. Zang, Q. Shang, H. Song: J. Alloys Compd., 617, 2014, 688. https://doi.org/10.1016/j.jallcom.2014.07.186
34. B. Liu, J. Wei, M. Yang, F. Yi, K. Xu: Vacuum, 154, 2018, 250. https://doi.org/10.1016/j.vacuum.2018.05.022
35. Z. Dhib, N. Guermazi, A. Ktari, M. Gasperini, N. Haddar: Mater. Sci. Eng. A, 696, 201, 374. https://doi.org/10.1016/j.msea.2017.04.080
36. T. Yu, A. Jing, X. Yan, W. Li, Q. Pang, G. Jing: J. Mater. Process. Technol., 266, 2019, 264. https://doi.org/10.1016/j.jmatprotec.2018.06.007
37. C.X. Chen, M. Liu, B. Liu, F. Yin, Y. Dong, X. Zhang, F: Zhang, Y. Zhang: Fusion Eng. Des., 125, 2017, 431. https://doi.org/10.1016/j.fusengdes.2017.05.136
38. S. Zhang, H. Xiao, X. Xie, L. Gu: J. Mater. Process. Technol., 214, 2014, 1205. https://doi.org/10.1016/j.jmatprotec.2014.01.006
39. A. Di Schino, L. Alleva, M. Guagnelli: Mater. Sci. Forum, 715-716, 2007, 860. https://doi.org/10.4028/www.scientific.net/MSF.715-716.860
40. H. Song, H. Shin, Y. Shin: Ocean Eng., 122, 2016, 278.https://doi.org/10.1016/j.oceaneng.2016.06.042
41. P. Petrousek, T. Kvackaj, R. Kocisko, J. Bidulska, M. Luptak, D. Manfredi, M.A. Grande, R. Bidulsky: Acta Metall. Slovaca, 25(4), 2019, 283. http://dx.doi.org/10.12776/ams.v25i4.1366
42. T. Kvackaj et al.: Journal of Materials Engineering and Performance, 29(3), 2020, 1509-1514. https://doi.org/10.1007/s11665-020-04561-y
43. R. Bidulsky, J. Bidulska, M. Actis Grande: Met. Sci. Heat Treat., 58(11-12), 2017, 734. https://doi.org/10.1007/s11041-017-0087-z
44. R. Bidulsky, M. Actis Grande, E. Dudrova, M. Kabatova, J. Bidulska: Powder Metall., 59(2), 2016, 121. https://doi.org/10.1179/1743290115Y.0000000022
45. R. Bidulsky, J. Bidulska, R. De Oro, E. Hryha, M. Maccarini, I. Forno, M. Actis Grande: Acta Physica Polonica A, 128(4), 2015, 647-650. http://dx.doi.org/10.12693/APhysPolA.128.647

OPEN ACCESS

ACTA METALLURGICA SLOVACA

2020, VOL. 26, NO. 3, 116-121

RESEARCH PAPER

ELEMENT PARTITIONING IN LOW-CARBON Si2Mn2CrMoVNb TRIP-ASSISTED STEEL IN INTERCRITICAL TEMPERATURE RANGE

Vasily Efremenko[1], Roman Kussa[1], Ivan Petryshynets[2], Kazumichi Shimizu[3], František Kromka[2], Vadim Zurnadzhy[1], Victoria Gavrilova[1]

[1] Pryazovskyi State Technical University, (PSTU) vul. Universytets'ka 7, Mariupol 87555, Ukraine

[2] Institute of Materials Research, Slovak Academy of Sciences, Watsonova 1935/47, 040 01, Kosice, Slovakia

[3] Muroran Institute of Technology, 27-1 Mizumotocho, Muroran, Hokkaido 050-8585, Japan

*Corresponding author: vgefremenko@gmail.com, Materials Science, Physics, Pryazovskyi State Technical University, (PSTU) vul. Universytets'ka 7, Mariupol 87555, Ukraine

Received: 14.05.2020
Accepted: 14.08.2020

ABSTRACT

The present paper is aimed at the study of the kinetics of Mn, Si, Cr partitioning in 0.2wt%C-Si2Mn2CrMoVNb TRIP-assisted steel under the annealing at 770 °C and 830 °C to be within the intercritical temperature range. The work was fulfilled using SEM, EDX, dilatometry, and hardness measurements. It was found that under heating a redistribution of the alloying elements between ferrite and austenite took place. Specifically, silicon partitioned to ferrite while chromium diffused to austenite with distribution coefficient values of 1.12-1.21 (K_{Si}) and 0.75-0.86 (K_{Cr}). Manganese was found to partition to a much greater extent resulting in a distribution coefficient of K_{Mn}=0.38-0.50 and 2.6 times higher concentration in austenite as compared to ferrite. As annealing temperature raised from 770 °C to 830 °C the elemental partitioning was accelerated, followed by the decrease in manganese content in austenite (by 1.44 time) and ferrite (by 1.34 time) caused by an increase in austenite volume fraction. Silicon featured uneven distribution within ferrite to be accumulated at the "martensite/ferrite" interface and near ferrite grain boundaries, while manganese was concentrated in MC carbides. The recommendation for annealing holding was formulated based on elemental partitioning kinetics.

Keywords: TRIP-assisted steel; annealing; SEM/EDX; element partitioning; ferrite; martensite

INTRODUCTION

Low carbon Mn-Si(Al) steels with TRIP effect (TRIP-assisted steels) remain attractive for researchers due to improved mechanical properties achieved under the low content of alloying elements [1-3]. They belong to the group of Advanced High Strength Steels (AHSSs) [4]. The distinguishable feature of TRIP-assisted steels is a heterogeneous multiphase structure comprising ferrite, carbide-free bainite, and retained austenite (RA) [5, 6]. According to adopted technology, TRIP-assisted steels are subjected to bainitizing heat treatment with preliminary annealing at intercritical temperature range (ITR), where carbon partitioning between ferrite and austenite takes place [1, 7, 8]. Enriched with carbon austenite retains after bainitizing, holding thus volume fraction of RA in final structure and reaches up to 10-15 vol.% [1, 9, 10]. Retained austenite is the key structural constituent of heterogeneous constructional steels due to its higher ductility and its capability toward strain-induced martensite transformation (TRIP-effect) [11, 12]. TRIP-effect results in enhancement of steel strength/ductility combination [13, 14] as well as in improvement in exploitation behaviour such as abrasive/erosive wear resistance [15-17].

A carbon partitioning between the phase constituents is a common feature of heat processing of different steel grades (TRIP-assisted steels [1, 5], Q&P-steels [18, 19], nanobainite steels [20]). During the intercritical annealing, carbon partitions between ferrite and austenite in order to reach a thermodynamic equilibrium being driven by the big difference in carbon equilibrium solubility in α-Fe and γ-Fe. A high diffusivity of carbon (as an interstitial element) under ITR makes its partitioning very fast. In addition to carbon, other (substitutional) elements (Si, Mn, Cr, etc.) could be involved in partitioning under ITR, affecting the stability of austenite to phase transformations upon bainitizing treatment or cooling [21]. This phenomenon was studied repeatedly to highlight its importance for steel transformation behaviour [22-26]. Zhang et al. [22] found that C, Mn, and Al were partitioning under ITR annealing in 0.05-0.15 wt% C -5 wt% Mn - 3 wt% Al dual-phase steels, greatly affecting austenite volume fraction and stability. Specifically, ITR annealing induced enrichment of austenite with manganese, while ferrite enriched with aluminum. The same results for manganese were reported in [23] for 6 wt% Mn - 1.4 wt% Si TRIP-assisted steel, however no partitioning of Si and Al was observed during inter-critical annealing. Lis et al. [24] found for 4 wt% Mn TRIP-steel that soft annealing at 625 °C led to the enrichment of proeutectoid cementite with Mn; besides this, a non-uniform distribution of Mn between polygonal ferrite/bainite and austenite was detected leading to increase in Mn content up to 10 wt% in martensite-austenite "islands" retained after water quenching. Lee et al. [25] showed for 6 wt% Mn steel that Mn partitioning to austenite increases the stability of retained austenite only when austenite is ultra-fine grained with grain size less than 500 nm. Luo et al. [26] demonstrated that austenite formation in 5 wt% Mn steel at the early stage of ITR annealing was controlled only by carbon diffusion. Furthermore, the newly formed 20 nm-thick austenite was formed without the Mn partitioning; however, after that manganese segregates at the γFe/αFe interface. Park et al. [27] revealed that alloying elements may partition in CMnSiAl TRIP steels not only under intercritical annealing, but under tempering at 400 °C as well.

The literature analysis allows one to conclude that investigation into elements partitioning under ITR annealing is mostly focused on medium-Mn TRIP-assisted steels and dual-phase steels alloyed by 5-7 wt% Mn. At the same time, the distribution of substitutional elements in low-Mn TRIP-assisted steel remains not well studied. Therefore the objective of the present work is to investigate the kinetics of elemental partition in low-carbon 0.2wt%C-Si2Mn2CrMoVNb TRIP-assisted steel under annealing at intercritical temperature range.

MATERIAL AND METHODS

The TRIP-assisted steel with the composition 0.20 wt% C, 1.79 wt% Si, 1.73 wt% Mn, 0.55 wt% Cr, 0.20 wt% Mo, 0.11 wt% V, 0.045 wt% Nb, 0.009 wt% S, and 0.013 wt% P was used in the present work. Steel was smelted in a 120-kg induction furnace and poured in 50 mm-diameter cast ingots which then were electro-slag remelted to produce an 80 mm diameter ingot. This ingot was subsequently forged and then rolled to a 15 mm thick strip with further soft annealing at 900 °C before machining. Then the specimens for dilatometric study (of 2 mm diameter and 20 mm length) and microscopic observation (of 3 mm x10 mm x10 mm size) were prepared. The critical points Ac_1 and Ac_3 were determined by optical dilatometer under the heating with a rate of 1.0 K/s. The isothermal heating was performed in an

electrical furnace in the air atmosphere at 770 ºC and 830 ºC. The holding durations for each temperature were 10 min, 30 min, 60 min, 120 min, and 240 min. After the holding the specimen was quenching in 20 ºC water.

The microstructure of the specimens was characterized using optical microscope (OM) Nikon 200-M and scanning electron microscope (SEM) JEOL JSM-6510. The specimens were prepared according to standard procedure and etched with the 4%-nital reagent. The volume fraction (VF) of ferrite was measured by Rosiwal lineal method [28] using the OM images of the structure. For each holding temperature five micrographs of 440 μm x 600 μm area of the same magnification were used with further averaging the results.

Phase elemental distributions were examined by the EDX method (JED-2300; JEOL). Before EDX analysis the detector was calibrated by the standard Co specimen. The average of five/seven measurements performed in the same phase was considered as phase chemical composition. Since EDX quantitative analysis of carbon in an electron microscope is difficult giving exaggerated carbon content [28], the as-obtained EDX-microprobe results were recalculated considering the total carbon content and its full carbon partitioning according to Fe-C phase diagram. The coefficient of elemental distribution between the α-phase and γ-phase was calculated as [29]

$$K_i = \frac{[i]_\alpha}{[i]_\gamma}, \qquad (1.)$$

where: $[i]_\alpha$ and $[i]_\gamma$ are the content of the i-element in the α-phase and the γ-phase respectively.

The hardness was measured using Vickers hardness tester (Future-Tech) under 30 kg load. The hardness values are an average of five/seven indentations.

RESULTS AND DISCUSSION

The selection of the regime of ITR annealing implies the data on the critical points of the steel. For this purpose, the dilatometric heating curve was analysed and the critical temperatures were found as Ac_1=760 ºC and Ac_3=930 ºC. Further, the specimens were heated from 700 ºC to 930 ºC (10 min holding) with a step of 20-30 ºC. Being heated above Ac_1 (760 ºC) the specimen acquired the ferrite/austenite structure; under the consequential water cooling the austenite transformed to martensite. Fig. 1 illustrates the effect of the temperature on ferrite volume fraction and steel hardness. Increasing the temperature between Ac_1 and Ac_3 leads to alteration of the "ferrite/martensite" ratio in favour of martensite causing the increase in hardness. The volume fraction of ferrite decreases more intensively just below Ac_1 with further slowing when approaching Ac_3. The hardness profile is inversely related to the ferrite VF profile. After holding at 930 ºC the microstructure was martensitic while the hardness reached its highest value (463 HV). From Fig. 1 the temperatures of 770 ºC and 830 ºC were selected for further investigation. The first one corresponded to the microstructure of 50 % ferrite + 50 % austenite while the latter was attributed to the microstructure of 20 % ferrite + 80 % austenite.

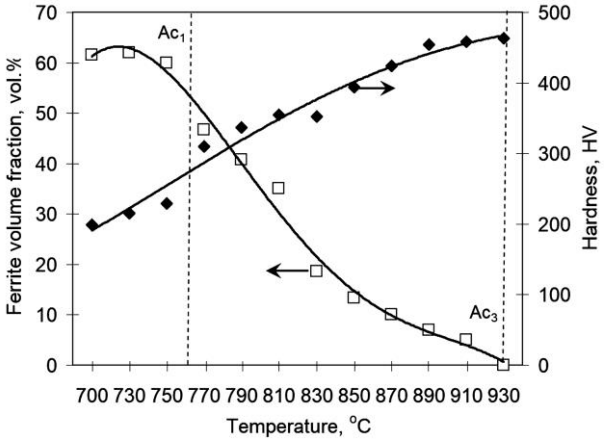

Fig. 1 Effect of the ITR temperature of ferrite volume fraction and steel hardness

Annealing at 770 ºC resulted in the microstructure consisting of ferrite and lath martensite located preferentially along the grain boundaries (Fig. 2). Grainy carbide precipitates were seen in the structure with size varied from 150 nm to 20 nm and lower. The coarse precipitates were mostly positioned in martensite areas to be associated with grain boundaries, whereas the fine nano-scaled precipitates were mostly found within the grains. Considering the presence of V and Nb in steel composition, the precipitates were assumed as a complex MC carbide ((V, Nb)C) precipitated at preliminary stages of steel manufacturing. Taking into account the size of microstructural constituents and the spatial resolution of EDX quantitative analysis (2-3 μm), the sites for the EDX-point analysis were selected in the inner part of ferrite grains or martensite areas to avoid the effect of the surrounding areas (Fig. 2, b).

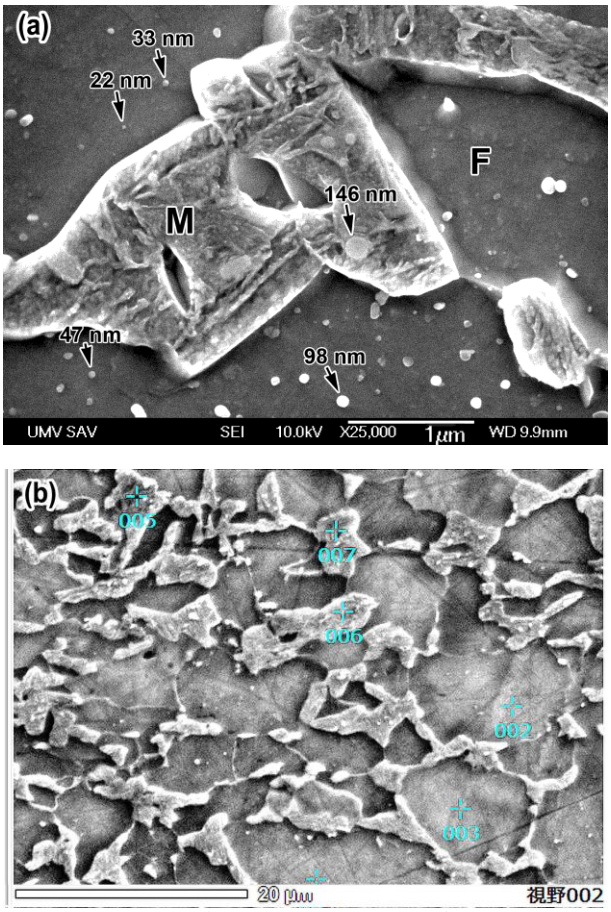

Fig. 2 The microstructure after holding at 770 ºC: (a) ferrite (F) and martensite (M) with the carbide precipitates, (b) the sites of EDX-point analyzing

As seen from Fig. 3, a, with holding time increasing the silicon content in ferrite increased from 1.83 wt% (10 min) to 2.04 wt% (60 min) with further stabilizing at this level. It was accompanied by continuous depleting of ferrite with manganese from 1.06 wt% (10 min) to 0.86 wt% (240 min). The chromium content remained stable during the entire holding duration (variation in the range of 0.58±0.03 wt%). The opposite behavior was observed for the martensitic areas (Fig. 3, b): the manganese content gradually increased from 2.12 wt% to 2.26 wt%, while silicon content decreases from 2.04 wt% with at 1.81 wt% stabilizing after 120 min holding. Also, the chromium content slightly increased in martensite from 0.68 wt% to 0.79-0.81 wt%.

The above values were extracted from the EDX-point analysis made in the core part of the ferrite/martensite areas. In contrast, the EDX observation in "scanning" modes gives more detailed information of elements' distribution. As seen from Fig. 4, manganese and silicon were unevenly distributed along the line crossing ferritic grains and martensitic areas. The Mn concentration was higher within the martensite plots (marked by the lines in Fig. 4, a). There were Mn "spikes" within martensite areas and ferrite grains associated with carbide precipitates (circled by the dotted line). Manganese content gradually decreased

from the "martensite/ferrite" interface towards the center of ferrite grain. Silicon was more unevenly distributed as compared with manganese. The mean concentration of silicon was higher in ferrite grains, however the spikes in Si concentration were revealed exactly near the "martensite/ferrite" interface. Mostly the Si-rich zones were situated in ferrite grains (Si-peaks 3, 5, and 6 in Fig. 4, a), but Si-spikes inside the martensite area were seen as well (Si-peak 1 and 2). Also, the Si-rich zone was detected at the "ferrite/ferrite" boundary (Si-peak 4). After the prolonged (240 min) holding at 770 ºC, silicon profile retained the above-described character with Si segregation in the vicinity of the "martensite/ferrite" boundary and Si-depletion inside the grains (Fig. 4, b).

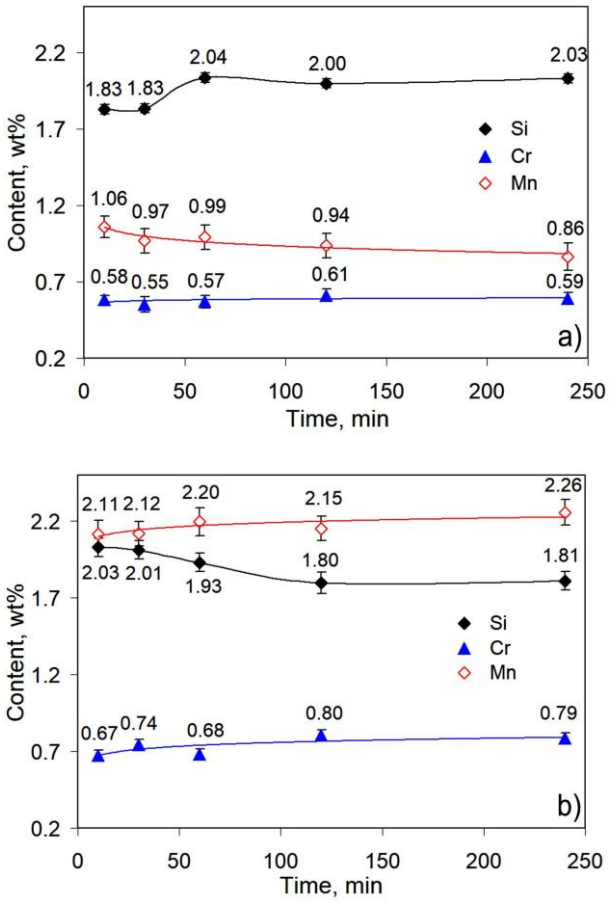

Fig. 3 Effect of holding at 770 ºC on Si, Mn, and Cr content in (a) ferrite and (b) martensite

EDX-mappings for Mn and Si are presented in Fig. 5. It is clear that the Mn-enriched areas almost completely matched the contours of martensite areas (taken from secondary electron image (SEI) in Fig. 5, a). Only two local Mn-rich areas in Fig. 5, b were not associated with martensite: a carbide aggregation (see double arrows) and the ferrite grain next to the "martensite/ferrite" interface (see the arrow). Silicon is mostly concentrated in the ferrite grains as an edging of 2-5 μm thick around the martensite areas (Fig. 5, c). The inner zones of ferrite grains are Si-depleted. Most of the silicon is concentrated in ferrite, however Si content in some martensite areas is increased (see the arrow in Fig. 5, c).

The results of EDS point analysis for the annealing at 830 ºC are presented in Fig. 6. As follows from this figure, the chemical compositions of ferrite grains and martensite areas were not significantly affected by the holding time. Only a decrease in manganese content in ferrite was noted from 0.79 wt% (10 min) to 0.59 wt% (30 min) at the early stage of the holding (Fig. 6, a). Also, silicon content in ferrite varied in a rather wide range (2.04-2.27 wt.%) caused by the smaller ferrite grains resulting in EDS-"effect" of neighbouring martensite.

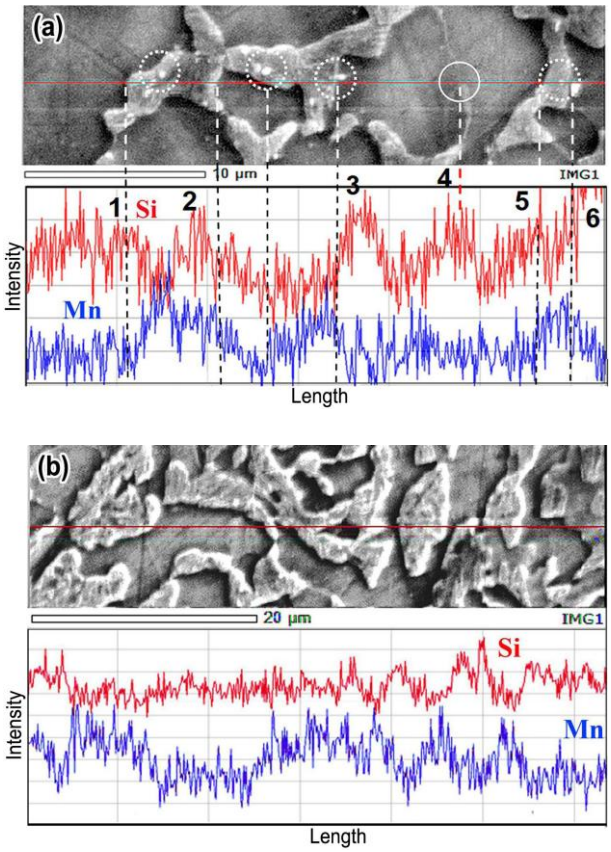

Fig. 4 SEI images of the microstructure and the profiles of Mn and Si (holding at 770 ºC for (a) 10 min and (b) 240 min)

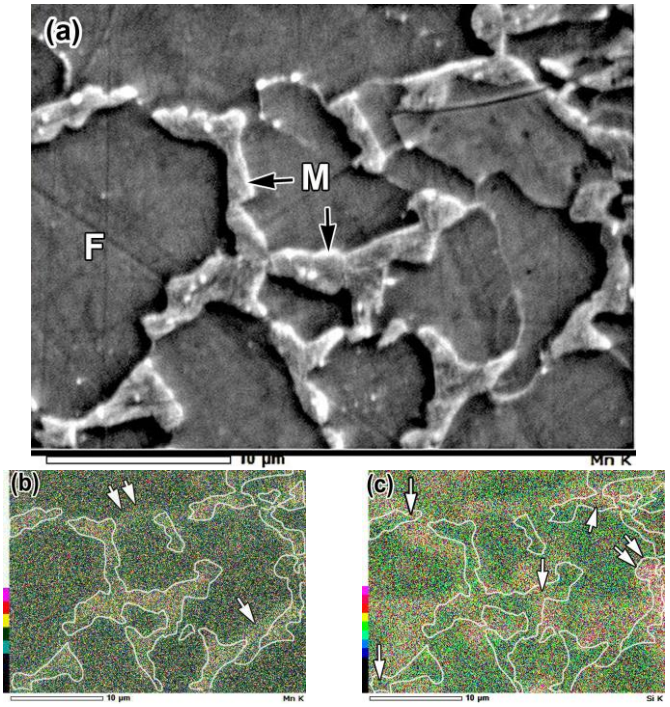

Fig. 5 (a) SEI image and the corresponding mapping of (b) Mn and (c) Si with the superimposed martensite areas contour (770 ºC, 10 min. F, M – ferrite, martensite, accordingly)

The comparison of Fig. 3 and Fig. 6 allowed one to conclude that an increase in annealing temperature from 770 ºC to 830 ºC resulted in certain variations in phase composition. Specifically, in martensite, a decrease in Mn content (from 2.20-2.26 wt% to ~1.65 wt%) and Cr content (from ~0.80 wt% to 0.66-0.70 wt%) was detected, while silicon content remained approximately at the same level. In ferrite a decrease in Mn content from ~0.90 wt% to ~0.60 wt% was revealed while Cr content almost did not change; also there was a slight increase in silicon content. An increase in annealing temperature considerably affected only the manganese content which decreased in both phases.

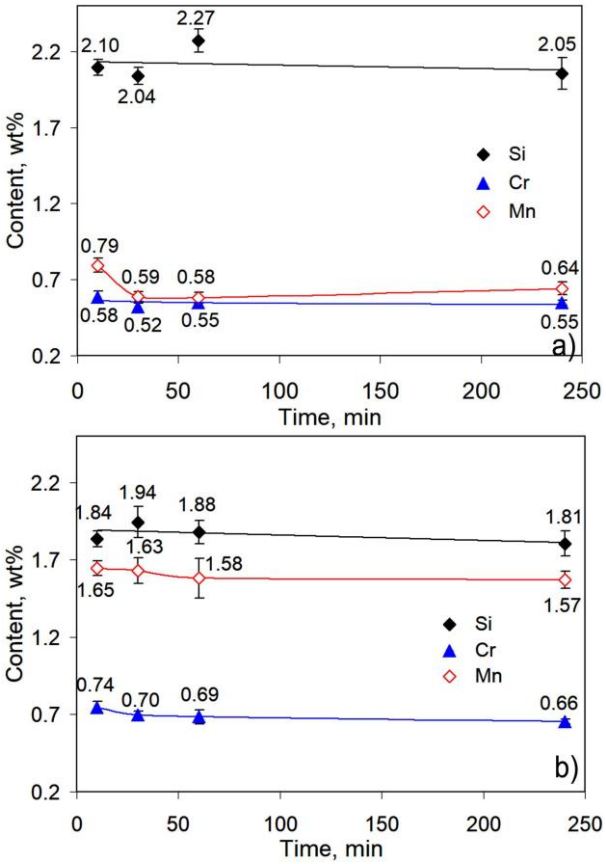

Fig. 6 Effect of holding time at 830 ºC on Si, Mn, and Cr content in (a) ferrite and (b) martensite

As follows from the mappings (Fig. 7), the holding at 830 ºC led to more pronounced partitioning the elements in different phases than at 770 ºC. Manganese was mostly concentrated in martensite, however some martensite areas were depleted with this element (shown by arrows in Fig. 7, b). The silicon distribution within ferrite grains became more homogeneous without the obvious grain-oriented segregation noted for 770 ºC (Fig. 7, c). However, EDX line-scanning still revealed the Si-spikes near the "ferrite/martensite" interface and grain boundaries although these "spikes" zones were much thinner than those at 770 ºC (about 1 μm thick).

The data obtained revealed that ITR annealing results in partitioning of Mn, Si, and Cr in the studied TRIP-assisted steel, whereas manganese partitioned to the greatest extent. At the end of 770 ºC-annealing the manganese content in austenite reached 2.26 wt.%, which is 2.6 times that of ferrite (0.86 wt%) with K_{Mn}=0.38 (Fig. 8, a). The annealing at 830 ºC led to a decrease in Mn content in austenite to 1.57 wt.% because of the increase in austenite volume fraction. With that, manganese-depleted zones appeared in martensite areas indicated by arrows in Fig. 7, b. Manganese content in ferrite decreased as well, caused by the manganese diffusivity stimulation by higher annealing temperature [30]. Thus, the distribution coefficient K_{Mn} at 830 ºC (is 0.40) remained similar to that of 770 ºC (is 0.38).

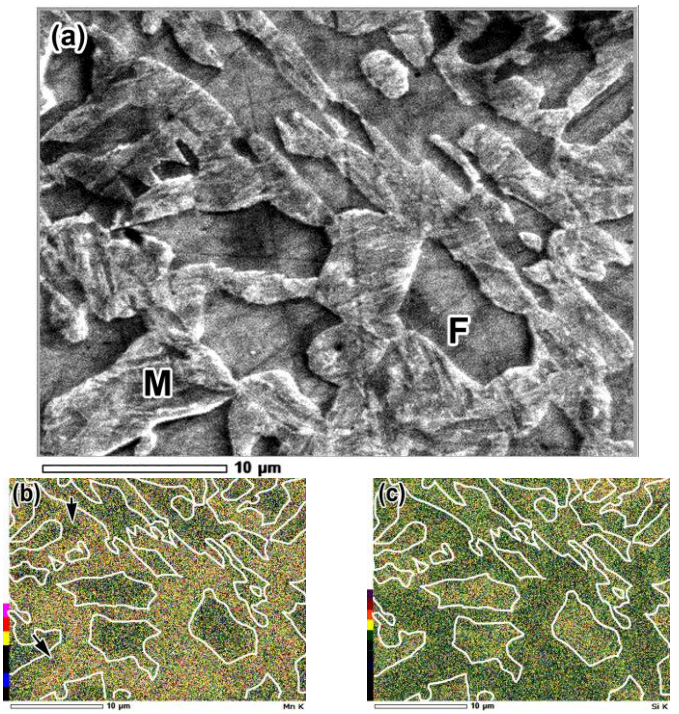

Fig. 7 (a) SEI image of microstructure and the corresponding mapping of (b) manganese and (c) silicon with the superimposed martensite contour (830 ºC for 30 min. F, M – ferrite, martensite, accordingly)

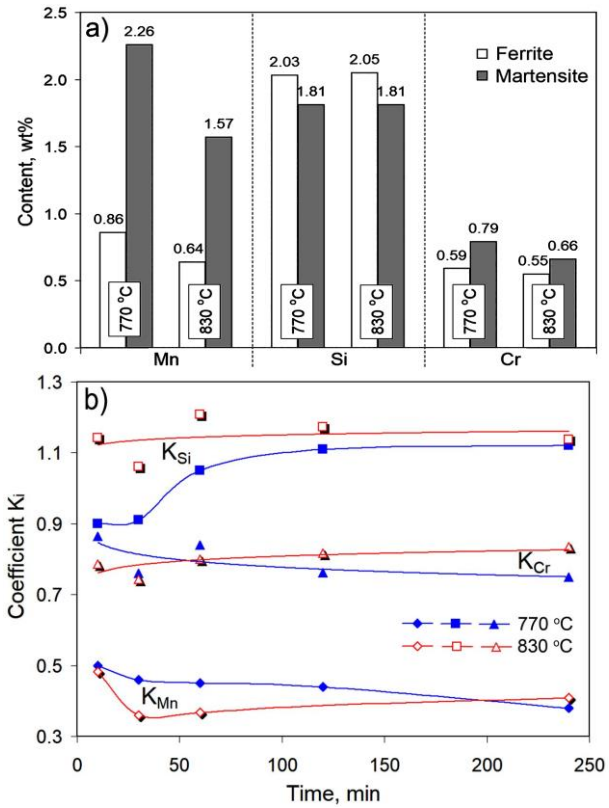

Fig. 8 (a) Phase content of Mn, Si and Cr (annealing time is 240 min) and (b) the effect of annealing time on the distribution coefficients K_{Mn}, K_{Cr}, and K_{Si}

The ferrite-stabilizing element silicon partitioned preferentially in ferrite, performing the same distribution coefficient K_{Si} (1.12-1.13) for both temperatures. Cr partitioning behavior is similar to Mn although its distribution coefficient K_{Cr} (0.75 for 770 ºC and 0.83 1.20 for 830 ºC) is much higher than that of manganese. Thus, the distribution coefficients for silicon and chromium were close to 1.0, meaning that Si and Cr are distributed approximately equally between the phases with a slight excess for the specific phase (Fig, 8, b). In contrast, the coefficient K_{Mn} (0.38-0.40) shows that. The greater part of manganese was accumulated in austenite (martensite).

The partitioning of Mn and Cr at 770 ºC proceeded with a low rate through all annealing holding (up to 240 min), which is consistent with the data of De Moor et al. [34] reported for medium-Mn "Third Generation" AHSSs subjected to intercritical annealing. However, in contrast to the observation of Luo et al. [26] and some other researchers [34, 35], we did not note the manganese segregation at the austenite/martensite interface.

The partitioning of Si at 770 ºC took place between 30-120 min holding. The distinctive feature of silicon partitioning is Si segregation at austenite/martensite interface (the same Si profile was observed by Nouri et al. [30] in dual-phase steels after annealing at 740 ºC). Noteworthy, that after 240 min holding silicon partitioning retained its uneven character while spikes of Mn concentration were associated only with carbide precipitates (Fig. 4a). The possible reason is the lower diffusivity of silicon as compared to manganese. In [30] the Si diffusion coefficient for dual-phase steels at 740 ºC was reported as $D_{\alpha Si}=3.64\cdot10^{-11}$ m^2/s for ferrite and $D_{\gamma S}=2.50\cdot10^{-15}$ m^2/s – for austenite. A big difference in D_{Si} for different phases causes an accumulation of silicon atoms at the γFe/αFe interface. In contrast, S. Sun and M. Pugh [35] found the diffusion coefficient of manganese in austenite for 0.1wt%C-2.67wt% Mn steel to be $7.12\cdot10^{-14}$ m^2/s (at 680 °C) which is an order of magnitude larger than above for silicon. Therefore manganese is evacuated faster from the boundary inward the grain, reducing its spike at the γFe/αFe interface. At 830 ºC the redistribution of manganese proceeds much faster to finish within 30 min.

Based on the above, ITR annealing at 770 ºC should not exceed 60 min. This holding time allows an increase in Mn content in austenite to stabilize it to phase transformation ensuring an increased volume fraction of retained austenite. On the other hand, the short holding will prevent the depletion of austenite by silicon. The decrease in silicon content may lead to carbide precipitation from austenite during bainitizing treatment, preventing the enrichment of austenite with carbon. This may decrease the VF of retained austenite thus negatively affecting the mechanical properties of steel [31]. ITR annealing at 830 ºC can be fulfilled with a holding of 10 min. The longer holding at 830 ºC may result in surface decarburization of the studied steel promoted by high Si content [32].

The obtained results for elemental partitioning allow predicting the volume fraction of austenite (f_{RA}) which may retain in the studied steel after bainitizing treatment:

$$f_{RA}=f_A-f_B-f_M, \quad (2.)$$

where f_A is the volume fraction of austenite at annealing temperature, f_B, is the volume fraction of bainite, f_M is the volume fraction of martensite formed after cooling from bainitizing treatment, respectively.

The volume fraction martensite can be calculated by Koistinen-Marburger equation [36]:

$$f_M=f_A-exp(-a_m\cdot(M_s-Tq)), \quad (3.)$$

where M_s is starting temperature of martensite transformation, T_q is quenching temperature, a_m is fitting parameter (0.011).

Ms temperature can be found by Andrews equation [36] based on the chemical composition (wt%) of austenite:

$$Ms=539-423C-30.4Mn-17.7Ni-12.1Cr-11.0Si-7.0Mo. \quad (4.)$$

To the end of 770 ºC-annealing (240 min) carbon content in austenite (C_A) should be almost 0.4 wt% (assuming that f_A=0.5 with full equilibrium carbon partitioning) while contents of Mn, Si and Cr are shown in Fig. 8a (molybdenum content is taken to be partitioned like chromium). For this case, M_s temperature is 270.8 ºC. According to equations (2) and (3) after the direct quenching from 770 ºC RA volume fraction should be 2.5 vol% only. However, f_{RA} can be increased in the course of bainite transformation which follows after intercritical annealing. Bainite transformation implies the rejection of carbon from bainitic ferrite into austenite causing the carbon enrichment of the latter [37]. Under silicon control the carbon is accumulated in austenite thus its concentration may reach high value, up to 1.1 wt%, as shown in [38] for 0.11 wt%C-1.5wt%Si-1.53wt%Mn steel. Presuming that bainite transformation will involve 70% of initial austenite (i.e. f_B=0.35) then carbon content in remaining austenite will increase to 1.17 wt% and M_s will decrease to minus 54.9 ºC resulting in 15 vol% of RA after final cooling.

The same calculations for 830 ºC-annealing (f_A=0.2, C_A=1.0 wt%) allow to get M_s=39.5 ºC and f_{RA}=15.6 vol% after direct quenching. Considering the high amount of carbon in austenite one can presume that this austenite will resist bainite transformation, completely retaining in the structure.

Thus, the studied steel may acquire about 15 vol.% of retained austenite as a result of elemental partitioning during intercritical annealing. This value is consistent with that previously reported in [1, 39] justifying the obtained results.

CONCLUSIONS

Based on the results obtained for 0.2wt%C-Si2Mn2CrMoVNb TRIP-assisted steel, major conclusions were drawn from this research:

1. During the annealing at 770 ºC manganese and chromium partitioned from ferrite to austenite with distribution coefficients of 0.38-0.50 and 0.75-0.86, respectively. Manganese partitioned in a greater extent resulting in manganese content in austenite to be 2.6 times that of ferrite. Silicon partitioned from austenite to ferrite with K_{Si}=0.9-1.12. An increase in annealing temperature to 830 ºC decreased the manganese content in austenite (by 1.44 times) and ferrite (by 1.34 times) whereas the content of Si and Cr remained the same to 770 ºC level.
2. Silicon is distributed unevenly within the ferrite grains, creating segregation zones near the ferrite/martensite interface or ferrite grain boundaries. As annealing temperature increased the width of these zones decreased from 2-5 μm to about 1 μm. Sharp "spikes" of manganese were associated with dispersed carbides MC.
3. At 770 ºC partitioning of Mn and Cr proceeded slowly during 240 min holding, while Si partitioning was completed after 120 min holding. At 830 ºC the elemental redistribution was finished within 30 min holding. The ITR annealing holding is recommended as 10 min for 830 ºC, and not higher than 60 min for 770 ºC.

Acknowledgments: This work is supported by Slovak Academic Information Agency (SAIA). R. Kussa and V. Zurnadzhy appreciate the support of Ministry of Science and Education of Ukraine under the project 0120U102087.

REFERENCES

1. W. Bleck, X. Guo, Y. Ma: Steel Research International, 88(10), 2019, 1700218. https://doi.org/10.1002/srin.201700218
2. H. Jirková, K. Opatová, Š. Jeníček, J. Vrtáček, L. Kučerová, P. Kurka: Acta Metallurgica Slovaca, 25(2), 2019, 101–106, http://dx.doi.org/10.12776/ams.v25i2.1267
3. Z. M. Rykavets et al.: Uspehi Fiziki Metallov, 20(4), 2019, p. 620–633. https://doi.org/10.15407/ufm.20.04.620
4. T. Nanda, V. Singh, V. Singh, A. Chakraborty, S. Sharma: Proceedings of the Institution of Mechanical Engineers, Part L: Journal of Materials: Design and Applications, 233(2), 2019, vol. 233, 209-238, https://doi.org/10.1177/1464420716664198
5. X. Tan et al.: Materials Science and Engineering: A, 771(13), 2020, 138629. https://doi.org/10.1016/j.msea.2019.138629
6. B. Fu, W.Y. Yang, Y.D. Wang, L.F. Li, Z.Q. Sun, Y. Ren: Acta Materialia, 76(1), 2014, 342-354. https://doi.org/10.1016/j.actamat.2014.05.029
7. E. Emadoddin, A. Akbarzadeh, Gh. Daneshi: Materials Characterization, 57(4-5), 2006, 408-413. https://doi.org/10.1016/j.matchar.2006.04.006
8. Z.H. Cai, H. Ding, H. Kamoutsi, G.N. Haidemenopoulos, R.D.K. Misra: Materials Science and Engineering: A, 654(27), 2016, 359-367. https://doi.org/10.1016/j.msea.2015.12.057
9. P.I. Christodoulou, A.T. Kermanidis, D. Krizan: International Journal of Fatigue, 91(Part 1), 2016, 220-231. https://doi.org/10.1016/j.ijfatigue.2016.06.004

10. B.L. Ennis et al.: International Journal of Plasticity, 88, 2017, 126-139. https://doi.org/10.1016/j.ijplas.2016.10.005
11. L.S. Malinov, I.E. Malysheva, E.S. Klimov, V.V. Kukhar, E.Yu. Balalayeva: Materials Science Forum, 945, 2019, MSF, 574-578. https://doi.org/10.4028/www.scientific.net/MSF.945.574
12. M.A. Vasylyev, B.N. Mordyuk, S.I. Sidorenko, S.M. Voloshko, A.P. Burmak: Surface and Coatings Technology. 343, 2018, 57-68. https://doi.org/10.1016/j.surfcoat.2017.11.019
13. V.I. Zurnadzhy et. al: Materials Science and Engineering: A, 745, 2019, 307–318. https://doi.org/10.1016/j.msea.2018.12.106
14. V. Kukhar, E. Balalayeva, A. Prysiazhnyi, O. Vasylevskyi, I. Marchenko: MATEC Web of Conferences, 178, 2018, 02003. https://doi.org/10.1051/matecconf/201817802003
15. A.D. Koval', V.G. Efremenko, M.N. Brykov, M.I. Andrushchenko, R.A. Kulikovskii, A.V. Efremenko: Journal of Friction and Wear, 33(1), 2012, 39-46. https://doi.org/10.3103/S1068366612010072
16. H.Y. Dong, K.M. Wu, X.L. Wang, T.P. Hou, R.Yan: Wear, 402-403, 2018, 21-29. https://doi.org/10.1016/j.wear.2018.01.009
17. V. Efremenko et al.: International Journal of Materials Research, 109(2), 2018, 147-156. https://doi.org/10.3139/146.111583
18. K. Rubešová, I. Vorel, H. Jirková, Š. Jeníček: Acta Metallurgica Slovaca, 24, 2018, 126–133. http://dx.doi.org/10.12776/ams.v24i2.1063
19. V.G. Efremenko, V.I. Zurnadzhi, Y.G. Chabak, O.V. Tsvetkova, A.V. Dzherenova: Material Science, Vol. 53, 2017, 67–75. https://doi.org/10.1007/s11003-017-0045-3
20. H. Guo, X. Feng, A. Zhao, Q. Li, M. Chai: Journal of Materials Research and Technology, 9(2), 2020, 1593–1605. https://doi:10.1016/j.jmrt.2019.11.085
21. B. Hu, H. Luo: Acta Materialia, 176(1), 2019, 250-263. https://doi.org/10.1016/j.actamat.2019.07.014
22. M. Zhang, W. Cao, H. Dong, J. Zhu: Materials Science and Engineering: A, 654, 2016, 193-202. http://dx.doi.org/10.1016/j.msea.2015.12.029
23. S.-J. Lee, S. Lee, B. C. De Cooman: Scripta Materialia, 64, 2011, p. 649–652, https://doi.org/10.1016/j.scriptamat.2010.12.012
24. J. Lis, J. Morgiel, A. Lis: Materials Chemistry and Physics, 81(2-3), 2003, 466-468, https://doi.org/10.1016/S0254-0584(03)00053-1
25. S. Lee, S.-J. Lee, B.C. De Cooman: Scripta Materialia, 65(3), 2011, 225-228, http://dx.doi.org/10.1016/j.scriptamat.2011.04.010
26. X.-N. Luo, X.-Y. Zhong, H.-W. Luo, H.-H. Zhou, C.-Y. Wang, J. Shi: Journal of Iron and Steel Research, International, 22(11), 2015, 1015-1019. https://doi.org/10.1016/S1006-706X(15)30105-9
27. H.-S. Park, J.-B. Seol, N.-S. Lim, S.-I. Kim, C.-G. Park: Materials & Design, 82, 2015, 173-180. https://doi.org/10.1016/j.matdes.2015.05.059
28. V.G. Efremenko, Yu.G. Chabak, A. Lekatou, A.E. Karantzalis, A.V. Efremenko: Metallurgical and Materials Transactions A, 47A(2), 2016, 1529-1543. https://doi.org/10.1007/s11661-016-3336-7
29. P. Rolland, V.L. Carlino, R. Vane: Microscopy and Microanalysis, 10(Suppl. 02), 2004, 964–965. https://doi.org/10.1017/S1431927604880504
30. A. Nouri, Sh. Kheirandish, H. Saghafian: Metal Sience and Heat Treatment, 59, 2018, 569–574. https://doi.org/10.1007/s11041-018-0191-8.
31. I. Spiridonova, O.V. Sukhova, A. Vashchenko: Metallofizika i Noveishie Tekhnologii, 21(2), 1999, 122-125.
32. A.D. Koval', V.G. Efremenko, M.N. Brykov, M.I. Andrushchenko, R.A. Kulikovskii, A.V. Efremenko: Journal of Friction and Wear, 33(2), 2012, 153–159. https://doi.org/10.3103/S1068366612020079
33. Y.-b. Liu, W. Zhang, Q. Tong, Q.-S. Sun: Journal of Iron and Steel Research, International, 23(12), 2016, 1316-1322. https://doi.ord/10.1016/S1006-706X(16)30194-7
34. E. De Moor, S. Kang, J. G. Speer and D. K. Matlock: Proceedings of the International Conference on Mining, Material and Metallurgical Engineering Prague, Czech Republic, 2014 Keynote Lecture II.
35. S. Sun, M. Pugh: Materials Science and Engineering: A, 276, 2000,167–174. https://doi.org/10.1016/S0921-5093(99)00261-0
36. K.W. Andrews: Journal of the Iron and Steel Institute, 203 (7), 1965, 721-727
37. V.I. Zurnadzhy et al.: Kovove Mater., 58, 2020, 129–140. https://doi.org/10.4149/km_2020_2_129
38. E. Girault, A. Mertens, J. Pascal, Y. Houbaert, B. Verlinden, J. Van Humbeeck: Scripta Materialia, 44(6), 2001, 885-892. https://doi.org/10.1016/S1359-6462(00)00697-7
39. H.-T. Jiang, W. Ding, D. Tang, W. Huang: Journal of Iron and Steel Research, International, 19(8), 2012, 29-36. https://doi.org/10.1016/S1006-706X(12)60136-8

OPEN ACCESS

ACTA METALLURGICA SLOVACA

2020, VOL. 26, NO. 3, 122-125

RESEARCH PAPER

UTILIZATION OF ANALYTICAL METHODS FOR THE FAILURE ANALYSIS OF INJECTION MOLDED PART

Ivan Gajdoš[1], Ján Slota [1], Ľuboš Kaščák[1], Oleksandr Grytsenko [2],Tomasz Jachowicz[3]

[1)] Technical University of Košice, Faculty of Mechanical Engineering , Department of CAx Technologies, Mäsiarska 74, Košice, Slovak Republic

[2)] Lviv Polytechnic National University, Department of Chemical Technology of Plastics Processing, Lviv, Ukraine

[3)] Lublin University of Technology, Faculty of Mechanical Engineering, Department of Technology and Polymer Processing, 36 Nadbystrzycka St., Lublin, Poland

*Corresponding author: ivan.gajdos@tuke.sk, tel.: +421-55-620-3518, Faculty of Mechanical Engineering / Technical University of Košice, 04001,Košice, Slovakia

Received: 01.05.2020
Accepted: 27.06.2020

ABSTRACT

As the use of the thermoplastic materials becomes conventional in numerous parts and various applications, incidence of various types of failure becomes inevitable. Failure of injection molded parts can be a cause of economic and legal problems, as well as causing health damage or death. Public perception of plastics is adversely affected by their failures, such as the bad reputation that early plastics earned with toys that broke too easily. As the injection molding process is very complex, finding the cause of failure is very complicated. In industrial mass scale production, determining the cause of failure is key point in customer-supplier relationship. In the presented study, a type of injection molded product from HDPE affected by occurrence of cracks was investigated by mechanical, thermal testing and spectral analysis. Mechanical properties were evaluated by the uniaxial tensile test and the SHORE hardness test. Thermal properties of the samples were evaluated by DSC/TGA analysis and for the spectral analysis a Raman spectroscopy device was used. Obtained results provided information about fluctuating quality of used material, coupled with non/stable molding conditions and small molding window. All those aspects caused molded in stress, which was released in the form of crack during the installation.

Keywords: molding failure; DSC; Raman Spectroscopy; tensile test

INTRODUCTION

High-Density Polyethylene (HDPE) is one of the most widely used thermoplastic material and probably the most valuable polymer in our daily life. It is used for production of various types of products, ranging from make grocery bags, shampoo bottles, children's toys, up to bullet proof vests [1-2]. Despite its versatility, PE polymer has the simplest structure of all commercial polymers, and the performance of the PE can be further improved by creating various composites with PE matrix [1-4].

As the utilization of the HDPE and HDPE composites becomes conventional in numerous parts and various applications, incidence of various types of failure becomes inevitable, ranging from cosmetics defects [5]. Failure of injection molded parts can be a cause of economic and legal problems, as well as causing health damage or death. Public perception of plastics is adversely affected by their failures, such as the bad reputation that early plastics earned with toys that broke too easily [6]. As the injection molding process is very complex, finding the cause of failure is very complicated. In industrial mass scale production, determining the cause of failure is key point in customer-supplier relationship. It is necessary to determine, whether the problem was caused by the selection of inappropriate material, design error, variance in material quality or the actual processing. That is why sophisticated testing methods are applied in such cases [6-8]. Methods determining the properties and cause of failure of HDPE part are mostly focused on laboratory testing of mechanical properties, thermal properties and the structure of the polymer with different level of crystallinity [9, 10].

In the presented paper, a type of injection molded product from HDPE (Fig.1) affected by occurrence of cracks was investigated by mechanical, thermal testing and spectral analysis. Cover (outside diameter = 218 mm) made of commercial HDPE grade DOW HDPE KS10100 UE exhibits crack occurrence and propagation through central part of molding (Fig.2), before, during or short after installation and therefore could not meet the desired service lifetime. Suspecting not stable molding condition at the producer molding shop and the material quality issues a set of analytical tests was necessary to find out the cause of crack occurrence, as some batches of cover did not have any problem.

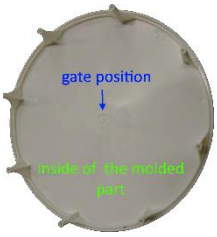

Fig. 1 Molded cover (inside)

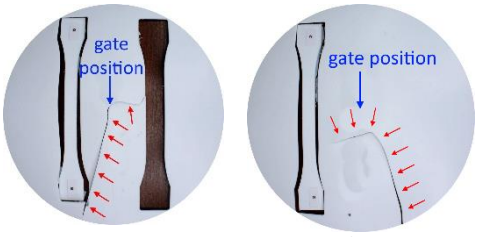

Fig. 2 Crack propagation/ cut location of tensile test samples

Numerous studies were focused on investigation of properties and crack causes in products made of HDPE, especially piping made of HDPE due to its wide use and application. To determine cause of failure of predict service lifetime standardized tests [11, 12], custom experiments [13] or FEA numerical modeling [14-16] were applied.

As the degree of crystallinity has significant influence on properties and performance of HDPE parts [2, 9], determining the degree of crystallinity in the part can provide important information about properties and structure of the material. One of the most applied method to determine the degree of crystallinity in the HDPE is the DSC. Although the sample size is very small, the sample destruction is inevitable. In cases where the sample destruction is not allowed, more detailed information about material structure is needed or to compare the DSC obtained crystallinity results a Raman spectroscopy is applicable [17-19].

MATERIAL AND METHODS

In this study totally six samples of injection molded part made of DOW HDPE KS10100 UE (supplier information) compound were investigated. Two of the samples with no quality issue and crack occurrence (sample no. 33 and 34) and four samples with crack (sample no. 35,36,37,38).

To evaluate mechanical properties of the samples material standardized uniaxial tensile tests according ISO 527-1 were performed and determination of samples surface Shore D hardness was determined according ASTM D2240. For structure and crystallinity observation the DSC testing method (ASTM D3418) on TA-

Q600 device and Raman spectroscopy with DeltaNu Rapid ID spectrometer were applied.
As presented in fig.2 a test sample for tensile test was cut out from the central part of the molding, that was not affected by crack. Obtained samples were analyzed before the tensile test with Raman spectrometry and the Shore D hardness. Samples for the DSC analysis were cut out from the molding, at the center of hole edge that remained after tensile test sample cut.
Three measurements were performed on each test sample. Average values of the hardness of individual samples were recorded. During the Shore D hardness testing, both sides of samples were measured. This approach was chosen, to capture eventually not uniform mold temperature resulting in different degree of crystallinity leading to differences in surface hardness.

RESULTS AND DISCUSSION

Tensile test

Table 1 shows the evaluated data from tensile test. The samples no. 33,34 without crack, meet the supplier tensile yield strength of 25 MPa and so the sample no.37 with crack do. Other samples with crack had the yield strength slightly below the supplier declared value. Standard deviation of tensile strength yield is 0.715.

Table 1 Results of tensile test

Sample	Evaluated values	
	Tensile strength yield [MPa]	*Tensile elongation [%]*
33	25.50	614
34	26.15	652
35	24.80	344
36	24.29	389
37	25.35	400
38	24.04	351
Mean	**25.08**	
St. Deviation	**0.715**	

Markedly differences are visible when comparing the value of tensile elongation. None of the samples reached the supplier declared value (1600%) , but the samples without crack have approximately 2 times higher tensile elongation. This could explain their resistance to crack building. All values of tensile elongation below material datasheet value can lead us to a conclusion that either extensive application of recycled material was used, or the molding condition (shear rate) were so high, that they lead to material degradation.

Shore D hardness

Shore D hardness measurement was performed on samples No. 33, 34, 35, 36, 37, 38 and 38 (Table 2). Measurements of samples showed differences in hardness values depending on which side of the sample was measured. The top side of the samples (as received and marked) on which the sample number was placed is "blue" and the reverse side "green". The measured values listed in Table 2 do not show significant differences in hardness between the samples but the mean value on the outside 59.72 is lower than the Shore D hardness 61.08 observed on the inside of the molding. The calculated mean values of Shore D hardness (tab.2), and the graph (Fig.3) with standard deviation show difference trend between the "blue" and "green" side.

Table 2 Results of Shore D hardness test

Sample	**Shore D hardness** blue /outside	**Shore D hardness** green /inside
33	59,9	60,3
34	59,8	60,5
35	59,5	62,7
36	59,8	61,3
37	59,8	60,8
38	59,5	60,9
Mean	59,72	61,08
St. deviation	0,172	0,864

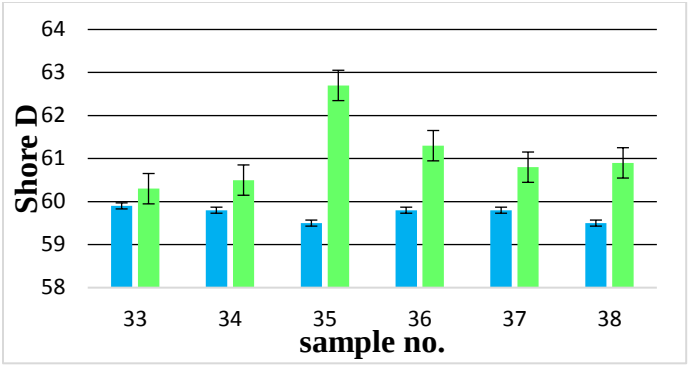

Fig. 3 Shore D results comparison for both sides of molding

DSC analysis

Data from DSC analysis are listed in Table 3. The results show that the melting temperature for individual samples is in the range from 133.93°C up to 135.37°C (Fig.4) and that corresponds to the HDPE polymer and no further peaks up to 200°C were observed. For samples no.33 and no.34 a higher degree of crystallinity was measured at level 71.92%, resp. 72.73%. Other samples taken from the moldings with crack achieve the measured crystallinity in the range from 67.19% up to 70.02%.

Table 3 Results of DSC analysis

Sample	Evaluated values	
	Melting temperature [ºC]	*Degree of crystallinity [%]*
33	135.37	71.92
34	134.70	72.73
35	133.93	67.19
36	134.98	70.02
37	134.92	68.13
38	135.09	68.90

Obtained crystallinity results from DSC analysis shows strong correlation between degree of crystallinity and tensile elongation.

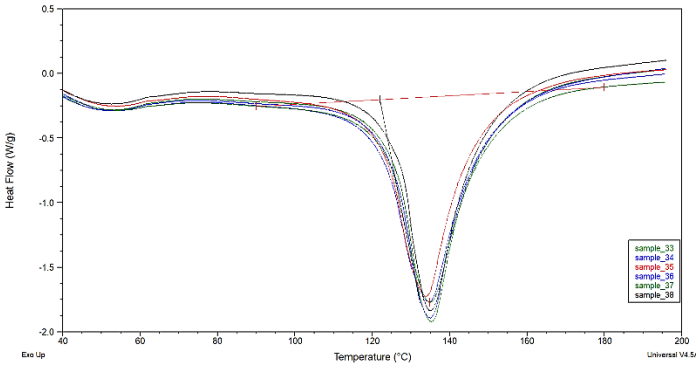

Fig. 4 DSC curves of measured samples

Raman spectrometry

Raman spectra of tested samples is presented in Fig. 5. Raman spectrum shift for samples in the range 1020-1550 cm^{-1} was measured. The peaks of spectral shifts at 1065 cm^{-1} ,1130 cm^{-1} and 1280 cm^{-1} distinguish clearly the samples 33 and 34 with higher crystallinity level. Spectral peaks of samples 33 and 34 at 1065 cm^{-1} resp. 1280 cm^{-1} are highest among tested samples, whereas their peak at 1130 cm^{-1} is the lowest. In Fig.5 are the spectral peaks of sample 34 with crystallinity of 72.73% marked with arrow.
These result of Raman spectral analysis show that this method is suitable for quick comparison of HDPE crystallinity degree between samples although not

exact value is obtained. The results from Raman spectroscopy match well to the results of the DSC analysis.

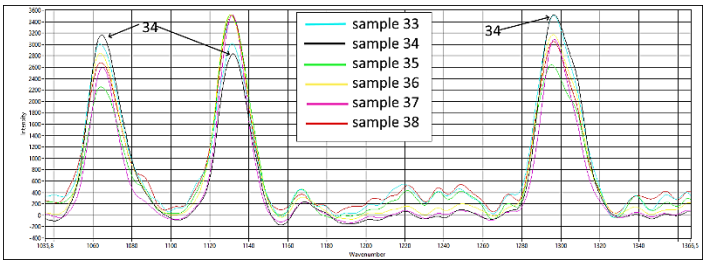

Fig. 5 Raman spectrum shifts of measured samples

CONCLUSION

Utilization of the HDPE as versatile material is nowadays present in wide variety of products. The wide variety of applications leads to occurrence of defects and failures of injection molded parts. Complexity of the injection molding process causes difficulties on the understanding of the failure cause. In mass scale production, determining the cause of failure is crucial factor in customer-supplier relationship. In practice there is high demand for methods that can quickly determine whether the problem was caused by the selection of inappropriate material, design error, variance in material quality or the actual processing.
In presented study four types of methods for analyzing HDPE material properties were applied to compare six molding. Two of them that meet the customer quality criteria (33,34) and four of them with failure (crack) (35,36,37,38).

- From the tensile test it was determined that yield strength of all samples fit in range 24.04-26.15MPa. The significant difference appears in the values of elongation. Samples 33,34 from good moldings exhibit approximately 2 times higher elongation at break (614%,652%) that samples from failure moldings (344-400%)
- Results from hardness measurement shows slightly difference and trend on all samples when comparing the inside and outside of the moldings. Difference between molding inside and outside is probably attributable to different mold temperatures during injection molding. However, this assumption could not be verified by processing data from supplier and further tests were considered unnecessary by the customer.
- DSC analysis provided values of melting temperature and degree of crystallinity. While the melting temperature remain in narrow range 133.93 - 135.37ºC and no correlation between failure and melting temperature was observed, the influence of degree of crystallinity is obvious. Samples 33 and 34 have the crystallinity above 71.92% and samples from failure moldings have crystallinity lower than 70.02%.
- Data from Raman spectroscopy and analysis of Raman spectra shifts show that a correlation between degree of crystallinity determined by DSC analysis and spectrum peaks at 1065 cm^{-1}, 1130 cm^{-1} and 1280 cm^{-1} is observable.

Based on obtained results it can be stated that material used to produce the moldings was the same, although the amount of virgin material is questionable due to low elongation at break. The degree of crystallinity was key factor that distinguishes the moldings with good quality and the molding with crack, and this factor was affected by not stable molding conditions. Taking into account the easy and non-destructive way to obtain Raman spectra, the method seems as ideal way for customer to quickly compare injection molded part and predict their quality.

Acknowledgments: Authors are grateful for the support of experimental works by project VEGA 1/0259/19.

REFERENCES

1. A. Ghanbari-Siahkali, P. Kingshott, D. Werner Breiby, L. Arleth, C. Koch Kjellander, K. Almdal: Investigating the role of anionic surfactant and polymer morphology on the environmental stress cracking (ESC) of high-density polyethylene. Polymer Degradation and Stability, 89, 2005, 442-453. https://doi.org/10.1016/j.polymdegradstab.2005.01.023
2. N. Pundhir, G. Arora, H. Pathak, S. Zafar: *Ballistic Impact Response of HDPE/UHMWPE Polymer Composite*. In.: Advances in Mechanical Engineering Select Proceedings of ICRIDME 2018. https://doi.org/10.1007/978-981-15-0124-1
3. K. Głogowska et al.: Assessment of the resistance to external factors of low-density polyethylene modified with natural fillers. Advances in Science and Technology Research Journal, 11(4), 2017, 35-40. https://doi.org/10.12913/22998624/75984
4. J. Sikora et al.: Polyethylene-Matrix Composites with Halloysite Nanotubes with Enhanced Physical Thermal Properties. Polymers, 11(5), 2019, 787-787. https://doi.org/10.3390/polym11050787
5. Ľ. Dulebová, T.Garbacz, V. Krasinskyi, B. Duleba: The influence of modifying HDPE on properties of the surface, Materials Science Forum, 818, 2015, 101-104. https://doi.org/10.4028/www.scientific.net/MSF.818.101
6. M. Ezrin: *Plastic Failure Guide. Causes and Prevention*. Hanser Publishing, 1996, ISBN 3-446-15715-8
7. T. Jachowicz: Investigation of Selected Properties of Injection-Molded Parts Subjected to Natural Aging. International Journal of Polymer Analysis and Characterization, 20, 2015, 307-315. https://doi.org/10.1080/1023666X.2015.1016788
8. T. Jachowicz, V. Krasinskyi, I. Gajdoš: The investigation of the influence of pro-degradant content on chosen properties of polymer composite. In: *Technological and design aspects of extrusion and injection moulding of thermoplastic polymer composites and nanocomposites*, volume 2. Košice, TU, 2014, 53-77. ISBN 978-80-553-1677-2
9. E. Nezbedova, A. Zahradnickova, Z. Salajka: Brittle failure versus structure of HDPE pipe resins. Journal of Macromolecular Science, Part B, 40(3-4), 2001, 507–515. https://doi.org/10.1081/mb-100106173
10. J.L. Jordan et al.: Low pressure shock response and dynamic failure of high-density polyethylene (HDPE). AIP Conference Proceedings, 1979(1), 2018, 090006. https://doi.org/10.1063/1.5044863
11. D.E. Duvall, D. Edwards: Field Failure Mechanisms in HDPE Potable Water Pipe, Plastics Engineering, 2012, https://doi.org/10.1002/j.1941-9635.2012.tb00808.x
12. S. Na, L. Nguyen, S. Spatari, Y. G. Hsuan: Effects of recycled HDPE and nanoclay on stress cracking of HDPE by correlating Jc with slow crack growth. Polymer Engineering & Science, 58, 2018, 1471–1478. https://doi.org/10.1002/pen.24691
13. F. Majid, M. Elghorba: HDPE pipes failure analysis and damage modeling. Engineering Failure Analysis, 71, 2017, 157-165. https://doi.org/10.1016/j.engfailanal.2016.10.002
14. S. Kalyanam et al.: Constraint Effects in Slow Crack Growth Test Methods for Service Life Prediction of High Density Polyethylene Piping. Journal of Pressure Vessel Technology, 2020, http://dx.doi.org/10.1115/1.4046884
15. M. A. Bouaziz et al.: Failure Analysis of HDPE Pipe for Drinking Water Distribution and Transmission. In: *Design and Modeling of Mechanical Systems - II. Lecture Notes in Mechanical Engineering*. Chouchane M., Fakhfakh T., Daly H., Aifaoui N., Chaari F. (eds). Springer, Cham, 2015, 407-414. https://doi.org/10.1007/978-3-319-17527-0_41
16. Z. Hao, J. Liu. J. Chang: Study on the Effect of HDPE Stress Absorbing Layer in Preventing Reflective Cracks, Transportation Soil Engineering in Cold Regions, *Lecture Notes in Civil Engineering*. Proceedings of TRANSOILCOLD 2019, p. 331-340, https://doi.org/10.1007/978-981-15-0450-1_34
17. I. Gajdoš, E. Spišák, V. Moravskyi: *Raman spectroscopy in polymer composites identifying and processing technologies*. In: Technological and design aspects of modern methods of composite and nanocomposite processing: Book of abstracts: 18-19 February 2015, Lviv, Ukraine, ISBN 978-617-607-711-4

18. I. Gajdoš et al.: Raman spectroscopy in polymer processing technologies. Acta Mechanica Slovaca, 15(4), 2011, 68-73
19. R. P. Paradkar, et al.: Raman Spectroscopy of Polymers. Encyclopedia of Analytical Chemistry, (2009), https://doi.org/10.1002/9780470027318.a9032

OPEN ACCESS

ACTA METALLURGICA SLOVACA

2020, VOL. 26, NO. 3, 126-131

RESEARCH PAPER

CORROSION AND WEAR PERFORMANCE OF ZA27/GRAPHENE/B_4C HYBRID NANOCOMPOSITES PRODUCED BY POWDER METALLURGY

Emre Deniz Yalçin[1], Aykut Çanakçi[2]

[1] Karadeniz Technical University, Abdullah Kanca Vocational High School, Trabzon, 61530, Turkey, emredenizyalcin@ktu.edu.tr

[2] Karadeniz Technical University, Department of Metallurgical and Materials Engineering, Trabzon, 61080, Turkey, aykut@ktu.edu.tr

*Corresponding author: emredenizyalcin@ktu.edu.tr tel.: 0462 377 81 70, Karadeniz Technical University, Abdullah Kanca Vocational High School, Trabzon, 61530, Turkey

Received: 27.04.2020
Accepted: 11.08.2020

ABSTRACT

In this research paper, dry sliding (unlubricated), corrosion and abrasive wear behavior of ZA27/ Graphene/ B_4C hybrid nanocomposites were studied. The hybrid nanocomposite samples were fabricated by powder metallurgy technique. Tribological tests were performed by employing a ball-on-disc type in the unlubricated situation and different loads (1, 2, 5 and 10 N). The examination of the worn and corroded surfaces, the powder characterization was performed using scanning electron microscopy (SEM). The findings indicated that the increase in B_4C nano-particle content can positively effect on the corrosion and wear behavior of the hybrid nanocomposites. The electrochemical polarization measurements showed that increasing of the nano B_4C content causes high corrosion resistance in the hybrid nanocomposites. The corrosion tests showed that the corrosion rate value of the ZA27/Graphene/B_4C hybrid nanocomposites decreased from 59.02 mpy to 16.77 mpy with increasing the nano B_4C content from 0.25% to 2%.

Keywords: ZA27, Graphene, B_4C, Hybrid nanocomposite, Wear, Corrosion

INTRODUCTION

Reinforcement of ZA27 alloys, with different materials, improve the strength of these alloys through better mechanical and physical properties. As a result, in recent years, Zn-Al based metal matrix composites (MMCs) have been used as alloys with lighter weight and high wear resistance [1-4]. In recent studies, B_4C ceramic particles are used to improve mechanical strength and increase thermal stability. The most important reason for using B_4C particles instead of SiC and Al_2O_3 ceramic particles is that B_4C particles have a relatively low density compared to SiC and Al_2O_3 particles and therefore the nanocomposites to be produced using B_4C particles have a higher specific strength value [5].

In recent years, graphene has emerged as a promising reinforcement material to advance wear resistance in hybrid nanocomposite materials. In this regard, many researches have been reported in the area of hybrid nanocomposites where the addition of graphene as a second phase leads to the development of the tribological and mechanical properties [6,10].

Graphene, as a very rigid material with low friction, is a perfect choice of material for bearing applications and nano-sized objects, including friction reduction and wear protection [7]. Mitrović et al. [8] have studied the wear behaviors of ZA27/Graphite/SiC hybrid nanocomposites manufactured by compo-casting. Their study showed that the ZA27/SiC/Graphite hybrid nanocomposites had greater wear resistance than ZA27 for all the sliding speeds and loads. In a recent study, the abrasion and corrosion behavior of nanocomposites produced by using in the range of 0.125 wt %-3 wt % nanographene reinforcement in ZA27 matrix alloy was investigated. According to the results, the hardness values of the samples decreased with increasing nanographene supplementation while increasing the abrasion resistance. In particular, 3 wt% nanographene reinforcement significantly improved the wear and corrosion properties. The corrosion rate for ZA27 was 2.719 mpy and the ZA27-Graphene nanocomposite supplemented with 3 wt% nano-graphene was 1.745 mpy [9]. Girish et al. [10] studied the wear behavior in the dry sliding environment by reinforcing the ZA27 matrix with graphite for tribological applications. In that study, 0%, 4%, 6%, 8% by weight graphite was added to the ZA27 matrix and it was found that the resistance to abrasion was best achieved with 4 wt % to 6 wt % graphite reinforcement.

The previous reports showed that nanoparticles reinforced with hybrid nanocomposites exhibit good tribological and mechanical properties. Because the unwished phases between the alloy and nanoparticles are inhibited at low increase the hardness of composite to uniformly dispersive in the matrix [11]. Dalmıs et al. investigated the mechanical and physical properties of ZA27-B_4C. Their experimental data indicated that nano B_4C can be used to enhance the mechanical and physical properties of the ZA27 matrix alloy. The increase in nano-sized B_4C ratio can cause the formation of agglomeration in grain size boundaries, which explains the decrease in tensile strength, density, and hardness values [12]. Dou et al. studied the wear behavior of Al6061 alloy matrix composites reinforced with 20% B_4C ceramic particles and stated that the wear loss was high at the beginning of the wear process and this loss was decreased as the wear rate increased and the oxide formation had a significant effect on the wear behavior [13]. In a study by Rajkumar and Aravindan, 5% to 30% by weight of graphite-reinforced and copper-based composite materials used in bearing materials were produced and density and hardness values of the produced materials were investigated. According to the results of this study, increasing the graphite amount and density caused a decrease in hardness values. The sintered density values decreased from approximately 7.6 g/cm^3 to 6.6 g/cm^3 and the hardness value decreased from 85 Hv to 55 Hv. The reason for the decrease in density values was attributed to the increasing amount of graphite and the increase in the number of aggregation regions formed by graphite particles in the structure and the decrease in hardness to the low hardness of graphite [14]. Seah et al. examined the acidic corrosion values of the composites they produced by adding 0%, 1%, 3%, 5% of graphite in the Zn-Al alloy matrix. Corrosion tests were performed at room temperature for 12 to 60 hours. They found that the wear decreases in HCl solution, while it increases with the addition of graphite [15]. Bobic et al. investigated the corrosion behavior of composites produced by the casting method by adding 1-3-5% SiC_P particles to ZA27 alloy. In the corrosion tests, 3.5% NaCl-(pH 6.7) was used as the test solution. After electrochemical polarization measurements, it was seen that increased SiC_P rate decreased the corrosion resistance of composites [16]. Morphology has a significant effect on the corrosion properties of metallic materials and alloys used in the industry. However, the physical and mechanical resistance of materials and alloys determine the amount of homogeneity in the distribution of the second phase [17-19].

Recent studies, showed that the form and content of the reinforcement material in the ZA27 matrix, the production technique of reinforced ZA27 and its hybrid nanocomposites play a very important function on the wear properties of nanocomposites. Nevertheless, to the author's knowledge, the effect of the reinforcement content on the corrosion and wear behavior of ZA27-based nanocomposites reinforced with nano-size graphene and nano-size B_4C has not been studied using powder metallurgy method. It should be also noted that

previous researches were just focused on the use of different reinforcement materials into the ZA27-based matrix. However, in this research, the effect of ZA27-based hybrid nanocomposites on the distribution of the nanoparticles in the ZA27 alloy was also studied. Hence, the aim of this research is graphene and B_4C reinforced zinc-aluminum based ZA27 matrix and hybrid nanocomposite materials; production by combining with powder metallurgy and mechanical alloying techniques, which have an important place in the production of materials. Also, the physical, morphological, and mechanical (hardness, abrasion resistance, and corrosion resistance) properties of the new materials produced were investigated.

MATERIAL AND METHODS

In this research paper, ZA27 powders (İki El Metal Co.) with average particle size 40 nm and a theoretical density of 5 g/cm^3 were used as the matrix alloy. B_4C and graphene powders (Alfa Aesar) with an average particle size of 50 nm and 55 nm were employed as reinforcement materials. The nominal composition of the ZA27 alloy listed in Table 1 [20,21]. Table 2 shows the coded of hybrid nanocomposites and their reinforcement content. ZA27 matrix alloy and its hybrid nanocomposites with different content of B_4C nanoparticles (0.25, 0.5, 1 and 2 wt. %) and graphene nanoparticles (3 wt. %) were produced by mechanical milling. Retsch PM 100 planetary ball-mill (high energy ball milling) is used in the milling process of hybrid nanocomposites. Powder mixing was carried out for 1 hour at room temperature in an argon atmosphere. The milling process was made of a tungsten carbide mill chamber with a volume of 250 ml, balls of 10 mm diameter. The ball: powder weight ratio was selected as 5:1. Mechanical mixing was carried out at Argon atmosphere, at room temperature and at a grinding speed of 400 rpm. The addition of zinc-stread was made at a rate of wt. 1% to prevent agglomeration during mechanical milling. Hot pressing was used for the preparation of the ZA27 matrix alloy and its hybrid nanocomposites. ZA27 matrix alloy and its hybrid nanocomposites powder were manually put consecutively in the steel die, and then the powders were uniaxial cold-pressed in a die up to 200 MPa for 2 minutes. The green compacts of ZA27 based hybrid nanocomposites in the die were hot-pressed for 3 hours at 435 ºC and 500 MPa in an argon atmosphere. The density of the sintered samples was determined by the Archimedes method. Morphology and internal structure analysis of hybrid nanocomposite powders were investigated by using a ZEISS LS 10 scanning electron microscope (SEM). Distribution of reinforcements in the matrix, porosity and surface investigations were made in detail by SEM analysis. After the wear and corrosion tests in SEM, the type of wear and surface condition and corrosion damage on the surface were examined. Rigaku Corporation, Japan brand X-ray diffractometer (XRD) was used for phase identification of ZA27/Graphene/B_4C hybrid nanocomposite samples. This was carried out at 40kV and 30mA and under Cukα (1,54059 Ao) radiation. XRD patterns were performed between 10-80 ° and 2θ.

Wear behavior of the ZA27 and its hybrid nanocomposites were examined by using a ball on disc (DUCOM) tribology tester. The tests were performed in dry sliding and 60 % relative humidity at room temperature. On account of wear test, ZA27 and its hybrid nanocomposite samples were ground with a 1500-2000 SiC grinding paper and further cleaned in ethanol. Before wear tests, the initial weights of the samples were measured. Balls made of H11 hot work tool steel with a diameter of 10 mm were used as abrasives. Before the wear tests, the surface roughness (Ra) values of the samples were measured as 0.2 µm. Wear test specimens were produced with a diameter of 30 mm and two different loads were used on one surface and a total of four loads were used on both surfaces. The applied loads were 1, 2, 5 and 10 N at 100 rpm (sliding speed range) and the sliding distances were chosen as 300 m. GAMRY reference 3000 brand corrosion device was used in corrosion tests. Corrosion samples were first drilled to a diameter of 2 mm. A copper wire was contacted with the sample to provide the electron current. The samples were ground with 600, 800, 1200 and 1500 grit and polished with alumina. The surface of each sample was washed with methanol and dried before starting the corrosion tests Potentiodynamic polarization tests were performed to determine the corrosion resistance of ZA27 / Graphene / B_4C hybrid nanocomposite samples. Potentiodynamic polarization measurements were started with a cathodic potential of 500 mV and continued to the anodic potential of + 500 mV at a scanning rate of 1 mV/s. In the experiments, a 3.5% NaCl solution was used as the electrolyte. To determine the corrosion resistance of ZA27 matrix alloy and hybrid nanocomposite samples, two potentiodynamic polarization tests were performed and averaged.

Table 1 Chemical composition of ZA27 alloy (wt.%)

Al	**Cu**	**Mg**	**Zn**
25,8	2,4	0,012	Bal.

Table 2 The samples produced by mechanical alloying and then hot pressing

Sample Number	Milling Time (h)	ZA27 (wt. %)	Graphene (wt. %)	B4C (wt. %)
ZA27	1	100	0	0
ZGB-0.25	1	96.75	3	0.25
ZGB-0.5	1	96.5	3	0.5
ZGB-1	1	96	3	1
ZGB-2	1	95	3	2

RESULTS AND DISCUSSION

Subtitle of results and discussion

In this study, nanocomposite and hybrid nanocomposites were produced by using the powder metallurgy method by reinforcing ZA27 matrix material with nano-size graphene and B_4C. The effects of nano-size graphene and B_4C on hardness, microstructure, wear and corrosion behavior of the ZA27/Graphene/B_4C hybrid nanocomposite were investigated. The main results obtained from experimental studies are discussed below.

XRD Analyses

XRD patterns of ZA27 matrix alloy and ZA27/Graphene/B_4C hybrid nanocomposites which have different graphene nanoparticle contents are presented in Fig. 1. The peaks of Zn, Al, and $CuZn_5$, besides that graphene, can be seen in the XRD pattern. When compared with the ZA27 matrix, newly produced phases such as the graphene phase were observed for ZA27/Graphene/B_4C hybrid nanocomposites, while the diffraction peaks of B_4C phase were much low for ZGB-0.5 hybrid nanocomposite. The increase in diffraction peak intensity of B_4C was observed for the ZGB-2 hybrid nanocomposite (Fig. 1). As shown in Fig. 1, the amount of $CuZn_5$ intermetallic phases increased for the hybrid composites. It should be noted that the $CuZn_5$ phase can be formed in the Zn–Al–Cu phase diagrams at a reaction temperature of 450 °C [22-23]. This result can be attributed to the positive effect of graphene on the formation of intermetallic phases and the densification process. As known, carbon-based materials such as graphite, graphene, and carbon nanotube have high thermal conductivity and the high conductivity of graphene particles increases the diffusion ability between Cu and Zn elements during the hot pressing process. Therefore, $CuZn_5$ phase content increases with increasing graphene content. A Similar result has been observed in a previous study [24].

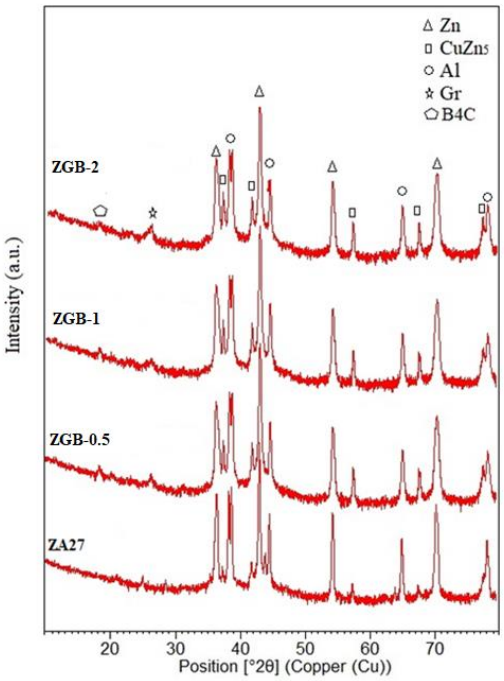

Fig. 1 XRD patterns of ZA27 alloy and ZA27/Gr/B_4C hybrid nanocomposite for different B_4C content

Microstructure

The SEM images of B_4C, graphene, and ZA27 matrix alloy powders are given in Fig. 2. ZA27 matrix powders were in ligament and irregular structure while B_4C powders were in a polygonal and angular structure. Graphene powders were hexagonal structure. (Fig. 2. and Fig. 3). Fig 3 also shows the morphology of hybrid nanocomposite powders with different reinforcement content after milling time of 1h. After 1 hour of milling, B_4C was embedded into the ZA27 powders surrounded with nano-size graphene particles The nearly flaked morphology of particles proposes that the 1 h milling time was enough to reach the desired condition.

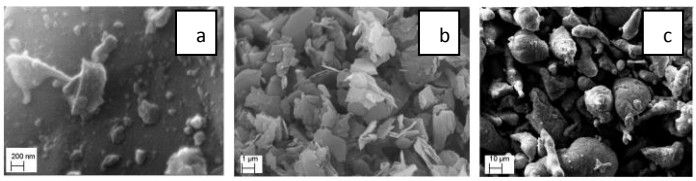

Fig. 2 SEM images of the initial matrix powders and reinforcement particles, (a) nano B_4C particles, (b) nano graphene particles, (c) ZA27 alloy powders.

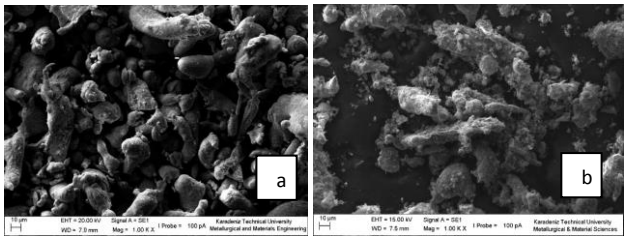

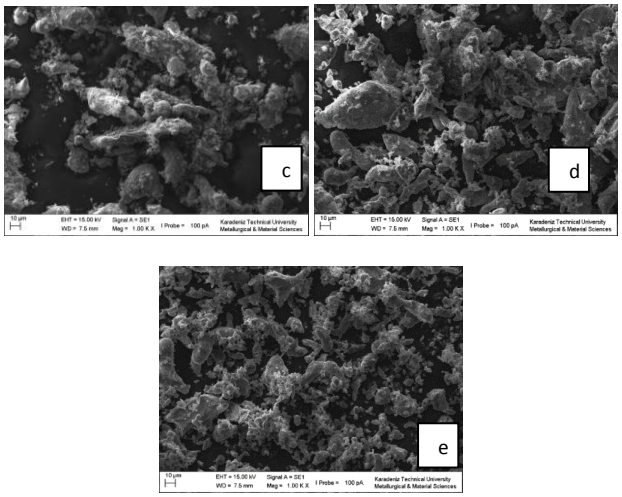

Fig. 3 SEM images of ;a) ZA27, b) ZGB-0.25 hybrid nanocomposite powders, c) ZGB-0.5 hybrid nanocomposite powders, d) ZGB-1 hybrid nanocomposite powders and e) ZGB-2 hybrid nanocomposite powders ball milled for 1h

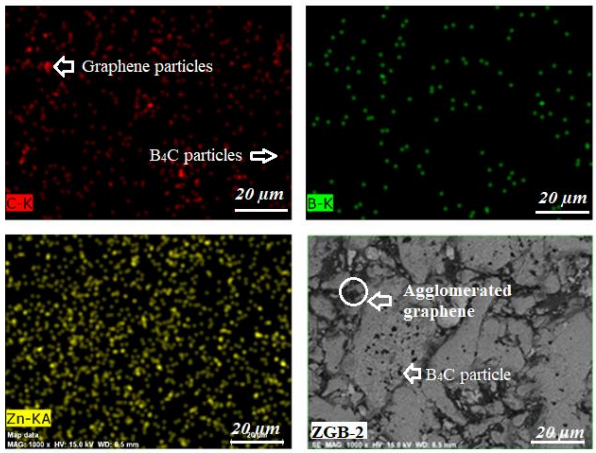

Fig. 4 SEM mapping images of ZGB-2 hybrid nanocomposite.

Fig. 4 shows SEM-EDS element distributions belonging to ZGB-2 hybrid nanocomposites. According to these internal structures, the red, green, blue, and yellow regions indicate the elemental distribution of C, B, Al, and Zn, respectively. Red regions show the distribution of nano-size graphene particles, while the green points indicate the nano B_4C particles into the ZA27 alloy matrix. The mapping confirmed that the distribution of nanoparticles in the matrix was nearly homogenous. As can be seen in the C-K mapping that showing with red point, agglomerated graphene particles are only located within the boundaries between neighboring ZA27 alloy matrix particles. While the B_4C particles are embedded in the matrix particles.

Porosity and Harness Measurements

The density decreased with increasing reinforcement. ZA27/Graphene/B_4C sample has a lower density than ZA27 due to its lower densification ability and the more agglomeration. The porosity of hybrid nanocomposites increased with the increase in the B_4C content. This can be attributed to the effect of hot pressing during the densification. The increase in the B_4C content from 1wt% to 2 wt% resulted in a decrease in the density of hybrid nanocomposites, nevertheless an important increase was obtained at a porosity of ZGB-2. Folorunso and Owoeye studied that the effect of SiC content on the physical, mechanical properties and tribological behavior of stir cast ZA27 alloy based hybrid composites. They

reported that the density of the composites decreased with an increase in the SiC content while slight voids exist as compared to the unreinforced alloy [25]. The results of Brinell-hardness measurements of all composites are shown in Table 3. It can be concluded that there was a dramatic decrease in hardness values. The decrease in the B_4C content resulted in higher hardness values for the hybrid nanocomposite. The results showed that B_4C content harmed on the porosity of hybrid nanocomposites during hot pressing. Moreover, ZGB-2 hybrid nanocomposite contains a high proportion of Graphene and B_4C supplements, the ZA27 matrix powders produced more plastic deformation and increased stresses between the matrix and the reinforcement. Yalçın et al. [9] achieved the best tribological properties in 3wt% graphene-reinforced ZA27 composites produced under similar conditions. They found the optimum performance at the composite mixture of ZA27 / 3 wt% Graphene porosity 4.05% with a Brinell hardness value of 62.67 HB.

Table 3 The porosities and hardness value of ZA27 alloy and composites

Sample Number	Porosity content (%)	Relative Density (%)	Brinell Hardness (HB)
ZA27	0.36	89.9	120
ZGB-0.25	10.02	88.1	71.9
ZGB-0.5	11.89	87.6	70.1
ZGB-1	12.34	87.2	68.9
ZGB-2	12.7	86.6	60.3

Wear Mechanism

For a better understanding of wear properties of ZA27/Graphene/B_4C hybrid nanocomposites, the B_4C content, and reinforcement distribution into the ZA27 matrix as well as bonding and interface interactions between ZA27/Graphene or B_4C reinforcement alloys should be further investigated. For the ZA27/Graphene/B_4C hybrid nanocomposites, the very critical parameter is the reinforcement content due to in the fact that microstructure changes from ZA27 alloy to hard ceramic with increasing B_4C content (wt.%). The capability of burden holding increases with an increase in B_4C content although the bonding strength between the ZA27 alloy and reinforcement materials decreases conspicuously. The result of the B_4C content on the wear loss of the ZA27 and hybrid nanocomposites are given in Table 4. As the B_4C content increased from 0.25 to 2 wt%, the wear weight loss decreased. A decrease in wear loss with increasing B_4C content was observed. Between the samples codded as ZGB-1 and ZGB-2 demonstrated lower wear loss at each load when compared with the ZA27 matrix alloy. This can be attributed to the presence of graphene nanoparticles in the matrix released to wear track of the disc during performing the wear tests. Fig. 5 shows both the lubrication of graphene and the hard nanoparticle property of the B_4C supplement showed a significant reduction in weight losses. Furthermore, it was shown that the relation between wear resistance and hardness is nearly linear in very advanced alloys. Girish et al. investigated the effect of graphite particles on mechanical, wear, and thermal behavior of ZA27 alloy composites. According to their results, the addition of graphite particles to the ZA27 zinc alloy matrix improves the wear resistance of the composite, the benefit of reinforcement is found more at 4–6% compared to higher values. It should be noted that a good indication that the graphite reinforcement will certainly help the designers to develop a suitable bearing material which gives better performance at elevated temperatures. However, hardness, thermal properties of composite such as thermal conductivity, diffusivity, and mechanical damping values at higher temperatures reduces with an increase in reinforcing percentage [10].

Table 4. The effect load on the wear loss of ZA27 alloy and hybrid nanocomposites at constant sliding distance (300m) and sliding speed (100 rpm)

Sample	Weight loss on 1N Load (mg.)	Weight loss on 2N Load (mg.)	Weight loss on 5N Load (mg.)	Weight loss on 10N Load (mg.)
ZA27	0.36	1.4	76.6	250
ZGB-0.25	0.002	0.003	0.006	0.028
ZGB-0.5	0.0014	0.0028	0.005	0.023
ZGB-1	0.0013	0.0025	0.004	0.021
ZGB-2	0.0012	0.0023	0.0032	0.009

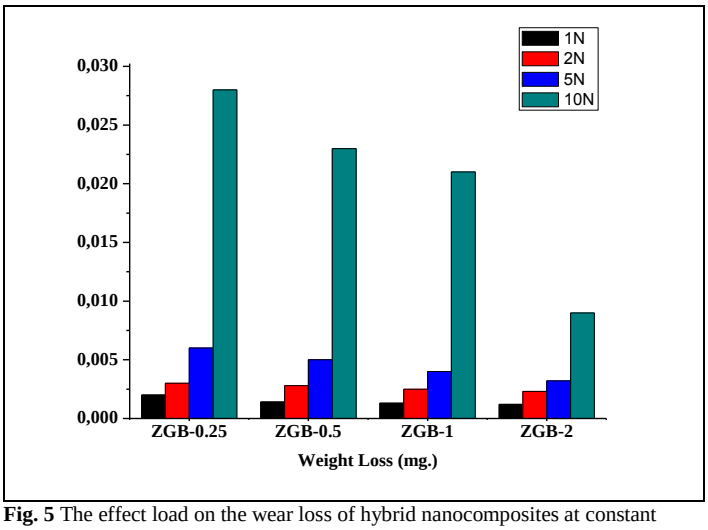

Fig. 5 The effect load on the wear loss of hybrid nanocomposites at constant sliding distance (300 m) and sliding speed (100 rpm)

Investigation of wear surfaces

Fig. 6 shows the SEM views of the worn surfaces of the ZA27 matrix alloy and hybrid nanocomposites. As seen in Figure 6, the wear mechanism includes the adhesion and delimitation mechanisms. SEM analysis of the worn surfaces shows that less damaged areas were obtained after wear testing on the ZGB-2 sample (Figure 6e) compared to that of the other hybrid nanocomposites and ZA27 alloys. The increasing agglomeration can be explained by the increased B_4C nanoparticle ratio. Wear marks were found on all wear surfaces in the same direction as the wear direction. In high magnifications, strips, plastic deformations, and cracks on wear surfaces were observed. As can be seen in Figure 6d-e, layer and cold tears are more common. This is because, in the experiments carried out at low loads, the particles that are detached from the sample surface have partially adhered to the surface of the sample during the test. As shown in Fig. 6, the tribological mechanism contains the abrasion and adhesion wear. The adhesion and abrasion wear that are essential tribological mechanisms describe fretting, pitting, spalling, scuffing, scoring, abrasion, and others. The increase in the B_4C particle content from 0.5 to 1 results in a change of adhesion wear mechanism to abrasion. This can be attributed to the distribution of B_4C particles in the ZA27 matrix. As seen in Fig. 6.b and c, even more particles have been severed, the more often the particles are bonded to the surface and the cold source has occurred. Hard B_4C particles eliminate the softening of the graphene particles in the structure. Kumar stated that the microstructure of wear surfaces of ZA27-graphite composites show deep and coarse grooves on the worn surface. The addition of SiC nanoparticles and Gr particles into the alloy increased the hardness of the ZA27 matrix alloy. Also, the SiC nanoparticles hinder the plowing during wear. The grooves became shallower as the content of graphite particles was present in the ZA27 hybrid composite [26].

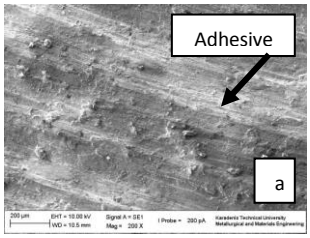

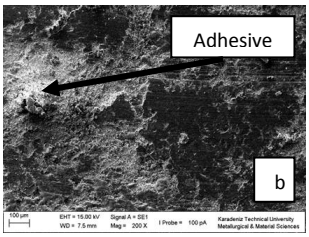

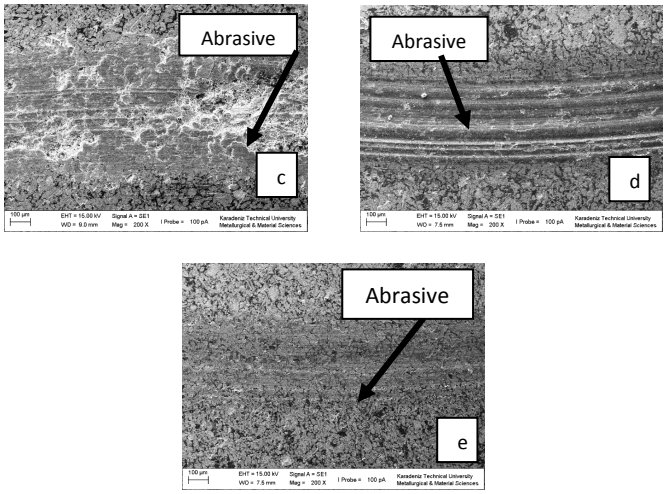

Fig. 6 SEM images of worn surface of a) ZA27, b) ZGB-0.25, c) ZGB-0.5, d)ZGB-1 and e) ZGB-2 ball milled for 1 h

Corrosion

Fig. 7 shows the potentiodynamic polarization curves of ZA27 matrix alloy and ZA27 / Graphene / B_4C hybrid nanocomposites (E_{kor}). The current density (I_{kor}) values decreased by the increase in B_4C contents. E_{kor} and low I_{kor} values close to the positive indicated that the corrosion resistance of the hybrid nano composite was higher.

Table 5 Electrochemical parameters derived from polarization data

Sample	I_{corr} (A/cm^2)	E_{corr} (mV)	Corrosion rate (mpy)
ZA27	1.23	-1000	2.719
ZGB-0.25	41.7	-1070	59.02
ZGB-0.5	19.4	-1150	57.6
ZGB-1	7.5	-968	20.8
ZGB-2	16.9	-1200	16.77

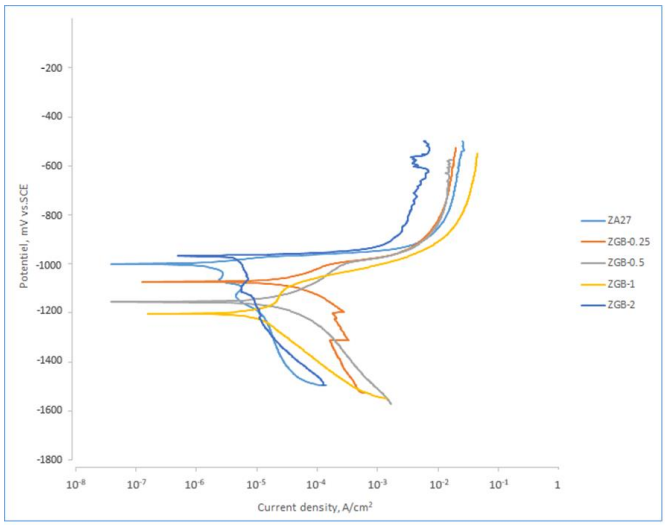

Fig. 7 Potentiodynamic polarization curves of ZA27 alloy and hybrid nanocomposites

The polarization curves of hybrid nanocomposites showed an increase in the current density with the increase in the applied polarization. The corrosion resistance of ZGB-2 hybrid nanocomposite in the environment was higher than other hybrid nanocomposites. In determining corrosion behavior, the particle content and the passive and active state of the environment were also important. Since ceramic particle causes a reduction in corrosion resistance in an active environment, it increases the corrosion resistance in a passive environment. Also, composites with low B_4C content with a E_{kor} value more than others were more passive. So, the tendency to ionization was higher. The other composites are known to corrode more quickly when activated [27]. Hybrid nanocomposites have high corrosion rates. This may be due to galvanic corrosion.

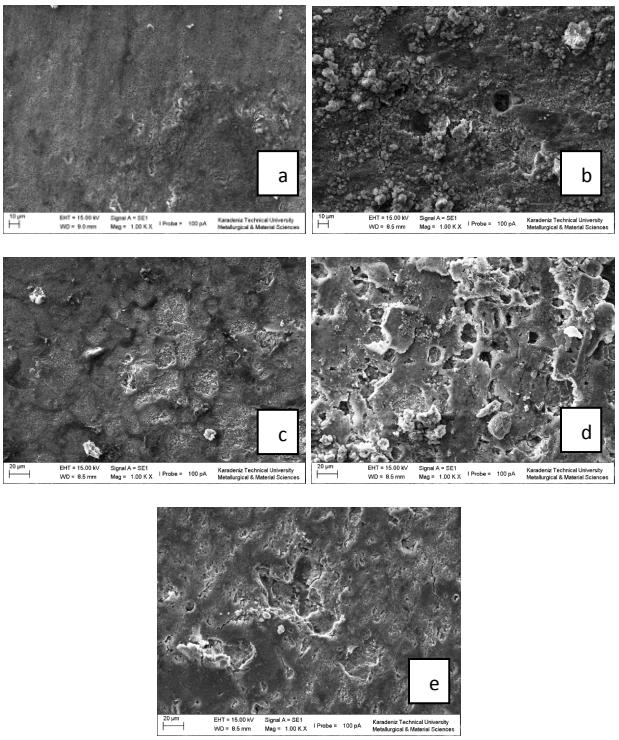

Fig. 8 SEM images after corrosion a) ZA27, b) ZGB-0.25, c) ZGB-0.5, d) ZGB-1 and e) ZGB-2 ball milled for 1 h

Fig. 8 shows the post-corrosion SEM images of ZA27 alloy and hybrid nanocomposites. On the surface of the hybrid nanocomposite specimens, the damages were formed in different sizes after corrosion and therefore the corrosion on the surfaces of the samples was observed. This type of corrosion usually occurs in neutral environments containing chlorine. The corrosion is known to occur in passivated materials in environments involving perchlorate, iodide, bromide or chloride ions when the electrode potential passing over a critical value. The potential varies depending on the material and the corrosive structure.

CONCLUSION

In the current work ZA27- Graphene-B_4C hybrid nanocomposites with 3wt% nano-size graphene, and 0.25 wt.%, 0.5 wt.%, 1 wt% and 2 wt.% nano-size B_4C were efficiently fabricated by the hot pressing method. According to this:

1. Hybrid nanocomposites that have excellent wear resistance than the ZA27 alloy have been manufactured with supplementations graphene and B_4C nanoparticles to ZA27 alloy.
2. According to SEM-EDS element distribution and XRD results of hybrid nanocomposites; Al, Zn, $CuZn_5$, B_4C and Graphene phases were encountered. The amount of Al, Zn, $CuZn_5$ phases increased with an increasing amount of reinforcement.

3. Higher porosity ratio such as 2 wt.% B_4C was obtained at ZGB-2 hybrid nanocomposite via hot sintering process.
4. ZGB-2 sample showed the best abrasion resistance without making grooves on the surface. Other samples exhibited an abrasive and adhesive wear mechanism. Therefore 3 wt. % nano graphene and 2 wt. % of B_4C supplementation can be an excellent choice.
5. The wear resistance of hybrid nanocomposites increased with the increase in the quantity of B_4C nano-sized particles.
6. The best corrosion resistance was obtained at ZGB-2 hybrid nanocomposites
7. Hybrid nanocomposites have high corrosion rates which are probably due to galvanic corrosion.

REFERENCES

1. Y.H. Zhu, H.C. Man and W.B. Lee: Microstructure of laser melted Zn–Al-based alloy, Journal of materials processing technology, 139, 2003, 296-301, https://doi.org/10.1016/S0924-0136(03)00239-5
2. T. Savaskan and A.P. Hekimoglu: Microstructure and mechanical properties of Zn–15Al-based ternary and quaternary alloys, Materials Science and Engineering: A, 603, 2014, 52-57, https://doi.org/10.1016/j.msea.2014.02.047
3. D. O. Folorunso and S. Owoeye: Influence of quarry dust-silicon carbide weight percentage on the mechanical properties and tribological behavior of stir cast ZA-27 alloy based hybrid composites, Journal of King Saud University - Engineering Sciences, 31(3), 2019, 280-285, https://doi.org/10.1016/j.jksues.2017.07.003
4. H. Şevik: The effect of silver on wear behaviour of zinc–aluminium-based ZA-12 alloy produced by gravity casting, Materials Characterization, 89, 2014, 81-87, https://doi.org/10.1016/j.matchar.2013.12.015
5. M. Afizadeh, M.H. Paydar and F.S. Jazi: Structural evaluation and mechanical properties of nanostructured Al/B_4C composite fabricated by ARB process, Composites Part B: Engineering, 44 (1), 2013, 339-343, https://doi.org/10.1016/j.compositesb.2012.04.069
6. T. Huang, Y. Xin, T. Li, S. Nutt, C. Su, H. Chen, P. Liu and Z. Lai: Modified graphene/polyimide nanocomposites: reinforcing and tribological effects, ACS Applied Materials Interfaces, 5(11), 2013, 4878-4891, https://doi.org/10.1021/am400635x
7. A. Klemenz, L. Pastewka, S.G. Balakrishna, A. Caron, R. Bennewitz and M. Moseler: Atomic scale mechanisms of friction reduction and wear protection by graphene, Nano Letters, 12, 2014, 7145-7152, https://doi.org/10.1021/nl5037403
8. H. Aahamed and V. Senthilkumar: Consolidation behavior of mechanically alloyed aluminium based nanocomposites reinforced with nanoscale Y_2O_3/Al_2O_3 particles, Materials Characterization, 62(12), 2011, 1235-1249, https://doi.org/10.1016/j.matchar.2011.10.011
9. E. D. Yalcin, A. Canakci, F. Erdemir, H. Cuvalci and A.H. Karabacak: Enhancement of wear and corrosion resistance of ZA27/Nanographene Composites Produced by Powder Metallurgy, Arabian Journal for Science and Engineering, 7, 2018, 1437-1445, https://doi.org/10.1007/s13369-018-3582-7
10. B.M. Girish, K.R. Prakash, B.M. Satisha, P.K. Jainb, K. Devic: Need for optimization of graphite particle reinforcement in ZA27 alloy composites for tribological applications, Materials Science and Engineering A, 530, 2011, 382, https://doi.org/10.1016/j.msea.2011.09.100
11. S. Mitrovic, M. Babic and N. Miloradovic: Wear Characteristics of Hybrid Composites Based on Za27 Alloy Reinforced With Silicon Carbide and Graphite Particles, Tribology in Industry, 36(2), 2014, 204.
12. R. Dalmiş, H. Cuvalci, A. Canakci and O. Güler: Investigation of Graphite Nano Particle Addition on the Physical and Mechanical Properties of ZA27 Composite, Advanced Composites Letters, 25(2), 2016, 37-42, https://doi.org/10.1177/096369351602500202
13. Y. Dou, Y. Liu, Y. Liu, Z. Xiong and Q. Xia: Friction and wear behaviors of B_4C/6061Al composite, Materials & Design, 60, 2014, 669-677, https://doi.org/10.1016/j.matdes.2014.04.016
14. K. Rajkumar and S. Aravindan: Microwave sintering of copper–graphite composites, Journal of Materials Processing Technology, 209(15-16), 2009, 5601-5605, https://doi.org/10.1016/j.jmatprotec.2009.05.017
15. K.H.W. Seah, F.S.C. Sharmas and B.M. Girishs: Corrosion characteristics of ZA-27-graphite particulate composites Corrosion Science, 39(1), 1997, 1-7, https://doi.org/10.1016/S0010-938X(96)00063-7
16. B. Bobic, J. Bajat, I. Bobic, and B. Jegdic: Corrosion Influence on Surface Appearance and Microstructure of Compo Cast ZA27/SiCp Composites in Sodium Chloride Solution, Transactions of Nonferrous Metals Society of China, 26, 2016, 1512, https://doi.org/10.1016/S1003-6326(16)64257-7
17. B. O. Fatile, B. O. Adewuyi and H. T. Owoyemi: Synthesis and characterization of ZA-27 alloy matrix composites reinforced with zinc oxide nanoparticles, Engineering Science and Technology, an International Journal, 20(3), 2017, 1147-1154, https://doi.org/10.1016/j.jestch.2017.01.001
18. C. He, B. Luo, Y. Zheng, Y. Yin, Z. Bai and Z. Ren: Effect of Sn on microstructure and corrosion behaviors of Al-Mg-Si alloys, Materials, 12(13), 2019, 2069, https://doi.org/10.3390/ma12132069
19. H. Wang, X. Zhang, Z. Xu, H. Wang and C. Zhu: Hot corrosion behaviour of Al-Si coating in mixed sulphate at 1150˚C, Corrosion Science, 147, 2019, 313-320, https://doi.org/10.1016/j.corsci.2018.11.026
20. T.J. Chen, Y. Hao, Y.D. Li and Y. Ma: Effect of solid solution treatment on semisolid microstructure of dendritic zinc alloy ZA27, Materials Science and Technology, 24, 2008, 1313-1320, https://doi.org/10.1179/174328407X226716
21. Y. Liu, H.Y. Li, H. Jiang and X. Lu: Effects of heat treatment on microstructure and mechanical properties of ZA27 alloy, Transactions of Nonferrous Metals Society of China, 23(3), 2013, 642-649, https://doi.org/10.1016/S1003-6326(13)62511-X
22. Yong Xiao, Mingyu Li, Ling Wang, Shangyu Huang, Xueming Du, Zhiquan Liu, Interfacial reaction behavior and mechanical properties of ultrasonically brazed Cu/Zn–Al/Cu joints, Materials and Design 73 (2015) 42-49, https://doi.org/10.1016/j.matdes.2015.02.016
23. Dafan Du, Guang Guan, Annie Gagnoud, Yves Fautrelle, Zhongming Ren, Xionggang Lu, Hui Wang, Yinming Dai, Qiuliang Wang, Xi Li, Materials Characterization,111 (2016) 31-42, https://doi.org/10.1016/j.matchar.2015.11.004
24. Onur Güler, Fatih Erdemir, Müslim Çelebi, Hamdullah Çuvalcı, Aykut Çanakçı, Effect of nano alumina content on corrosion behavior and microstructure of Za27/graphite/alumina hybrid nanocomposites, Results in Physics 15 (2019), https://doi.org/10.1016/j.rinp.2019.102700
25. Davies Oladayo Folorunso, Seun Samuel Owoeye, Influence of quarry dust-silicon carbide weight percentage on themechanical properties and tribological behavior of stir cast ZA-27 alloybased hybrid composites, Journal of King Saud University – Engineering Sciences, 31 (2019) 280-285. https://doi.org/10.1016/j.jksues.2017.07.003
26. Nagavelly Shiva Kumar, Mechanical and Wear Behavior of ZA-27/Sic/Gr Hybrid Metal Matrix Composites, Materials Today: Proceedings 5 (2018) 19969–19975. https://doi.org/10.1016/j.matpr.2018.06.363
27. S. Gollapudi: Grain size distribution effects on the corrosion behaviour of materials, Corrosion Science, 62, 2012, 90-94, https://doi.org/10.1016/j.corsci.2012.04.040

OPEN ACCESS

ACTA METALLURGICA SLOVACA

2020, VOL. 26, NO. 3, 132-137

RESEARCH PAPER

Oblique Gate Direction During Centrifugal Casting in Artificial Lumbar Disc Model of CP-Ti

Lilik Dwi Setyana[1], Muslim Mahardika[1,2], Suyitno[1,2*]

[1] Department of Mechanical and Industrial Engineering, Faculty of Engineering, Universitas Gadjah Mada, Yogyakarta, 55281, Indonesia

[2] Center for Innovations of Medical Devices, Universitas Gadjah Mada, Yogyakarta, 55281, Indonesia

*Corresponding author: suyitno@ugm.ac.id, tel.: +6281325017275, Faculty of Engineering / Universitas Gadjah Mada, 55281, Yogyakarta, Indonesia

Received: 16.04.2020
Accepted: 22.06.2020

ABSTRACT

Oblique gate direction in different angles was hardly applied in centrifugal casting. The purpose of this research was to determine the effects of oblique gate direction in centrifugal casting on density, porosity, roughness, and microstructures in the artificial lumbar disc model. The angles of the oblique gate were ranged from 30º to 150º toward to the runner. The sharp turn of the gate would cause retardations and losses friction that decreased the pressure in molten metal. This process caused the porosity and the surface roughness decreased while the density increased. The product in which the oblique gate direction was the same with the mold rotation was better than the one in the opposite direction. The tangential forces would increase the forces acting on molten metal when entered the mold with the oblique gate direction that same with the mold rotation. Gate with the θ of 90º was the most widely used, but the product was better to use the gate with the θ of 60º than the product with the θ of 90º. Hence, to obtain an artificial lumbar disc model with less porosity, high density, and smooth surface, the oblique gate of 60º should be applied.

Keywords: Gating design; Porosity; Centrifugal casting; Artificial lumbar disc model

INTRODUCTION

The principle of centrifugal casting is the application of forces generated from the centripetal acceleration of a rotating mold to distribute the molten metal into the mold [1]. Centrifugal casting produces a product with limited gas porosity, smooth surface, and accurate dimensions [1, 2]. These characteristics are caused by the distribution of molten metal into the mold cavity, which uses forces resulted from the centripetal acceleration of a mold rotation. The centrifugal force is a function of rotational speed, metal density, and radius [1]. The pressure distribution that controlled by rotational speed affects the shrinkage cavity. The porosity can be reduced by adjusting the rotational speed of more than 180 rpm [3]. Furthermore, increasing the rotational speed affects the increase in pressure, which causes a decrease in defects [4].

Defects on casting products usually happen due to improper in the gating system design (around 90%), and the rest is caused by the manufacturing problems [5, 6]. The product defects such as porosity cannot be avoided but can be controlled. Shrinkage or trapped gas during the cooling process can raise the occurrence of porosity [7-9].

The cross-section, position, and direction of the gate during centrifugal casting are designed to generate products with minimal porosity. Gate shapes that often used are rectangular [10-14] and circular [14-15] cross-section with perpendicular [10-14] and oblique [14] toward the mold cavity. The circular cross-section of the gate has a higher molten metal filling speed rather than the rectangular one [10]. Viscosity increases rapidly in rectangular cross-section, which has a closer gating wall distance to the center of cross-section rather than the circular one. This condition affects porosity, which tends to be more numerous [10]. Research on gate direction in centrifugal casting is still needed so that molten metal enters the mold cavity with high pressure and low turbulence. The high pressure and low turbulence can be obtained by changing geometry, shape, and number of the gates [12, 16].

However, the products of centrifugal casting always have porosity even though rectangular or circular cross-sections of gate shape are used. Gate direction, which same or opposite to the mold rotation, which purpose is to increase the molten metal filling to the mold, still needs further investigations [14]. The rectangular cross-section gate shape with the oblique direction the same as the rotation of the mold was suitable to be implemented in the centrifugal casting product [14]. However, the optimum angle of the oblique gate to be applied in the product is not yet known. The study is conducted to determine the influence of various oblique gate directions toward porosity, density, microstructure, hardness, and surface roughness of the artificial lumbar disc (ALD) model.

MATERIAL AND METHODS

Commercial pure titanium (CP-Ti) with composition of 99.72 wt.% Ti, 0.17 wt.% Fe, and 0.11 wt.% gaseous element was used in this research. The composition analysis used EDS (Quanta x50 SEM Series).

The product made in this study was an artificial lumbar disc model (ALD model). It was produced with centrifugal casting as arranged in Fig. 1. The product was set in a variety of oblique gate directions, which shown in θ ranged from 30º up to 150º. The θ was an angle formed by the axis of the gate and runner. Fig. 1.a showed the positions of the gate with the θ of 30º, 45º, 60º, 75º, and 90º. Then the θ of 90º, 105º, 120º, 135º, and 150º were shown in Fig. 1.b. The gate direction of 30º up to 75º was the same as the mold rotation. The gate direction of 90º was perpendicular toward the runner. Then the gate direction of 105º up to 150º was opposite with the mold rotation.

The ALD model geometry was shown in Fig. 2.a. The outer diameter was 30 mm, while the radius of the ball-on-socket was 13 mm with 2 mm depth. The gate shape (Fig.2.b) was rectangular cross-section. The cross-sectional geometry area declined gradually, along with the process of molten metal entering the mold. Then, the cross-sectional area of the gate declined gradually from 70 mm² to 30 mm² with the length of the gate for about 15 mm.

CP-Ti was melted at 1700º C, then poured in an ALD model shell mold. The zirconium-based ceramic material (consisted of 8 layers) was used to create the shell mold. The pouring rate of molten metal was about 0.12 kg s^{-1}. Moreover, when molten metal was poured, the mold was rotated in a counterclockwise direction at 60 rpm. The processes were conducted in the vacuum furnace (Flash caster, Japan).

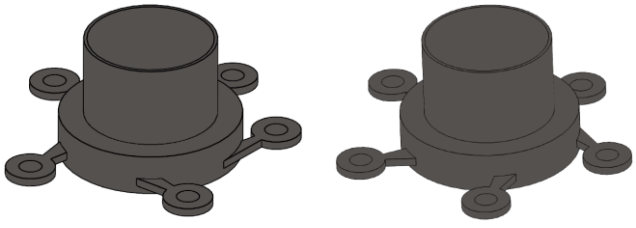

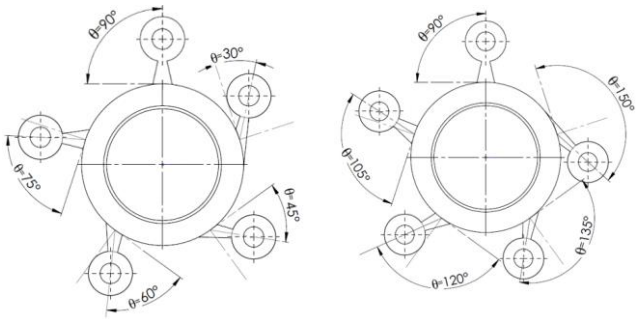

a. b.

Fig. 1 The schematic arrangement of the oblique gate direction

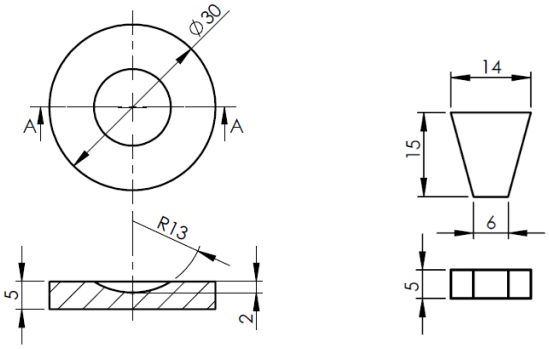

a. b.

Fig. 2 The geometry of ALD model (a) and gate shape (b)

The observations in this study consisted of shrinkage porosity and microstructures. The shrinkage porosity was observed using a stereo-zoom microscope (SZ-PT, Olympus, Japan) after the in-depth preparation by dye penetrant. Porosity calculations were manually counted using millimeter blocks. Besides, the percentage of porosity was calculated by comparing the porosity area with a total area of the product. The microstructure was observed using a metallurgical microscope (PME3, Olympus, Japan). Specimen preparation was done with sandpapers (grade #100 to #8000) to produce a smooth surface, then polished by the autosol. Kroll solution was used to bring out the microstructure (etching process).

The measurements consisted of hardness, surface roughness, and density. The hardness was measured from the sub-surface to the inner of a cross-sectional spanning product using a microhardness tester (HMV-M3, Shimadzu, Japan). The distance of each point test of hardness was arranged for 50 µm. Then, the load was set for 2 N. Profilometer (Surfcorder SE 1700, Fowler) was used for testing the surface roughness (Ra). The density was calculated by dividing the weight with the volume of the product. The equipment used to measure the weight in this research was analytical balancing (Sartorius AG Gottingen LC-12018).

RESULTS AND DISCUSSION

Results

The ALD model, which produced using centrifugal casting with the variation of oblique gate direction is shown in Fig. 3. All oblique gate directions, (θ range from 30º up to 150º) produce a complete filling casting. Fig. 4 shows defects on the product surface. The surface shrinkage porosities (A) and pinholes (B) can be seen on the surface. The surface shrinkage porosities are seen with an irregular shape that has a length and wide about 3 mm and 1 mm, respectively. The pinhole tends to congregate with a diameter of about 0.1 mm. It is also reported in prior research [17]. The product with θ of 60º has the least amount of surface shrinkage and pinholes. On the other hand, the product with θ of 150º has the largest surface shrinkage and pinholes, among others.

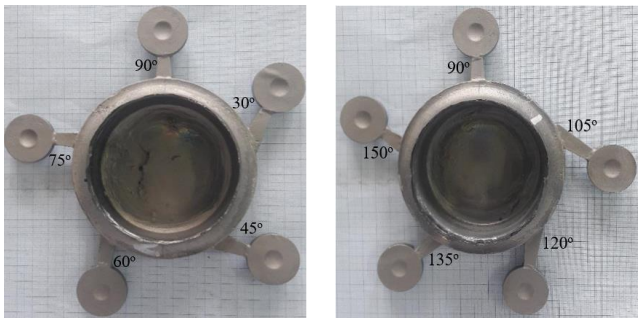

Fig. 3 The ALD model product

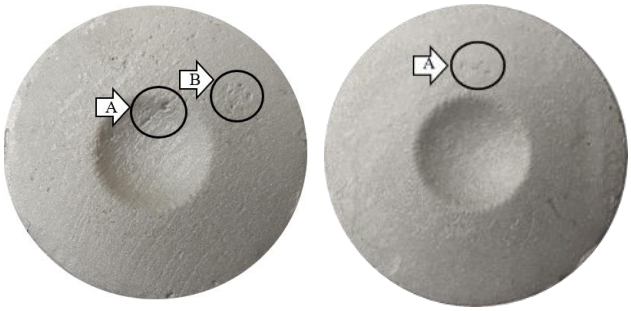

Fig. 4 The pinhole and surface shrinkage defects

Fig. 5 and Fig. 6 shows the internal porosity of ALD model products with θ of 30º up to 150º. The porosities are found in the mid area between the thickness of the products. The porosity with θ of 30º up to 90º tends to congregate with a size of about 100-200 µm. Meanwhile, the porosity with θ of 105º up to 150º tends to spread in size about 50-100 µm.

Fig. 7 shows the enlargement of the internal shrinkage porosity of the product with θ of 150º. It has an irregular shape in various sizes (50-200 µm). Some of the internal shrinkage porosity has a crack tail. Several adjacent porosities are connected by the crack tail.

Fig. 8 describes the number of porosity areas. The percentage porosity area with θ of 30º up to 150º are 0.65, 0.47, 0.34, 0.36, 0.49, 0.50, 0.59, 0.82, and 0.92% respectively. The porosity area tends to decrease along with the increase of the θ (30º up to 60º). On the contrary, for the θ that is more than 60º, the porosity area tends to increase. The θ of 150º has the highest percentage of porosity area (0.92%), while the θ of 60º has the lowest percentage of porosity area (0.34%).

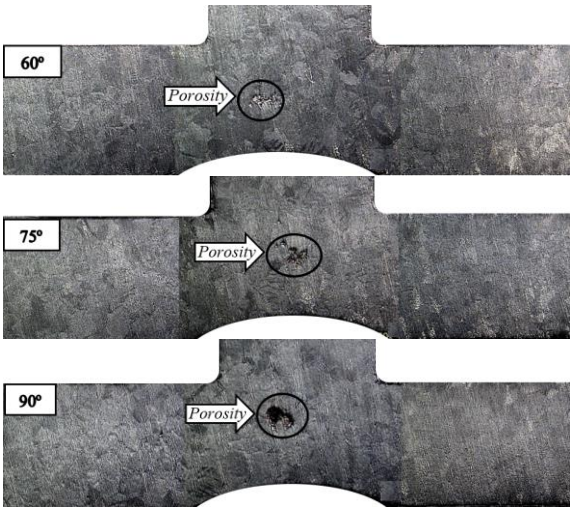

Fig. 5 The shrinkage porosity on product with various oblique gate directions (the θ of 75º up to 90º)

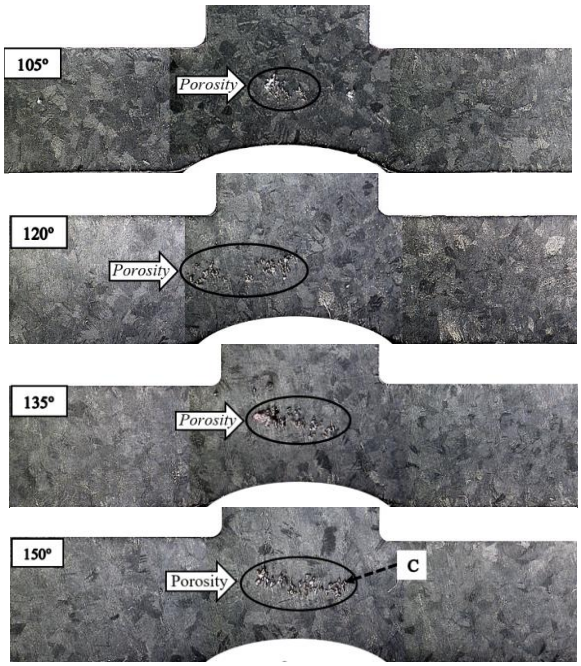

Fig. 6 The shrinkage porosity on product with various oblique gate directions (the θ of 105º up to 150º)

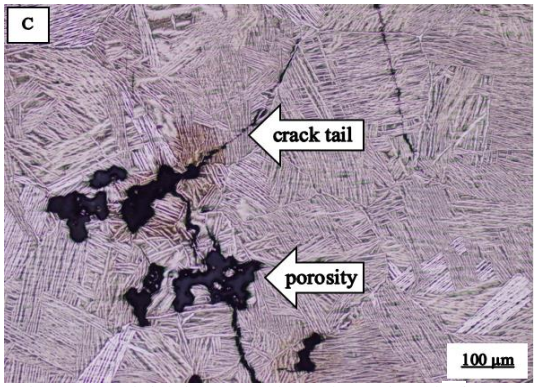

Fig. 7 An enlargement of shrinkage porosity (C in products θ of 150º)

The microstructure consists of α morphologies and equiaxed prior β grains in all kinds of oblique gate direction (Fig. 9). It is supported by the previous result [18]. The types of α-morphologies are known as α-case (a), prior β grain boundaries (b), and widmanstaten α (c). The morphologies of grain have the same characteristics as the previous research [19].

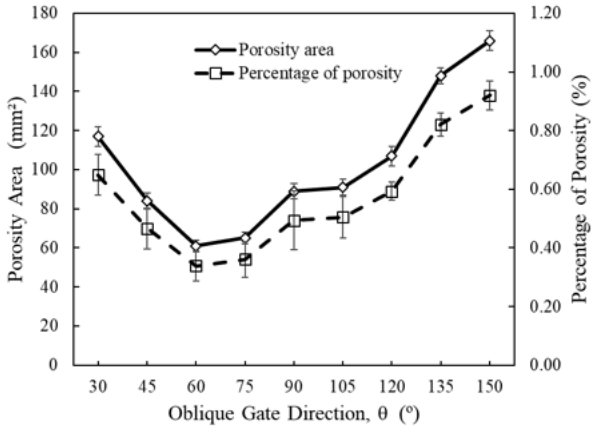

Fig. 8 The porosity area of ALD model

The α-case (Fig. 9.a) is formed in the sub-surface with a thickness of about 100 µm. The thickness of α-case in the product with the variate gate direction has a range from 50 µm to 250 µm. The thickness of α-case on the product with θ of 30º, 45º, 60º, 75º, and 90º are 200, 150, 50, 100, and 150 µm respectively. Then the α-case on the product with θ of 105º, 120º, 135º, and 150º are 150, 200, 250, and 250 µm respectively. The α-case on the product with a gate direction of 120º up to 150º has a crack for about 150-500 µm in length. Meanwhile, the α-cases on the product with other oblique angles have no crack.

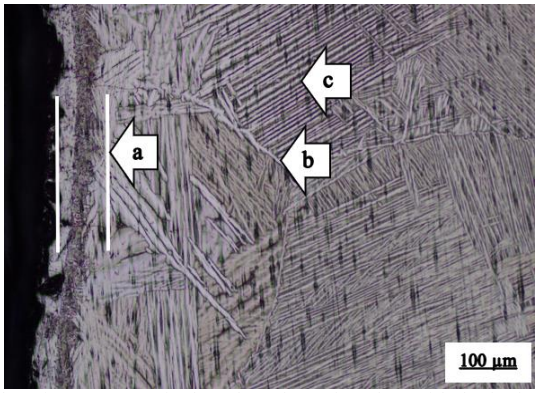

Fig. 9 The microstructures in the sub surface of product with the θ of 75º

The ALD density with various gate directions is shown in Fig. 10. The density for the θ of 30º up to 60º tends to increase from 4.514 to 4.519 g cm^{-3}. Whereas, for the θ of 60º up to 150º, the density decreases from 4.519 to 4.510 g cm^{-3}. The density increases up to 0.11% on a product with the θ of 60º compared with the density on the θ of 30º. On the contrary, the density decreases to 0.20% on the product with the θ of 150º compared with the density on the θ of 60º.

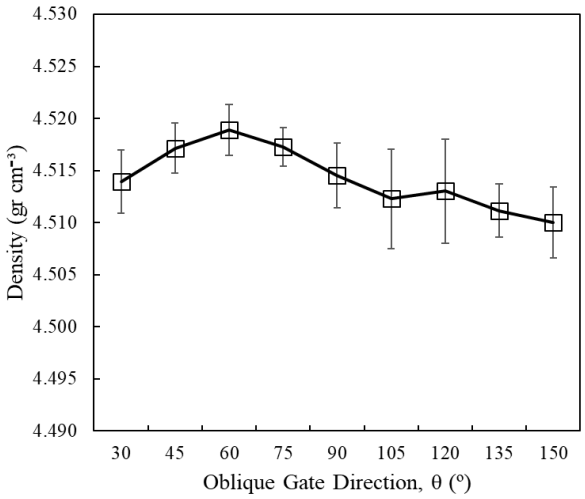

Fig. 10 The density of ALD model

The hardness of the ALD model is seen in Fig. 11. The hardness in the sub-surface with the θ of 30º is 766 VHN. Then on the distance of 0.2 mm, it drops to 332 VHN. Continuously on the distance of 0.05 mm, the hardness is 223 VHN. Meanwhile, after the distance of 0.05 mm the hardness tends to stabilize in 210 VHN. In general, the hardness with θ of 30º up to 150º from the sub-surface to the inner has the same trend. However, some differences occur in the sub-surface (α-case), as seen in Fig. 12. The hardness with the θ of 30º to 60º is decreasing from 766 VHN to 644 VHN. Meanwhile, the hardness on the product with θ of 75º to 150º is 701 VHN to 766 VHN.

The average hardness in the sub-surface with oblique gate direction opposite to the mold rotation (105º-150º) is higher than the average hardness with the same direction to the mold rotation (30º-75º). The enhancement of the average hardness is up to 7%.

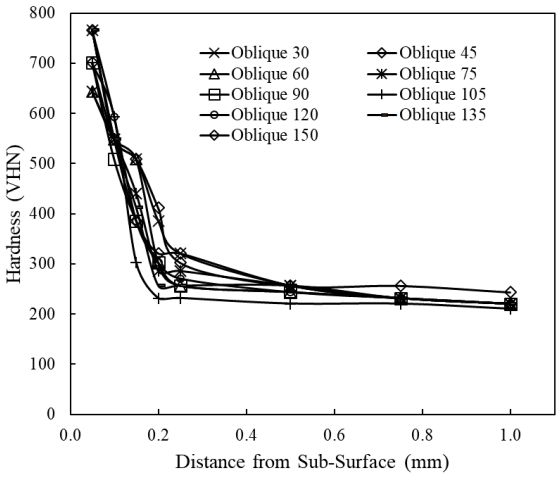

Fig. 11 The hardness of ALD model

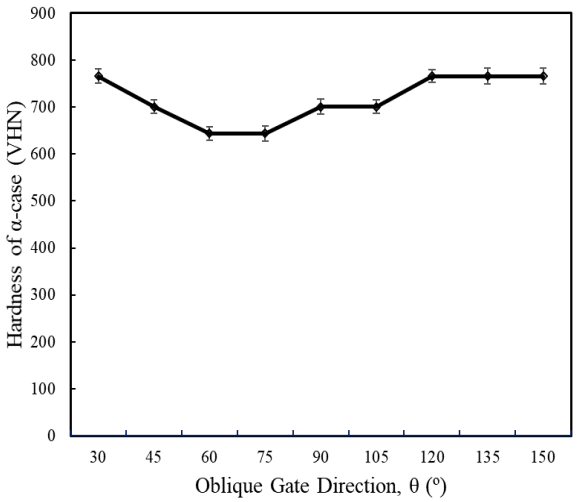

Fig. 12 The hardness of α-case

The surface roughness (Ra) of the product is ranged from 3.9 to 5.5 µm. (Fig.13). The surface roughness for the θ of 30º to 60º tends to decrease from 5.5 to 3.9 µm. Then it increases from 3.9 to 5.5 µm on the θ of 60º to 150º. The Ra with θ of 60º decreases 30% compared with Ra on the θ of 30º.

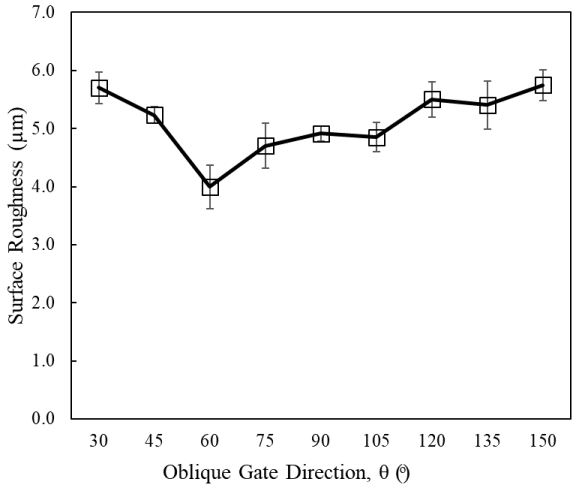

Fig. 13 The surface roughness of ALD model

Discussion

Gates with θ of 30º to 75º are the gates with the same direction to the mold rotation. Gate with θ of 90º is perpendicular toward the runner. Moreover, gates with θ of 105º to 150º are the gates with the opposite direction to the mold rotation.

Porosity area and surface roughness tend to decrease along with the θ from 30º up to 60º, then increase for the θ is more than 60º (60º up to 150º). Meanwhile, the density for the θ of 30º to 60º tends to increase, then decreases for the θ of 60º to 150º.

The forces acting on molten metal when entering a mold cavity with oblique gate are centrifugal and tangential. The magnitude of centrifugal force is the same for all oblique gates in which direction is away from the center. Meanwhile, the tangential force is different depending on the oblique gate directions. The tangential force at the oblique gate directions which same to the mold rotation (θ: 30º to 75º), is positive. The magnitude of oblique gate directions is directly proportional to the tangential force. It will increase the pressure and velocity of the molten metal when entering the mold. While the tangential force at the oblique gate directions which opposite to the mold rotation (θ: 105º to 150º), is

negative. It will reduce the velocity and pressure of the molten metal when entering the mold.

Product with θ of 30º up to 60º shows the increasing mechanical properties. Product with θ of 60º has the lowest percentage of porosity area (0.34%), the smoothest surface (3.9 µm), and the highest density (4.519 g cm^{-3}). It is caused by the total of centrifugal and tangential force acting on molten metal when entering the mold is bigger than forces on other gate directions. The pressure and velocity of molten metal become the highest when entering the mold. Besides, the gate direction allows molten metal to enter the mold cavity easily. It is caused by small retardation and losses friction. The increasing pressure and velocity of molten metal reduce the internal shrinkage porosity that automatically increases the density. The porosity tends to congregate with a size of about 50-100 µm without a crack tail. The shape and distribution of pores have a significant influence on the mechanical characteristics of materials [20]. The pressure of the molten metal to the wall cavity increases due to the high pressure when pouring. It causes a smooth surface.

Gate with θ of 90º is perpendicular toward the runner. This direction is the most widely used in casting [10-14]. The pressure and velocity of molten metal when entering the mold in this direction is determined by centrifugal force. The porosity formed in this direction is lesser than porosity in the opposite gate directions toward the mold (the θ of 105º up to 150º). In the pouring process, the molten metal has less retardation and friction to enter the mold cavity because there are no sharp turns. There is no crack in the α-case with a thickness of about 150 µm.

Product with θ 90º up to 150º shows the decreasing mechanical properties. Product with the θ of 150º has the highest percentage of porosity area (0.92%), roughest surface (5.5 µm), and lowest density (4.510 g cm^{-3}). Gate with the θ of 150º is opposite to the mold rotation. The tangential force in the gate direction is negative. Therefore, it decreases the total forces acting on molten metal. The pressure and velocity on molten metal at θ of 150º is the lowest. The pressure is the basic indicator that determines the shrinkage cavities distribution [3]. When the molten metal's pressure is low, it induces shrinkage porosities that directly decrease the density. Also, this gate direction has a sharp turn that causes the molten metal to encounter many retardations in entering the mold cavity. The retardations generate losses of friction between molten metal and gate wall. The greatest retardation occurs in the gate direction of 150º. Losses friction causes the molten metal's pressure to decrease, so it needs longer filling time to enter the mold cavity. The sharp turn also causes a turbulent flow. The turbulent flow will trap the air, then bring it back to molten metal [21]. It consequently induces porosities [22]. The porosity with the θ of 150º tends to spread in the irregular form with a crack tail. The low pressure also causes the pressure of molten metal to the wall cavity is less, which resulted in the roughness on the surface (5.5 µm). Besides, the low pressure causes the sub-surface of the product to have the thickest α-case, among other directions. The thick α-case will easily bring out a crack. The α-case is hard and brittle with a high-stress concentration [23], so cracking happens easily.

The microstructure formed in any of gate directions tends to be similar, which consists of equiaxed prior β grains and α types. The differences in the cooling rate caused by the differences in gate angles do not affect the type of microstructure. The pressure, velocity or friction also do not affect the microstructure, nor affects the thickness of the α case. The microstructure on the sub-surface is transformed from a bright coarse grain to become fine grains in the inner area. This structure is similar to previous research [14].

The hardness in all products (any oblique gate directions) from the sub-surface until the distance of more than 0.05 mm relatively have the same trend. On the sub-surface region, an α-case is formed with a thickness of 50 up to 300 µm. Hardness of α-case is 644 up to 766 VHN, which caused by the oxygen contamination and finer microstructure on the surface [24]. The hardness is particularly influenced by the kind of phase of the microstructure [25]. Oxygen can extend the α phase region, which shows that α phase will be easily formed with increasing oxygen content [26]. This is confirmed with the results of a study [14, 23]. The α-case on the product with the opposite gate direction of the mold rotation is harder and thicker than the same one. This condition happens because the product with same direction has a high pressure and velocity, which has a higher cooling rate compared to the opposite one during the solidification process. A higher cooling rate prevents oxygen diffusion occurs so that the α-case is thin [26].

CONCLUSION

The conclusions of this research are:

1. The product in which the gate direction is the same with the mold rotation is better than the one in the opposite direction because the tangential forces will increase the forces acting on molten metal when entering the mold with the gate direction the same with the mold rotation.
2. The sharp turn of the gate will cause retardations and losses friction that will decrease the pressure in molten metal, which causes the porosity and the surface roughness decrease while the density increases.
3. Gate with the θ of 90º (perpendicular toward the runner) is the most widely used in centrifugal casting, but the product is better to use an oblique gate with the θ of 60º than the product with the θ of 90º.
4. The oblique gate of 60º is the best direction to be implemented in the manufacture of artificial lumbar disc model.

Acknowledgments: The research was funded under dissertation grant by the Indonesian Ministry of Finance through Lembaga Pengelola Dana Pendidikan (LPDP). We thank the Department of Mechanical and Industrial Engineering Universitas Gadjah Mada for testing and observation equipments.

REFERENCES

1. W.S. Ebhota, A.S. Karun, F.L. Inambao: International Journal of Materials Research, 107(10), 2016, 1-10. https://doi.org/10.3139/146.111423
2. S. Wu, Q. Xu, X. Xue: Advanced Materials Research, 317-319, 2011, 456-459. https://doi.org/10.4028/www.scientific.net/ AMR.317-319.456
3. Y. Ling, J. Zhou, H. Nan, L. Zhu, Y. Yin: Journal of Materials Processing Technology, 251, 2018, 295-304. https://doi.org/10.1016/j.jmatprotec.2017.08.025
4. T. Prayoga, R. Dharmastiti, F. Akbar, Suyitno: Journal of Mechanical Science and Technology, 32 (1), 2018, 149-156. https://doi.org/10.1007/s12206-017-1216-8
5. A. Vegda, S. Bhingradiya, K. Faldu, P. Gandhi, M. Shah: International Journal of Scientific & Engineering Research, 9(1), 2018, 1222-1228.
6. S.L. Nimbulkar, R.S. Daluba: Perspectives in Science, 8, 2016, 39-42. https://doi.org/10.1016/j.pisc.2016.03.001
7. Sutiyoko, Suyitno, M. Mahardika, A. Syamsudin: Archives of Foundry Engineering, 16 (4), 2016, 157-162. https://doi.org/10.1515/afe-2016-0102
8. B.H. Hu, K.K. Tong, X.P. Niu, I. Pinwill: Journal of Materials Processing Technology, 105(1-2), 1999, 128-133. https://doi.org/10.1016/S0924-0136(00)00546-X
9. J.K. Kuo, P.H. Huang, H.Y. Lai, J.R. Chen: International Journal Advance Manufacture Technology, 92(1-4), 2017, 1093-1103. https://doi.org/10.1007/s00170-017-0198-0
10. P. Suwankan, N. Sornsuwit, N. Poolthong: Key Engineering Materials, 659, 2015, 647-651. https://doi.org/10.4028/www.scientific.net/KEM.659.647
11. M. Gadalla, R. Habingreither, R. Cook: The Minerals, Metals and Materials Society, 55, 2007, 39-45.
12. M. Masoumi, H. Hu, J. Hedjazi, M.A. Boutorabi: American Foundry Society, 05-152(2), 2005, 1-12.
13. B.H. Hu, K.K. Tong, X.P. Niu, I. Pinwill: Journal of Materials Processing Technology, 105, 2000, 128-133, https://doi.org/10.1016/S0924-0136(00)00546-X
14. L.D. Setyana, M. Mahardika, Sutiyoko, Suyitno: Acta Metallurgica Slovaca. 25(3), 2019, 193-202. https://doi.org/10.12776/ams.v25i3.1315
15. R. Ahmad, M.Y. Hasyim: Archives of Metallurgy and Materials. 56(4), 2011, 991-997. https://doi.org/10.2478/v10172-011-0109-6
16. O. Akinlabi, A. Ayodele: Acta Metallurgica Slovaca, 21(2), 2015, 135-141, https://doi.org/10.12776/ams.v21li2.567
17. J.K. Kuo, P.H. Huang, H.Y. Lai, W.J. Wu: The International Journal of Advanced Manufacturing Technology, 100, 2019, 529–540. https://doi.org/10.1007/s00170-018-2737-8
18. K.M. Ibrahim, M. Mhaede, L. Wagner: Transactions of Nonferrous Metals Society of China. 21(8), 2011, 1735-1740. https://doi.org/10.1016/S1003-6326(11)60923-0
19. M.J. Bermingham, S.D. Donald, M.S. Dargusch, D.H. John: Journal Material Research, 23(1), 2008, 97-104. https://doi.org/10.1557/JMR.2008.0002
20. J. Bidulská, R. Bidulský, M. A. Grande, T. Kvackaj: Materials, 12(22), 2019, 3724. https://doi.org/10.3390/ma12223724

21. B.D. Lee, U.H. Baek, J.W. Han: Journal of Materials Engineering and Performance, 16 (1). 2012. https://doi.org/10.1007/s11665-011-0111-1
22. J.R. Brevick: Die Casting Engineering. 5, 1997, 42–46.
23. W.J. Boettinger, M.E. Williams, S.R. Coriell, U.R. Kattner, B.A. Mueller: Metallurgical and Materials Transactions B. 31(B), 2000, 1-9. https://doi.org/10.1007/s11663-000-0026
24. X. Feng et.al: Journal of Materials Science & Technology, 32, 2016, 362-371. https://doi.org/10.1016/j.jmst.2015.12.010
25. S. Darmo, L. D. Setyana, Tarmono, N. Santoso: IOP Conf. Series: Materials Science and Engineering, 384, 2018, 1-4. https://doi.org/10.1088/1757-899X/384/1/012017
26. Y. Ma et.al: Journal of Materials Science & Technology, 26(2), 2010, 131-135. https://doi.org/10.1016/S1005-0302(10)60021-7